International
Progress Report

IPR-04-09

Äspö Hard Rock Laboratory

Using borehole tides to determine fracture parameters

2 – Data analysis

Hans-Georg Scherneck

Chalmers University of Technology

December 2003

Svensk Kärnbränslehantering AB
Swedish Nuclear Fuel
and Waste Management Co
Box 5864
SE-102 40 Stockholm Sweden
Tel 08-459 84 00
+46 8 459 84 00
Fax 08-661 57 19
+46 8 661 57 19

Äspö Hard Rock Laboratory

Report no.
IPR-04-09
No.
F50K
Author
Hans-Georg Scherneck
Date
Dec. 2003
Checked by
Mansueto Morosini
Date
2004-05-24
Approved
Christer Svemar
Date
2004-06-11

Äspö Hard Rock Laboratory

Using borehole tides to determine fracture parameters

2 – Data analysis

Hans-Georg Scherneck

Chalmers University of Technology

December 2003

Keywords: Keywords: Earth tides, tidal strain, ocean tide loading, confined aquifers, atmospheric loading, groundwater tides, fractured rock, crystalline rocks, borehole geophysics, hydrogeology, precambrian rocks, Sweden, Baltic Shield, Äspö HRL

Abstract

The purpose of the study was to investigate whether the results of the tidal pre-study on KAS03 section A (800 m depth) could be transferred to other boreholes around Äspö. The expectation was that fracture zone parameters could be determined sufficiently well in the other cases. The fracture zone parameters of the model are dip and strike, Poisson ratio, modulus of elasticity (E), and an along-plane thinning ratio ($E\beta$). Of these strike and Poisson ratio are most clearly resolvable. Dip and elasticity are highly correlated and need ancillary information for unique determination. It was hoped that barometric pressure forcing would provide the missing constraint on dip. However, the effects induced by air pressure are too small and too much concentrated at low frequencies to provide sufficiently strong constraints. The most prominent finding is that almost all boreholes display very similar tidal response, and the strike angle solution for a supposed singular fracture zone is found consistently between 120° and 140° from north.

Sammanfattning

I denna delrapport undersöks om den tidala metodiken från förstudien kan appliceras på de andra borrhålen vid Äspö. Förstudien gällde en 800 m djup sektion i borrhålet KAS03. På grund av gynnsamma förhållandena i KAS03 var det möjligt utifrån tidjordsdrivna tryckförändringar i borrhålssektionerna att bestämma parametrar i en spickzonsmodell, i huvudsak sprickzonens orientering (stup och strykvinkel) och dess elastiska parametrar. Förväntningen var att liknande resultat skulle kunna erhållas i de andra borrhålssektionerna, och att orienteringsvinklarna skulle vara representativa för varje spricka för sig. Stupvinkel och elasticitetsmodul är starkt korrelerade i det rent tidala problemet, så att ytterligare information behövs för att lösa den kopplingen. Till detta ändamål utökas studien att även omfatta borrhålens respons när jordytan belastas av varierande atmosfärstryck. I studien befinns dessvärre tryckeffekterna i det intressanta frekvensområdet mellan en och två cykler per dygn som för små och precisionen för de resulterande parametrarna som för osäker. Det allt överskuggande resultatet är att nästan alla borrhålssektioner uppvisar en liknande respons i avseende på sprickzonmodellens strykvinkel. Den bestäms till mellan 120 och 140 grader öst utgående från nord.

Contents

Extended summary

This second part of the report on tidal analysis of borehole water pressure observations comprises the analysis of 47 different data segments from 23 boreholes at different levels and in different .time periods. The boreholes are all located at the Äspö site north of Oskarshamn, Sweden. We distinguish holes that are drilled from the surface and holes drilled from tunnels. The former can reach considerable depth. We also distinguish periods when relative pressure measurements were taken, most of them with sub-mm resolution, and absolute pressure measurements, most of them with 5 mm resolution. Tidal variations can be discerned in practically all these situations.

The following results can be regarded as established: Tides with amplitudes up to 0.2 m are present in the borehole pressure records. Singular exceptions appear to relate to confinement or packer failure. Tidal shear strain is coupled into the borehole pressure in the majority of borehole sections. The observed borehole tides are thus not a pure volumetric effect. We also see significant ocean loading strain due to the North Sea and North Atlantic despite the great distance to the coast. If the water level is unperturbed by geohydrological testing, the tidal model with strain coupling reduces the observation efficiently, the normalised χ^2 of the least-squares fit dropping to levels below 2, and most often near 1.

However, it turns out that elevated noise levels prohibit in many cases sufficient precision of tidal parameter estimation and subsequently sufficient significance of solved fracture zone parameters. Barometric pressure effects were too uncertain to constrain the elasticity-dip angle correlation. Yet, a general, conspicuous tendency emerges, suggesting more or less the same azimuth angle for a presumed fracture zone in all borehole sections. The conclusion is that this feature has a regional character, either caused by a anisotropic state of strain in the bedrocks of Äspö or by interconnected fractures. Given that tides sense daily and subdaily changes the latter explanation appears unrealistic. The former explanations would need testing with 3-dimensional tidal strain measurement techniques.

1 Introduction

In the first part of this report (Scherneck, 2001, hereinafter referred to as SCH1) the basic theory of tides in boreholes was described along with ways to analyse recorded time series of water pressure in deep, confined boreholes. The problem involves global features (the tide rising potential and the deformation response of the earth on the planetary scale) and local features in the vicinity of the borehole (geological and tectonic structures, mostly fracture zones). In short, the water pressure in a confined section of a borehole is closely related to the pressure of the fluid in fractures intersecting with the borehole. In absence of such fractures, the fluid pressure is determined by the volumetric change of the surrounding rock. In any case the pressure changes are related to the changes of the general state of stress (tensor) in the surrounding rock mass. The tidal components of these variations can be computed from the tidal potential via tidal strain. This stage assumes laterally uniform layers. One perturbing effect, which can be added to the model in a straightforward way (SCH1; Scherneck, 2001b) concerns ocean tide loading.

The undisturbed state of strain in a uniform crust near the surface is taken as the boundary condition that controls the deformation of the local structure. A model by Bower (1983) was introduced that may explain the strain coupling coefficients in terms of a fracture zone that intersects with a borehole. In the fracture zone model, the strain implies stress exerted on the walls of a fracture, and the fluid filling the fracture transmits the pressure that balances the wall stress.

Near the earth surface (at the scale size of the tidal problem this implies practically the whole crust down to the Moho) several components of the tensors for stress and strain vanish. The state of strain is determined by three horizontal components, that can be combined as (1) Areal strain, (2) North-north-east-east pure shear and (3) North-east pure shear. In absence of a fracture in perfectly isotropic elasticity, shear would not imply any volume change and thus not affect borehole pressure. So the task boils down to determine coupling coefficients between borehole pressure and tidal strain including shear components. Since tidal North-east shear comes at 90° phase with respect to the tide potential and the volumetric change, (and North-north-east-east shear is in phase or in opposite phase), and since tidal strain components are mixed differently in the diurnal and semidiurnal bands, the ratio of tidal responses semidiurnal to diurnal bears a fingerprint of shear-strain coupling by means of the amplitude and the phase of this ratio.

The borehole tides can be analysed for certain details in the tidal response frequency. Such a study was presented in Scherneck (2001b). It is interesting mainly from a global perspective, involving effects that relate to the earth's core and the oceans. The fact that this can be done underlines the high data quality that is encountered in some series in SKB's data base. The earth core study was indeed carried out on the time series that turned out to have the highest tidal signal to noise ratio.

What cannot be done with a singular record from a singular borehole section is a critical test of the Bower fracture zone model. The missing piece to scrutinize the problem is the unknown actual state of strain in the region in general and in the local structure in particular. The present study was added where as many boreholes as possible were included. The results that were aimed at would comprise compilations of tide response parameters; similarly for surface air pressure; and the set of strain coupling parameters that can be determined independently for each data section. From the ensemble an overview will be gained whether the Bower model can be applied to detect whether a water bearing fracture intersects with a borehole section, what the tidal efficiency is in this fracture, and how the fracture is oriented. Finally, an attempt will be made to infer whether a fracture zone model is capable to explain the observed variation in strain coupling coefficients.

1.1 Prerequisits and definitions

In order to characterise the observations, a few parameters will be exploited. Most of these terms are familiar from statistics and time series analysis, like the **Signal-to-noise ratio (SNR)**. However, discrimination of a harmonic process in noise also depends on the amount of data. We will frequently use the ratio of the M2 tide amplitude to the **residual** standard deviation as the **tidal SNR (T-SNR)**. The standard deviation is thus an *a posteriori* quantity and reflects the power of the signals that are unaccounted for (our definition of noise).

It is ultimately the T-SNR that qualifies the determination of tide response coefficients, strain coupling coefficients, and eventually fracture zone parameters. We will need a quick-and-dirty method that allows a prognosis of the success of the tidal determination stage given a segment of data. A candidate segment can then be altered with respect to duration and weeding out of transients, until optimum segments are found. The conventional, wide-band SNR is no sharp indicator for this purpose. Instead, the tides need to be enhanced by band-pass filtering. For this measure we will use the term tidally filtered SNR or **F-SNR** in shorthand.

The notion of the residual standard deviation requires that a white-noise condition holds. To achieve this is a matter of conditioning of the time series using a whitening filter. For our purposes it is found that a **simple difference filter** D=(1., -1.), or in z-transform notation $D(\square)=1-\square$, does an excellent job. Using a two-hour sampling interval, the difference operation leaves the tidal frequencies well-preserved while proper random walk is perfectly reduced to white noise.

A **random-walk** noise character is typically what we find in our time series. Quite often, however, the power spectra indicate a low-frequency asymptote of $1/f^{\alpha}$ with $\alpha<2$, i.e. pink noise or flicker noise ($\alpha=1$). This means that proper random walk is a conservative assumption and the random-walk whitening filter might yield an over-whitened time-series. This affects the low frequencies and hence impedes investigation of long-period tides. However, previous studies using prediction-error filters for whitening did not result in sufficiently good T-SNR for the fortnightly tide. Therefore, results for **long-period tides will not be interpreted**; for the diurnal and subdiurnal periods over-whitening is not considered a problem.

The standard definition of SNR will also be used occasionally. For this we will compare the signal X submitted to the least-squares tidal analysis and the resulting residual X-S, each after the difference-filtering.

$$\mathrm{SNR} = 20\cdot_{10}\log\left(\frac{\mathrm{RMS}(D*(S+N))}{\mathrm{RMS}(D*N)}\right) = 20\cdot_{10}\log\left(\frac{\mathrm{RMS}(D*X)}{\mathrm{RMS}(D*(X-S))}\right) \qquad (1\text{-}1)$$

A worse problem is **stationarity**. We may distinguish nonstationary noise (external environmental perturbations) and nonstationary tide response. The former have a notion of being additive; subtracting the effect would yield a pure tide and barometric response. The second has a multiplicative notion as the tidal or barometric gain in the borehole may be reduced for a limit period of time.

The least-squares analysis will remove tidal signals and other deterministic components of the signal, and the noise consists of the variations unaccounted for. There are many examples of occasional transients that contradict the assumption of white noise or random walk. A large impact could be made on the SNR if the influence of e.g. pumping and other test studies could be modelled. In lieu of such methods the anomalous data samples must be ignored. The applied strategy of outlier detection is based on the least-squares residual, and employs data editing of samples falling outside a five-sigma interval before re-analysis. Of course there is a threshold of recognition. However, as long as these transient features are introduced only occasionally, have no temporal relation to the lunar hour angle, and do not correlate with atmospheric pressure, systematic perturbations of the tidal results will be small. That is to say that the data editing has limited impact on the solution and its shortcomings too. A critical example will be found in KAS04_1_A.

Occasionally we find periods in the tidal residuals where tidal variations are visible. The problem points out a change in the tidal response of the borehole-sensor-system. The least-squares tidal model cannot deal with this situation; the only remedy is to split the time series into shorter segments.

Another parameter of interest is the **Tidal efficiency (T-EFF)**. An ideal definition would imply that T-EFF = 1 if the observed tide (pressure, water head) equals the expected value in a simple reference case. However, an expected value is difficult to state because the geometry and confinement properties of the aquifer matter, so that a reference case would be rather far away from the encountered situation. In principle we know that closing of cracks and isolation conditions from the atmosphere increase with depth, promoting tidal efficiency. The forward prediction of tide amplitudes using a fracture zone model is part of this investigation, so the first of the three pressure-strain coupling coefficient is a scale factor away from a proper, dimensionless tidal efficiency measure. However, as we will see, the fracture zone model does not explain sufficiently well the variations between inter-tidal ratios from section to section.

A more convenient definition for T-EFF is the absolute value of the ratio between the rise of the water head and the rise of the external tidal potential, and we will have to keep in mind that this parameter is meaningful only as a relative scale, i.e. for comparison within the regional set of observations.

Finally, the **Barometric efficiency (B-EFF)** is defined as the ratio between the observed water head and the barometric pressure expressed in units of water column.

The term (**borehole**) **section** is reserved to a length interval of the borehole that was confined with packers. The section is marked up by adding a number to the name of the borehole. Associated is a time series of original observations. Out of these series new series will have to be prepared, employing some signal conditioning (mostly resampling at a constant rate). One section can thus give rise to several chunks of data that will be analysed one at a time. Since the aim is to obtain chunks that are as stationary as possible, numerical results like tide admittance coefficients will be associated with each chunk. We will use the term (**data**) **segment** for such a selection. In order to mark up the segments a letter is added to the section code. As an example, the length of KAS04 was divided into a number of sections (KAS04_1, 2, 3, 5, 6). For each one we will inspect one data segment (e.g. KAS04_1_A). In the case of KAS03 we will look at three data segments from the same section, KAS03_1_A, B, C).

2 Borehole Pressure Data Analysis

2.1 Data preparation

The original measurement series are sampled at roughly 2 h interval. However they are generally not sampled at integer hours, not at constant sampling interval, and different series are not sampled synchronously with each other. The time series analysis that follows, however, requires uniformly sampled series. Therefore the measurements were resampled on 2 h intervals at UTC 1:00:00, 3:00:00 etc using linear interpolation. All procedures that will be applied below can cope with a limited number of missing data, and the gaps may have arbitrary length.

Two examples are presented (Figures 2-1 and 2-2). They illustrate the relation between the original measurements and the time series that are obtained using linear interpolation. The first figure illustrates the behaviour of the interpolation algorithm at data gaps. The second figure shows the increase of data rate that was issued on March 21, 2000. With the longer measurement intervals before March 2000, the time lag between an original sample and the regular sampling instance is most often larger than several minutes, but with the high data rate, the maximum lag is most often less than one minute. Therefore, in the latter situation the interpolated time series have ordinates that are almost coincident with the discretisation levels of the measurement. The discreteisation error becomes thus a bit more conspicuous; however, the numerical effect on spectrum analysis and tidal analysis is similar once the series are down-sampled. We will see that the major problem caused by the wide discreteisation levels implies that the barometric response becomes uncertain and coherence between surface air pressure and borehole pressure is lost at diurnal and shorter periods.

2.1.1 Selection of data segments

Preparing the subsequent analysis the regularised time series are inspected for suitable segments. A simple filter is applied to give the series an appreciable degree of stationarity. The filter simply computes the successive difference between adjacent samples. When one of them is missing, the output is flagged missing. Similarly, if the absolute value of output exceeds a certain threshold (0.2 m change per two hours), it is flagged missing. The following properties are requested: few, short gaps and a good signal-to-noise ratio. Quantitatively:.

Ancillary data

Parallel to every borehole data segment two ancillary time series are prepared. They represent the air pressure near the laboratory and the sea level at Oskarshamn harbour. The data will first be used in the least-squares regression in order to avoid perturbations of tidal parameters. The date will also be used to determine dynamic responses of the borehole pressure using cross-spectrum estimation. For both applications, the data must be resampled at the synchronous rate of 2 h. In the case of the sea level, the original data is sampled at 1 h interval, and 1:2 subsampling after low-pass filtering is uncritical. In the case of air pressure data the original data is sampled at 3h intervals starting at

midnight UTC. The most straightforward method to arrive at 2 h sampling is to take every other value and to interpolate the two missing values in between using a linear scheme. Since the air pressure signal power at high-frequency is low, the interpolation noise of this short scheme is expected to be determined by the high-frequency signal power (standard deviation 1 hPa roughly).

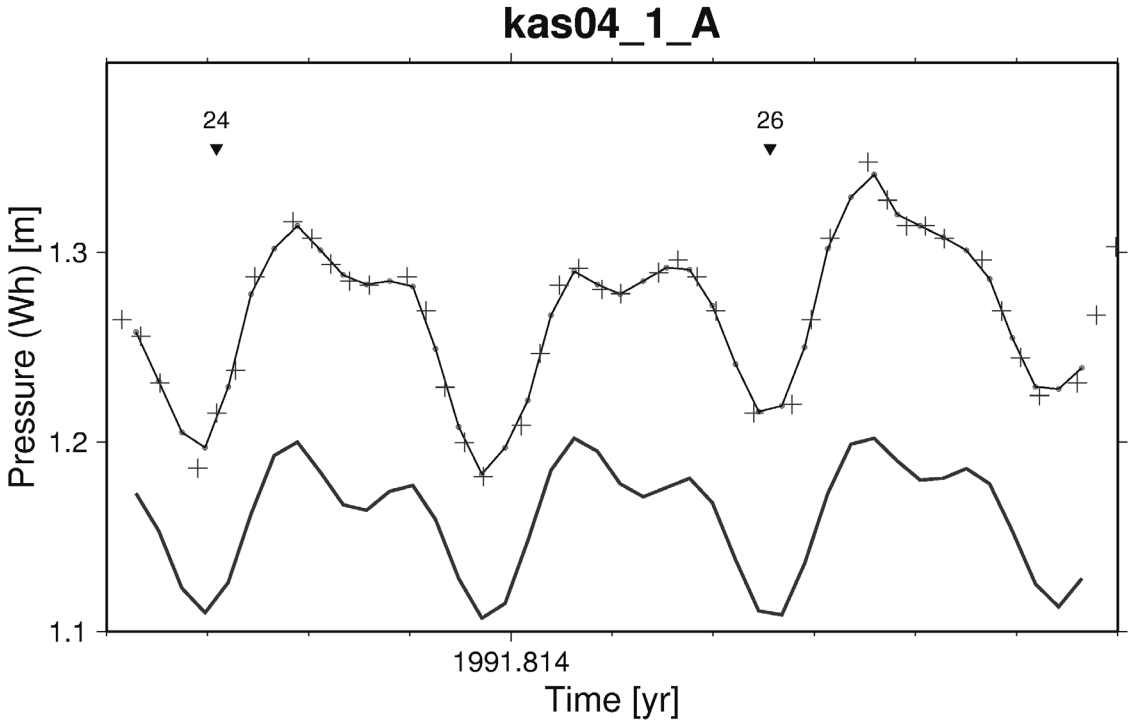

Figure 2-1. *This figure shows a section of original data (red crosses) and the regularized data in two-hour intervals (connected circles). Note that we do not interpolate more than two hours into a gap. The section shown is from Oct 24-26, 1991.*

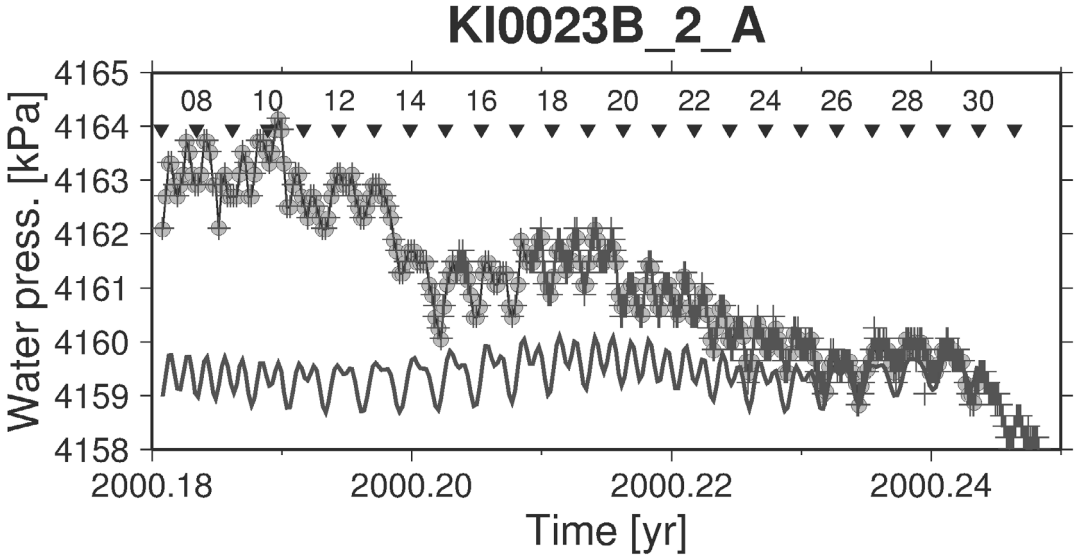

Figure 2-2. *Transition of low rate measurements and high rate measurements on March 25, 2000. The original measurements are shown as crosses, the regularised time series as filled circles. The curve in the bottom shows the tidal variations predicted for this borehole section.*

Table 2-1. Analysed data segments and tidal SNR. Missing SNR values where tide efficiency was very low. Date in transducer column specifies transition from relative to absolute. "Resl" means measurement resolution.

Section and Segment	Transducer Absol. / Relat.	Resl. [mm]	Begin	End	Number of samples Miss	Valid	Total	T-SNR [dB]
KI0023B_1_A	A	5	1999-10-23	2000-09-16	0	3960	3960	32.4
KI0023B_1_M	A	< 1	1999-10-23	2000-09-16	0	3960	3960	
KI0023B_2_A	A	5	2000-02-17	2000-12-23	22	3695	3717	31.2
	A	5						
KI0023B_8_A			2000-02-17	2000-12-28	22	3767	3789	31.1
KI0023B_9_A	A	5	2000-06-08	2000-08-20	0	877	877	26.8
KI0025F02_2_A	A	5	1999-10-23	2000-12-30	18	5192	5210	33.3
KI0025F02_9_A	A	5	1999-10-23	2000-12-30	18	5192	5210	31.5
KI0025F03_9_A	A	5	1999-10-23	2000-12-30	18	5192	5210	28.2
KA1061A_1_A	A	< 1	1993-06-22	1995-03-07	12	7470	7482	30.4
KA1131B_1_A	A	< 1	1994-05-11	1996-03-05	52	7924	7976	30.1
KA1755A_2_A	A	< 1	1995-10-14	1996-08-11	0	3625	3625	33.4
KA1755A_2_B	A	< 1	1999-10-23	2000-12-30	0	5208	5208	32.0
KA2511A_2_A	A	5	1999-10-27	2000-12-30	0	5164	5164	32.8
KA2511A_4_A	A	5	2000-01-26	2000-12-30	0	4071	4071	32.4
KA2511A_5_A	A	5	1999-10-24	2000-12-30	0	5202	5202	33.1
KA2511A_6_A	A	5	1999-10-25	2000-12-30	0	5189	5189	33.0
KA2563A_1_A	A	5	1999-10-24	2000-12-30	0	5195	5195	33.6
KA2563A_2_A	A	5	1999-11-16	2000-12-30	0	4925	4925	35.2
KA3110A_1_A	A	< 1	1997-03-21	1997-11-12	2	2824	2826	23.3
KA3600F_2_A	A	5	1999-10-23	2000-06-05	0	2712	2712	30.2
KAS02_3_A	R	< 1	1991-09-20	1992-05-30	163	2871	3034	32.3
KAS03_1_A	R, 1996-06-13	< 1	1991-12-15	1993-06-25	18	6681	6699	41.5
KAS03_1_B	A, 1996-06-13	< 1	1996-06-13	1997-03-18	56	3276	3332	38.0
KAS03_1_C	A, 1996-06-13	< 1	1999-02-24	1999-12-01	0	3359	3359	30.7
KAS04_1_A	R	< 1	1991-10-23	1992-10-01	36	4094	4130	14.8
KAS04_2_A	R	< 1	1991-10-23	1992-06-13	23	2789	2812	34.8
KAS04_3_A	R	< 1	1991-10-11	1992-02-27	9	1663	1672	28.1
KAS04_5_A	R	< 1	1991-10-22	1992-08-03	39	3391	3430	37.4
KAS05_2_A	R	< 1	1992-03-02	1992-06-18	3	1293	1296	25.3
KAS06_6_A	R	< 1	1993-06-21	1995-03-03	0	7433	7433	29.0
KAS07_1_A	R	< 1	1991-10-23	1992-01-21	0	1078	1078	20.4
KAS07_1_B	R	< 1	1992-05-13	1992-08-11	0	1089	1089	23.9
KAS07_2_A	R	< 1	1991-09-20	1992-02-27	124	1796	1920	22.4
KAS08_1_A	R	< 1	1991-10-23	1992-08-09	20	3475	3495	20,9
KAS08_1_B	R	< 1	1993-05-29	1993-09-02	0	1157	1157	25.0
KAS09_1_A	R, 1996-07-23	< 1	1993-07-07	1994-04-19	0	3428	3428	22.6
KAS11_1_A	R	< 1	1993-05-02	1994-07-28	0	5417	5417	32.8
KAS11_4_A	R	< 1	1994-04-25	1995-07-04	0	5217	5217	22.2
KAS13_1_A	R	< 1	1992-06-07	1992-08-23	0	921	921	21.8
KAS16_2_A	R, 1997-10-08	< 1	1995-12-05	1996-07-03	48	2486	2534	38.0
KAS16_2_B	A, 1997-10-08	< 1	1999-05-06	2000-12-28	5	7209	7214	3.2
KAS16_3_A	R, 1996-06-12	< 1	1995-06-23	1996-02-08	6	2757	2763	33.6
KAS16_4_A	R, 1996-02-29	< 1	1993-03-24	1993-09-11	0	2059	2059	10.3
KAS16_4_B	A, 1996-02-29	< 1	1999-05-06	2000-12-28	47	7167	7214	

KAS16_4_Z	R, 1996-02-29	< 1	1993-02-19	1993-12-07	0	3495	3495	0.6
KBH02_3_A	RA, 1996-06-13	< 1	1996-03-04	1997-01-31	84	3915	3999	26.0
KBH02_4_A	A, 1996-06-13	< 1	1996-06-14	1997-01-08	65	2435	2500	20.0
KBH02_5_A	A, 1996-06-13	< 1	1996-06-14	1997-01-08	66	2434	2500	20.3
KBH02_6_A	A, 1998-09-01	< 1	1996-06-14	1997-01-08	53	2447	2500	23.2

Data segment selection criteria

The objective in this study was to include as many borehole sections as possible. From each section data segments were to be extracted that permitted the determination of tidal with good confidence. For this matter the data series should extend over more than 0.5 years. During these relatively long stretches of time the data series needs to preserve its character.

Gaps would not matter for the analysis. However, one may suspect that after long periods of interruption or after very large perturbations, the stationarity of the borehole conditions is not warranted. Therefore, segment boundaries are imposed at gaps of several days or conspicuous changes of water head.

Although criteria can be stated for candidate data segments, validation will also need *a posteriori* review. For instance, a narrow passband filter can be used to target at a tidal and a non-tidal frequency. Comparing the two responses, a first parameter is obtained that would characterise the signal to noise ratio. Since such a filter can be made short, a comprehensive view can be obtained how the SNR changes over time.

The filter used here is 360 samples long, using a Hanning-window design, $F_k(\omega)=\cos^2(\pi k/2N)*\exp(ik\omega\Delta)$, $-N \le k \le N=180$, $\Delta=2$h. The tidal frequency selected for ω is M2. The frequency selected for comparison is located half-ways in between the diurnal and the semidiurnal band (1.5 cyc/d). I define for signal strength

$$S(\boldsymbol{x})=20\cdot_{10}\log(\mathrm{RMS}[\boldsymbol{F}(\mathrm{M2})*\boldsymbol{x}]/0.001) \qquad (2\text{-}1)$$

and for signal to noise ratio

$$\mathrm{SNR}(\boldsymbol{x})=20\cdot_{10}\log(\mathrm{RMS}[\boldsymbol{F}(\mathrm{M2})*\boldsymbol{x}]/\mathrm{RMS}[\boldsymbol{F}(1.5\mathrm{cyc/d})*\boldsymbol{x}]). \qquad (2\text{-}2)$$

Owing to the length of the filter the output series can be subsampled at e.g. $N/4$ (7.5 days in the example).

In each case the series $\boldsymbol{x}$ is derived from the 2h-sampled series by a differencing operation. The differencing operation amplifies steps and short transients. For outlier editing I remove data points that exceed 0.2 m change over 2 h. Unless such a situations arise at isolated places the filter output is discarded. Thus, the SNR plots will appear rather sparse. It will lead to a conservative suggestion of what data could be submitted to tide analysis. Four examples are shown in Fig. 2-3 to 2-6. The first one is for KAS03_1 where tides have been analysed successfully in the prestudy. The second one is for a borehole section with lower SNR and low transducer resolution (KI0025F03_9), the third one for a case of very low SNR (KAS04_1), and finally the problem case HA1960a. In the latter two cases plots of excerpts of the time series have been added in order to illustrate the kinds of problems that are encountered. Included in these plots are the tidal and nontidal components (as determined in sections), anticipating the tide analysis stage to be detailed below. This helps to exhibit unexplained signal features.

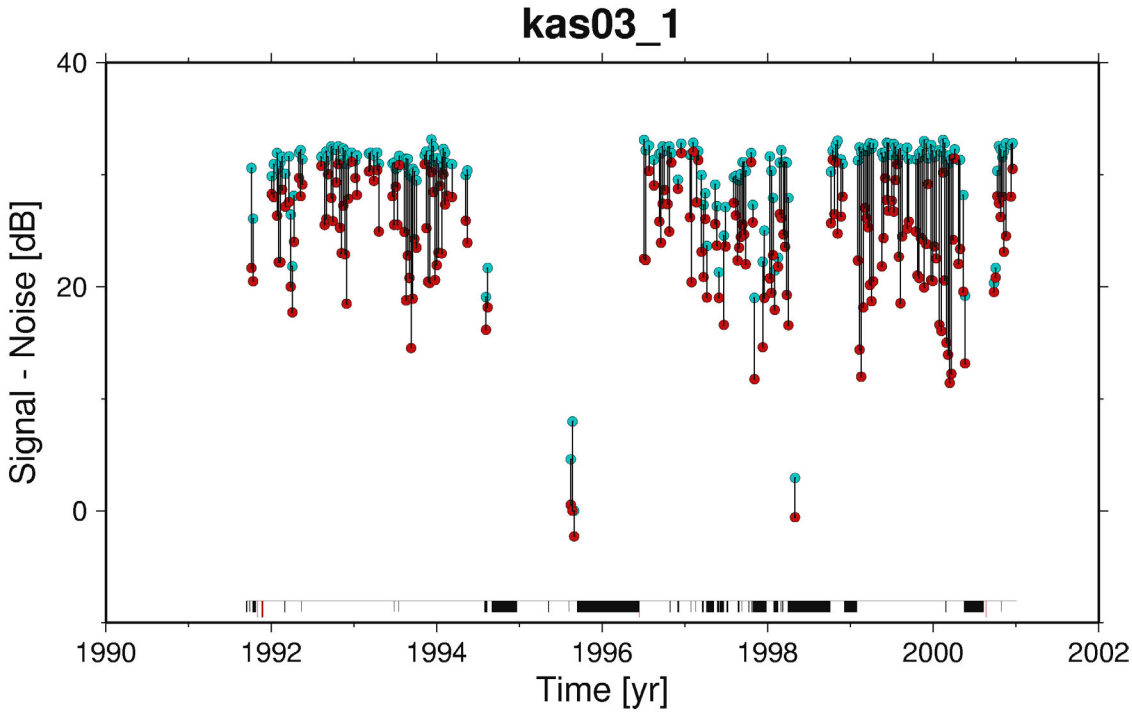

Figure 2-3. *KAS03_1. Six months from this borehole section, however from 1989, was used for the prestudy. Data with high SNR was consecutively obtained for another decade. This plot shows the signal strength of the M2 tide (green dots) in decibels with respect to a signal of 1 mm, the signal to noise ratio in decibels with respect to a noise band in between the tides (1.5 cyc/d, red dots). The SNR together with signal fragmentation was used to determine suitable contiguous data segments for tidal analysis. Signal fragmentation is indicated by the black and red bars in the lower part of the diagram. Red stripes indicate data missing from the start, black stripes data that is to be removed since it would exceed a criterion of maximum water head change (0.1 m/h).*

KAS03_1. Figure 2-3 suggests to pick three segments, (1) until 1995, (2) from second half of 1996 through first half of 1998, and (3) after spring 1999.The plot hints at rather unstable signal level in the mid segment (scattering green dots). SNR is highest in the last segment (indicated by the length of the black bars). In all, the signal level 30 dB diagnoses 60 mm M2 amplitude. Especially in 1999, signal is consistently 20 dB above intertidal noise. That segment has few gaps. In contrast, the mid segment contains many gaps already in the original measurement series.

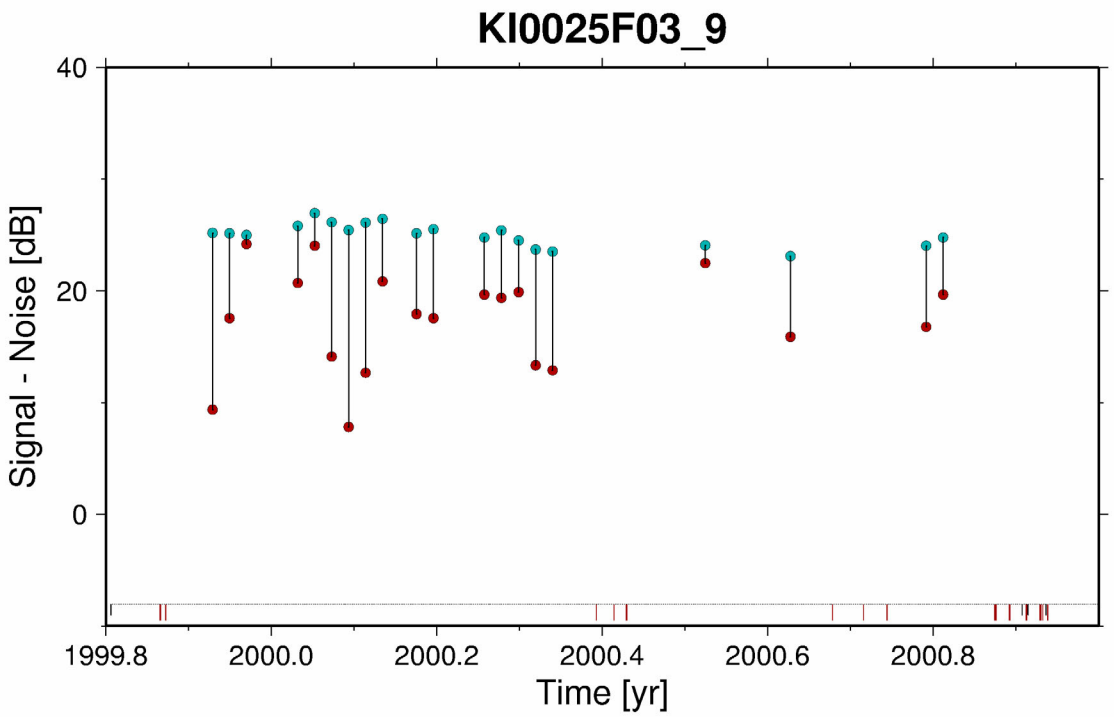

Figure 2-4. *KI0025F03_9 is an example for a section that has been observed only for a short time. The segment with acceptable noise and continuity extends only through the first half.*

KI0025F03_9. This section has only been observed in 1999 and 2000. Good, continuous data appears to be available only until March 2000.

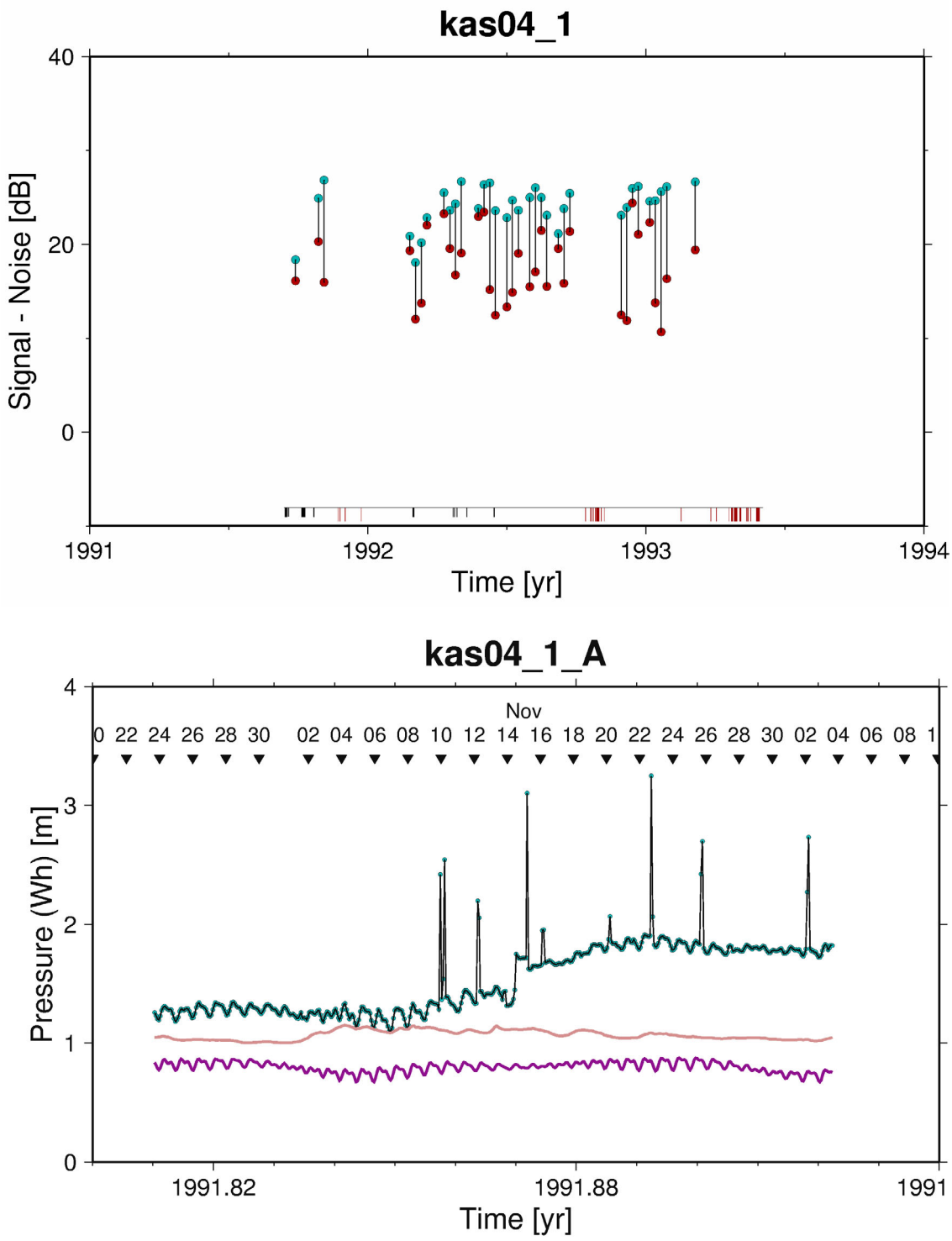

Figure 2-5. *KAS04. The lower diagram shows an excerpt from the beginning of segment 1. The segment that has been analysed extends from the start in autumn 1991 to October 1992. Transients as those appearing in this example, in fact all changes exceeding 0.2 m/h, are eliminated in the tidal analysis.*

KAS04_1. This section is an example for regularly good SNR, however it suffers from infrequent, large transients. After autumn 1993 perturbations are too frequent, so that the segment to be analysed had to be terminated at Oct 1, 1992

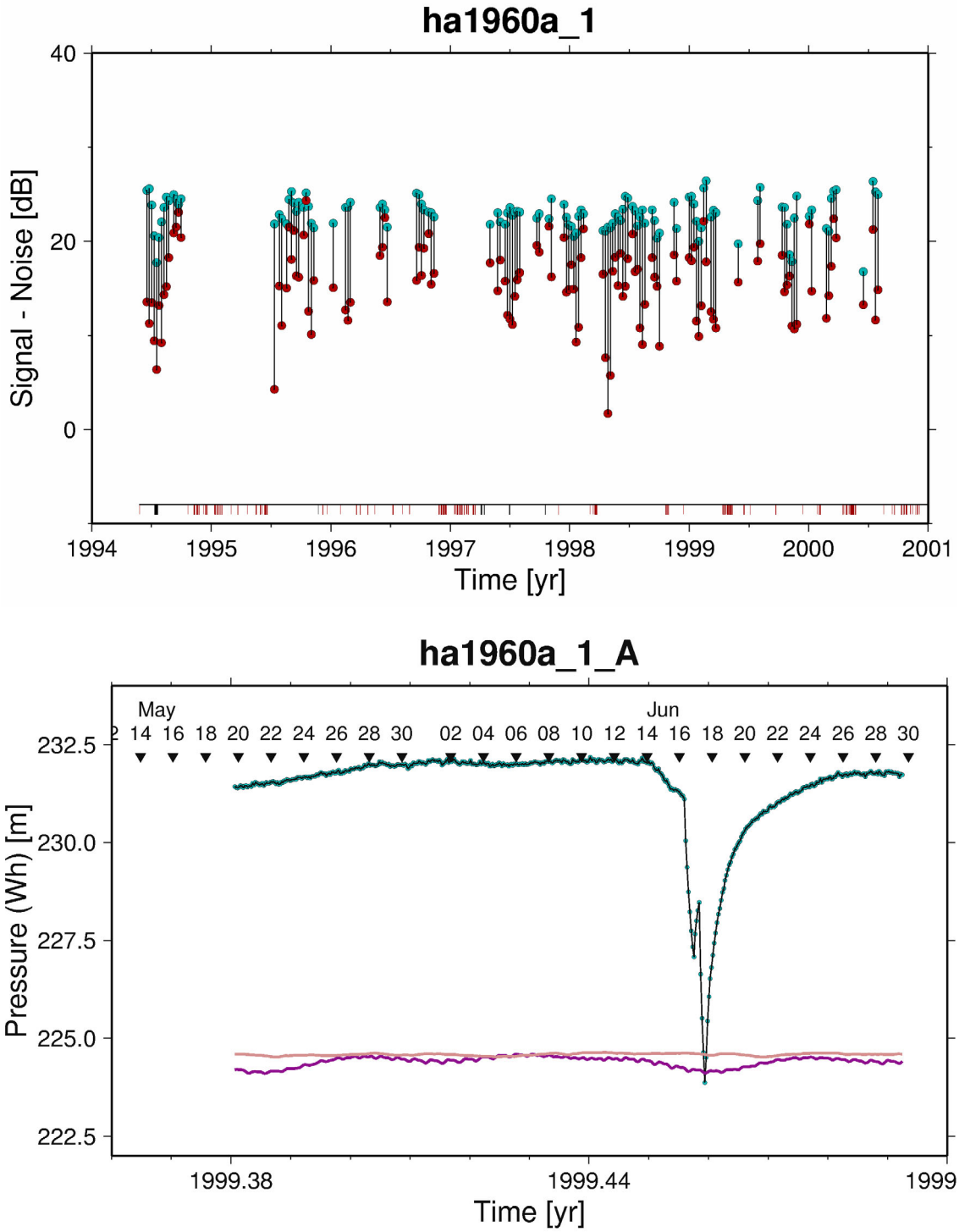

Figure 2-6. *HA1960a. Upper frame shows F-SNR plot for the M2 tide, lower frame an excerpt of the most promising time series segment. Upper frame shows signal (green dots) in dB per 1 mm and SNR (black bars) in dB. The time series plot shows the resampled observations (green dots), the empirical tide (purple) and the nontidal signals (admitted air pressure and sea level, orange)*

HA1960a. The F-SNR-plot suggests that tide analysis would not reach the 10 dB. M2 amplitude was determined at 15 mm. Visual inspection, however shows many tars and transients, too dense to derive a stationary data segment of sufficient length. Therefore the results were judged unreliable, and the series was discarded from further analysis.

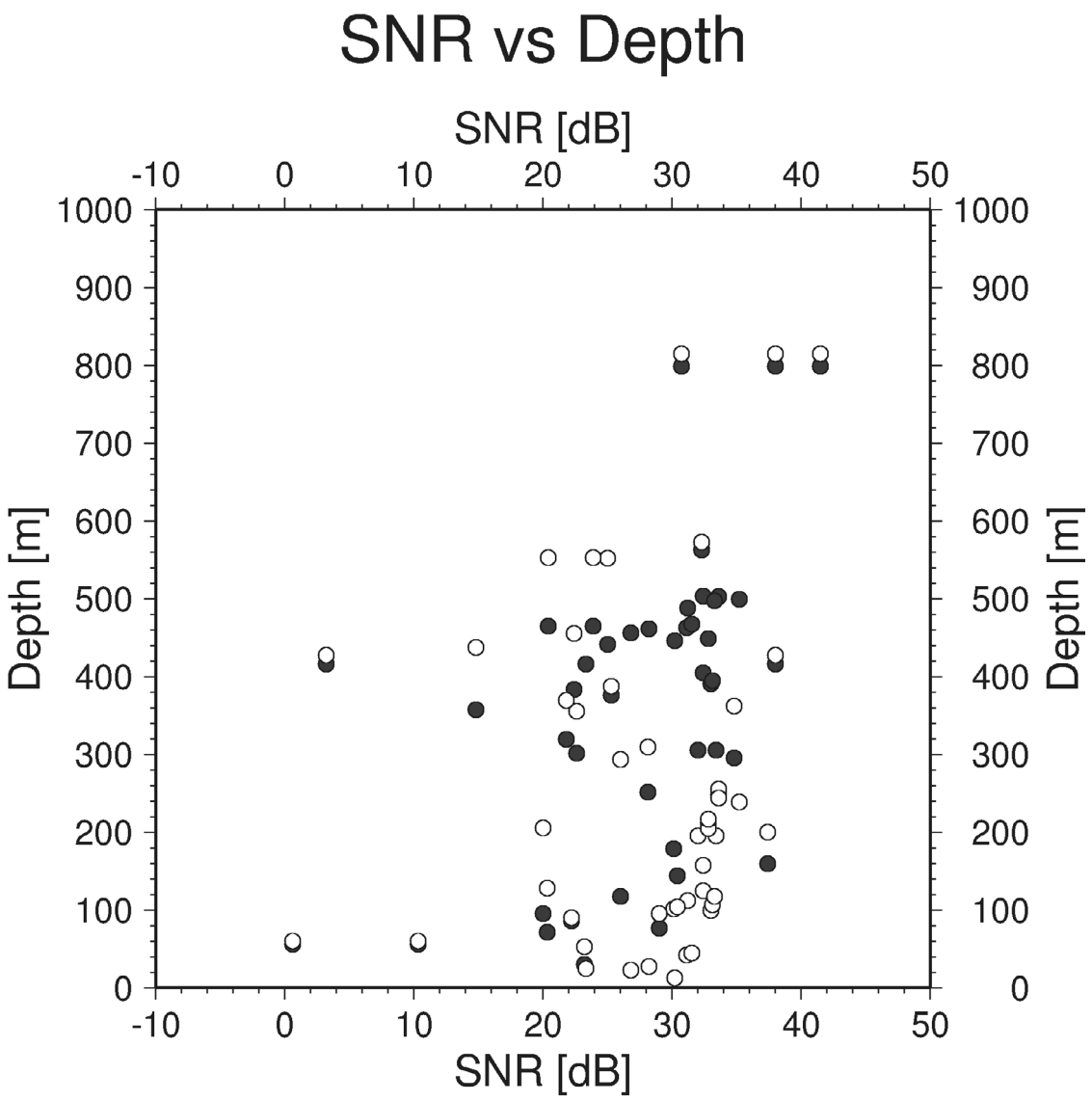

Figure 2-7. *Tidal signal-to-noise ratio (T-SNR) of the M2 tide component versus depth of borehole. Dark dots show the mean depth of the section below mean sea level, bright dots the distance of the section from the surface or tunnel. The most shallow sections show very low the sections very high T-SNR, but in between all combinations seem possible.*

In order to obtain a representative T-SNR figure for each data segment, the result of the least-squares tide analysis is used. Signal power is simply proportional the square of the estimated amplitude A. Noise power represents the variance of the least- squares residual and hence the square of the standard deviation σ_A. The T-SNR column in Tables 1 and 2 represents thus

$$\text{T-SNR}=20\cdot_{10}\log(A/\sigma_A)$$

The content of Table 2-2 is plotted in various combinations in Figures 2-7 to 2-10. Borehole sections and time segments with low tidal efficiency and low SNR are not promising for the fracture zone analysis.

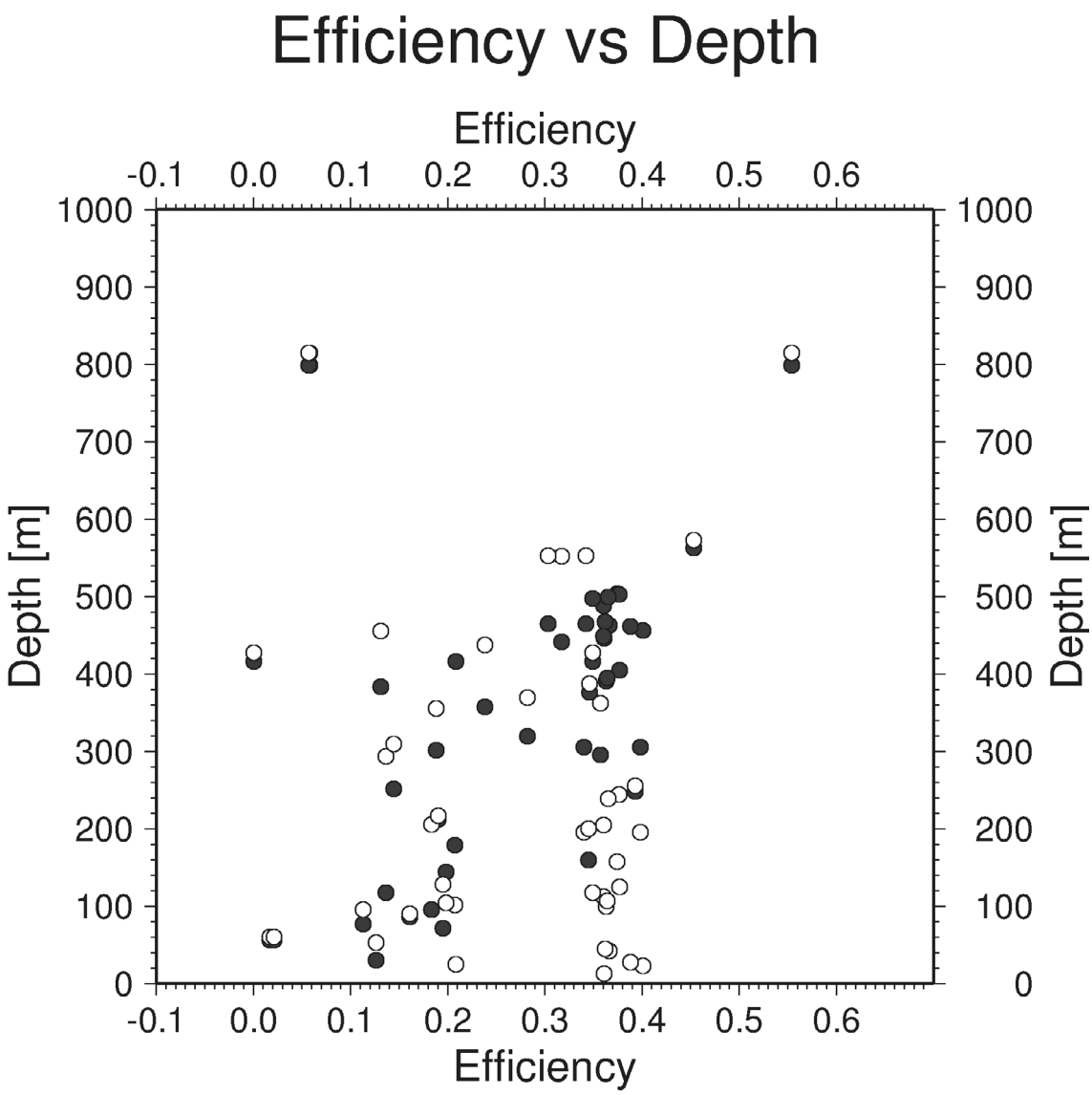

Figure 2-8. *Efficiency of the M2 tide versus depth, coded as in the previous figure. High and low efficiency appears to occur at all depths, possibly because some of the deep sections had leaky packers. With a few exceptions, a general increase of tidal efficiency with depth below sea level can be discerned.*

Plotting SNR versus T-EFF shows that the noise level is quite uniform across all series, and that low tidal efficiency is the major limiting factor for how small the confidence intervals can become.

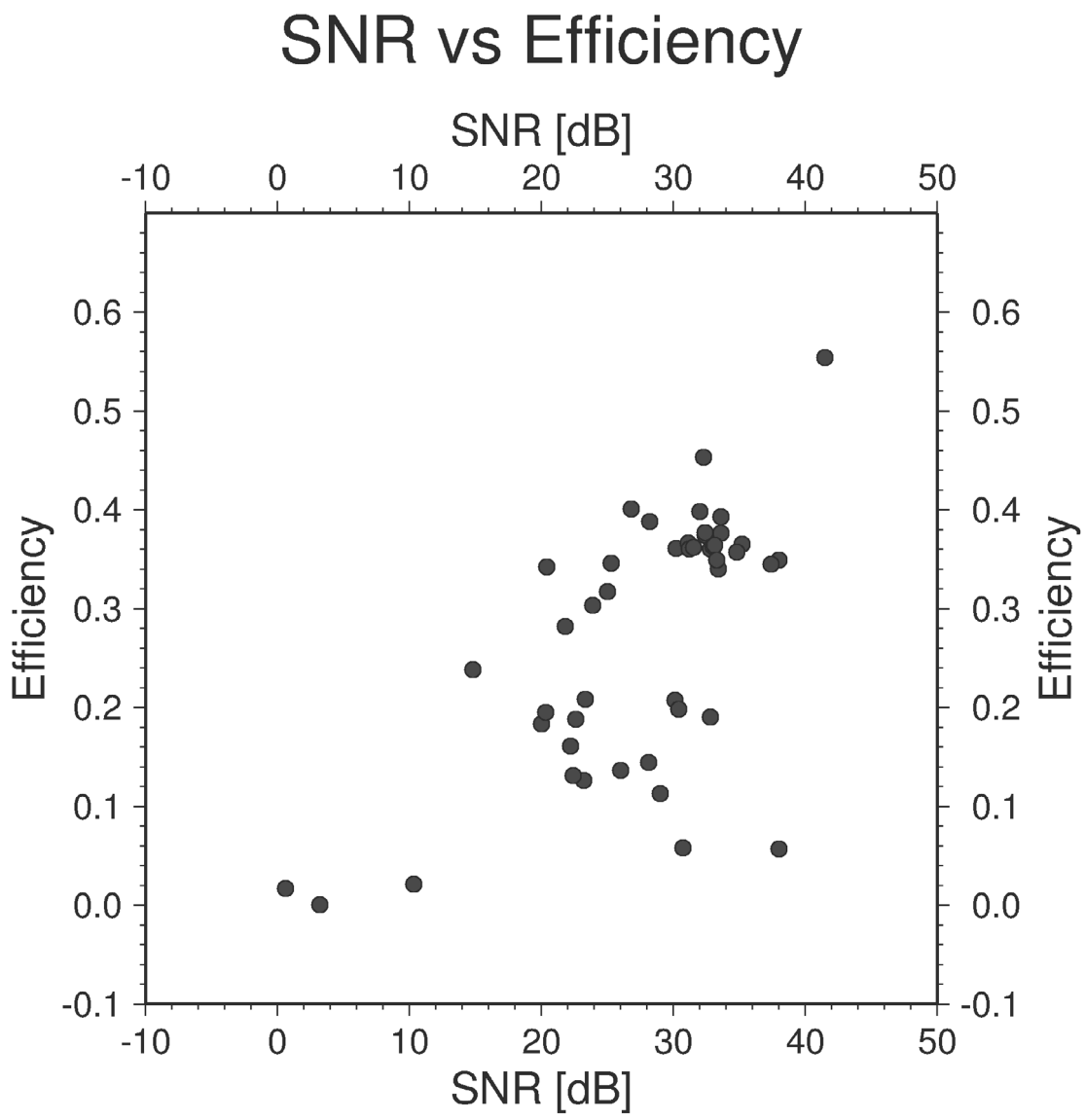

Figure 2-9 *Tidal efficiency versus tidal signal-to-noise ratio.*

Fig. 2-8 suggests that borehole depth (red dots) correlates better with tide efficiency than distance. T-EFF is plotted once more (Fig.2-10), but now only against depth, and the segments are labelled. One of the guiding parameters for tide response is the effective modulus of elasticity (Lamé´s λ). Crack density increasing to the earth's surface is an important factor that reduces the effective elasticity. Below 500 m the tide amplitude is following a straight line with only narrow spread. Below 500 m the spread increases considerably. Another reason for low efficiency could be intersection of the respective borehole with fractures having shallow dip. Such fractures are more difficult to sustain at greater depth. However, packer tightness needs to be considered, as indicated from comparing segments from identical sections, e.g. KI0023B_1_A and _M; KAS08_A and _B; and KAS16_2_A and _B

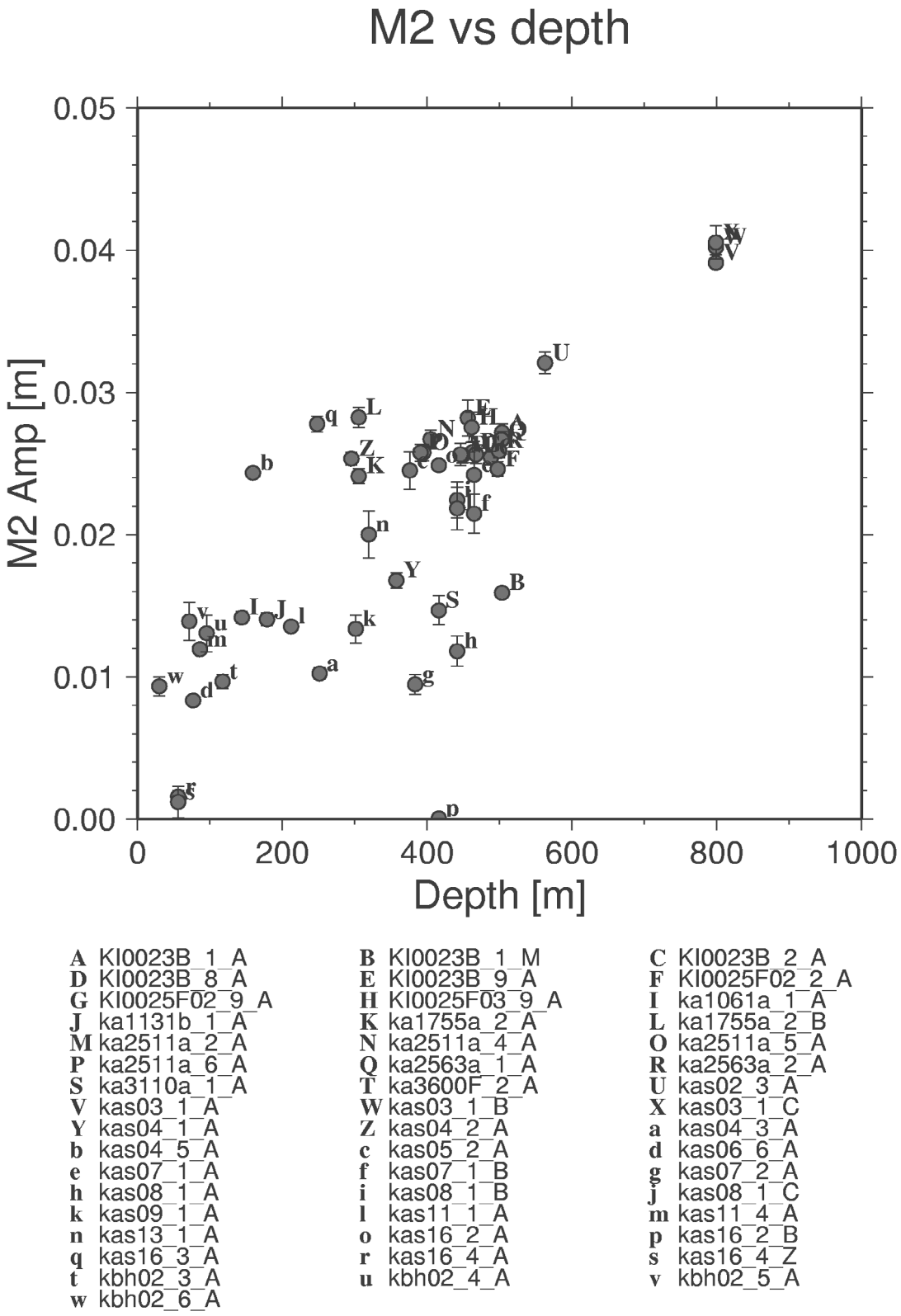

Figure 2-10. *Tidal efficiency once more, now only versus topographic depth, and data segments labelled.*

Interesting candidates for close attention are those with narrow confidence limits and high or low tide response at 300 to 500 m depth: KAS04_5_A, KAS16_3_A, KA1755a_2_A and _B (high M2-efficiency), and KAS07_1_A and KA3110a_1_A (low).

Table 2-2. Tidal efficiencies of the M2 wave in increasing order, T-SNR, and conventional SNR.

Borehole section	M2 eff	M2 amp	M2 pha	T-SNR	SNR	segment depth
data segment	[-]	[m]	[deg]	[dB]	[dB]	[m]
KAS16_2_B	0	0	139.8	3.5	1.1	415.8
KAS16_4_Z	0.017	0.0012	106.4	0.8	0.3	56.0
KAS16_4_A	0.021	0.0016	103.9	10.9	1.1	56.0
KAS06_6_A	0.113	0.0083	201.7	29.2	2.0	76.4
KBH02_6_A	0.131	0.0093	166.9	23.2	1.7	29.9
KAS07_2_A	0.134	0.0095	179.7	22.7	1.8	383.2
KBH02_3_A	0.137	0.0097	163.2	25.9	2.0	117.3
KAS04_3_A	0.144	0.0102	185.5	28.1	4.1	251.5
KAS08_1_A	0.166	0.0118	163.1	20.9	1.2	441.3
KAS11_4_A	0.168	0.0119	207.4	30.5	3.3	85.7
KBH02_4_A	0.185	0.0131	207.1	20.1	1.1	95.0
KAS09_1_A	0.189	0.0134	215	22.6	1.5	301.0
KAS11_1_A	0.190	0.0135	218	32.9	2.7	212.2
KBH02_5_A	0.196	0.0139	213.9	20.4	1.0	71.1
KA1131B_1_A	0.197	0.0140	221.7	30.1	2.7	178.9
KA1061A_1_A	0.200	0.0142	218	30.7	3.4	144.0
KA3110A_1_A	0.207	0.0147	201.3	23.3	1.3	416.0
KI0023B_1_M	0.224	0.0159	211.9	34.5	7.6	503.6
KAS04_1_A	0.237	0.0168	196.8	30.0	2.6	357.4
KAS13_1_A	0.282	0.0200	170.4	21.8	3.9	319.0
KAS07_1_B	0.303	0.0215	202.9	23.9	2.0	465.0
KAS08_1_B	0.316	0.0224	203.6	25.1	3.0	441.3
KA1755A_2_A	0.340	0.0241	212.9	33.5	4.0	305.5
KAS07_1_A	0.341	0.0242	204.4	20.4	2.7	465.0
KAS04_5_A	0.343	0.0243	205.1	3.08	8.4	159.4
KAS05_2_A	0.346	0.0245	195.6	25.3	4.1	376.2
KI0025F02_2_A	0.347	0.0246	209.2	33.5	4.9	497.3
KAS16_2_A	0.351	0.0249	180.7	38.0	7.3	415.8
KAS04_2_A	0.357	0.0253	203.8	35.0	8.0	295.2
KI0023B_2_A	0.358	0.0254	208.9	33.8	6.0	487.7
KA2511A_2_A	0.361	0.0256	204.6	33.4	4.6	448.9
KA3600F_2_A	0.361	0.0256	204.1	30.2	4.5	446.0
KI0025F02_9_A	0.361	0.0256	204.2	31.7	3.1	467.4
KA2511A_6_A	0.364	0.0258	202.4	33.0	4.0	390.4
KA2511A_5_A	0.364	0.0258	202.6	33.1	4.1	394.5
KI0023B_8_A	0.364	0.0258	203.1	31.1	3.7	462.6
KA2563A_2_A	0.365	0.0259	208.9	35.2	5.9	499.1
KA2563A_1_A	0.377	0.0267	210.2	33.6	4.5	502.6
KA2511A_4_A	0.377	0.0267	203.2	32.4	4.2	404.5
KI0023B_1_A	0.384	0.0272	155.8	32.4	4.9	503.6
KI0025F03_9_A	0.388	0.0275	209.6	28.2	2.4	461.5
KAS16_3_A	0.392	0.0278	207.7	33.9	3.2	248.2
KI0023B_9_A	0.400	0.0282	213.5	26.9	6.4	455.7
KA1755A_2_B	0.400	0.0282	212.6	32.0	3.5	305.5
KAS02_3_A	0.458	0.0321	205.4	32.5	4.7	562.9
KAS03_1_A	0.551	0.0391	201.5	42.2	11.6	798.9
KAS03_1_B	0.567	0.0402	203.4	38.0	10.0	798.9
KAS03_1_C	0.571	0,0405	203,1	30,6	4,3	798,9

2.2 Barometric response

At two stages in the analysis process admittance parameters are estimated for the effect of atmospheric pressure on the borehole record. We need to distinguish the following cases:

1. **Absolute pressure measurements.** The pressure in the borehole section is measured by a pressure transducer that works independent from the surface air pressure.

2. **Relative pressure measurements.** The pressure in the borehole section is measured relative to the surface air pressure.

In some cases the transducers were replaced from relative to absolute. In such cases the surface air pressure was subtracted from the absolute readings in order to continue the character of the earlier recording. These measures have been taken by Geosigma and determine the character of the acquired data. The analysis process has to take these changing conditions into account.

The barometric efficiency that will be reported below will be conceptually the relation between the pressure in the borehole section and the surface pressure. Assuming a linear relationship

$$p(\omega) = T(\omega) p_a(\omega) + p_t + \ldots \qquad (2\text{-}3)$$

where $T(\omega)$ is a transfer function that depends on frequency. The borehole pressure p is thus described as being composed of a part driven by the atmosphere p_a, a tidal part p_t, and other effects. In order to apply this concept uniformly to all records, the surface pressure must be added when relative sensors have been used. In particular, this means that surface pressure restoration is needed for the large amount of early surface borehole data.

For this restoration, pressure recordings from SMHI station Ölands Norra Udde have been used. The time coverage extends through all the analysed data sets. Comparison with SKB's own recordings at Äspö is shown in Fig. 2-11. The difference between the series consists mainly of a constant offset.

In the tidal analysis, the air pressure series is admitted presupposing a totally flat spectrum ($T \equiv c$, c a constant to be determined). This is not very critical as the atmospheric effect is mainly noticeable at the semidiurnal solar tides, a comparatively high frequency. The differencing operation on all time series prior to the least-squares fit will facilitate the admittance at high frequencies.

In order to obtain the frequency response spectrum $T(\omega)$ a simple tide analysis is performed resulting in a residual time series cleaned only of tides. Other predictable effects should be removed in a similar way before $T(\omega)$ is obtained from a cross-spectral analysis. In lieu of such information the hope stands to the atmospherically driven effect being sufficiently large so that the gain factor is determined with reasonably small uncertainty.

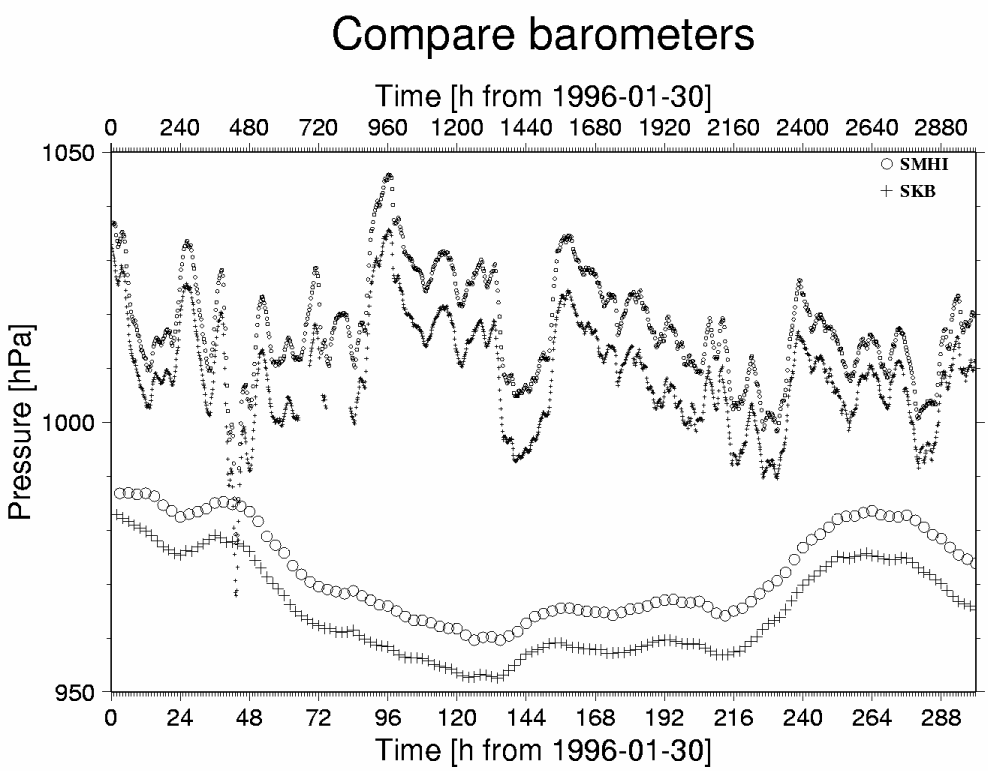

Figure 2-11. *Comparison of the barometric measurements at Äspö and observations by SMHI at Ölands Norra Udde*

2.2.1 Cross-spectrum analysis of the surface air pressure effect

In order to arrive at balanced conditions as to the high- and low-frequency tails in the gain spectrum, the time series to be subjected to cross-spectrum analysis are filtered with a prediction error filter (PEF). Its purpose is to yield a white spectrum of the effect represented in the denominator of the gain relation. In our case we have

$$T = \frac{p}{p_a} \tag{2-4}$$

so that we need a PEF for air pressure only. The same PEF will do in all cases. It was found that a filter order of 4 is sufficient. Then

$$T(\omega) = \frac{f(\omega)p(\omega)f^*(\omega)p_a^*(\omega)}{f(\omega)p_a(\omega)f^*(\omega)p_a^*(\omega)} = \frac{\mathbf{X}\{f*p, f*p_a\}}{\mathbf{P}\{f*p_a\}} \tag{2-5}$$

is in practice the employed formula, where **X** is the smoothed cross-spectrum and **P** the smoothed power spectrum (however, the series are actually filtered in the time domain).

Table 2-3. Barometric efficiency. Shown are the admittance coefficients with the smallest error limits in the frequency range between 0.1 and 1 cyc/d, one for every borehole section.

Section	admittance			freq.
	95% cfd min	average	95% cfd max	[cyc/d]
KI0023B_1_A	0.492	0.723	0.954	0.3281
KI0023B_1_M	0.461	0.613	0.766	0.5156
KI0023B_2_A	0.369	0.668	0.968	0.3281
KI0023B_8_A	0.476	1.038	1.599	0.7031
KI0023B_9_A	0.643	1.599	2.555	0.0469
KI0025F02_2_A	0.355	0.563	0.771	0.3750
KI0025F02_9_A	0.606	0.983	1.360	0.6562
KI0025F03_9_A	0.039	1.413	2.787	0.8906
KA1061A_1_A	0.866	1.008	1.150	0.2812
KA1131B_1_A	0.919	1.110	1.300	0.1875
KA1755A_2_A	0.410	0.724	1.038	0.1875
KA1755A_2_B	0.370	0.618	0.866	0.4688
KA2511A_2_A	0.426	0.680	0.934	0.4219
KA2511A_4_A	0.390	0.665	0.941	0.5156
KA2511A_5_A	0.675	1.145	1.616	0.1406
KA2511A_6_A	0.320	0.617	0.915	0.4219
KA2563A_1_A	0.369	0.582	0.795	0.4219
KA2563A_2_A	0.521	0.702	0.883	0.4688
KA3110A_1_A	0.472	0.911	1.349	0.2812
KA3600F_2_A	0.413	0.665	0.916	0.3750
KAS02_3_A	0.307	0.611	0.914	0.4219
KAS03_1_A	0.410	0.567	0.724	0.6094
KAS03_1_B	0.653	0.885	1.116	0.9844
KAS03_1_C	0.284	0.801	1.317	0.7500
KAS04_1_A	0.498	0.700	0.902	0.2812
KAS04_2_A	0.556	0.753	0.949	0.5625
KAS04_3_A	0.751	0.863	0.974	0.2812
KAS04_5_A	0.510	0.624	0.737	0.5156
KAS05_2_A	0.734	1.293	1.852	0.0469
KAS06_6_A	0.744	0.853	0.962	0.3750
KAS07_1_A	0.605	1.168	1.730	0.1406
KAS07_1_B	0.206	1.068	1.930	0.4688
KAS07_2_A	0.407	0.630	0.854	0.3750

KAS08_1_A	1.022	1.590	2.157	0.0469
KAS08_1_B	0.553	1.441	2.329	0.3281
KAS09_1_A	0.679	0.903	1.127	0.3281
KAS11_1_A	0.854	1.010	1.167	0.2812
KAS11_4_A	0.788	0.973	1.159	0.3750
KAS13_1_A	0.756	1.314	1.871	0.2344
KAS16_2_A	0.513	0.753	0.994	0.9844
KAS16_2_B	0.915	0.942	0.970	0.3750
KAS16_3_A	0.360	0.723	1.085	0.3750
KAS16_4_A	0.700	0.990	1.280	0.6562
KAS16_4_Z	0.915	1.532	2.148	0.6094
KBH02_3_A	0.753	0.936	1.119	0.3281
KBH02_4_A	0.698	1.024	1.350	0.4688
KBH02_5_A	0.624	0.997	1.371	0.4219
KBH02_6_A	0.828	1.078	1.329	0.0938

I show four examples for the cross-spectrum results, KAS04_3_A and KA1061A_1_A as cases for early measurements with relative and absolute sensors, respectively, and KBH02_5_A and KA2511a_2_A as cases for more recent measurements. KBH02_5_A is an example for an originally relative measurement where the effect of surface pressure was restored after the sensor change in order to change the character from absolute measurement relative. KA2511a_2_A is an example for a tunnel borehole section with an absolute sensor where the measured quantity is resolved at an equivalent of 5 mm water head.

The response of the sections is condensed into one parameter that represents the low-frequency response of the (restored) absolute pressure. This parameter is listed in Table 2-3 and plotted in Figure 2-16.

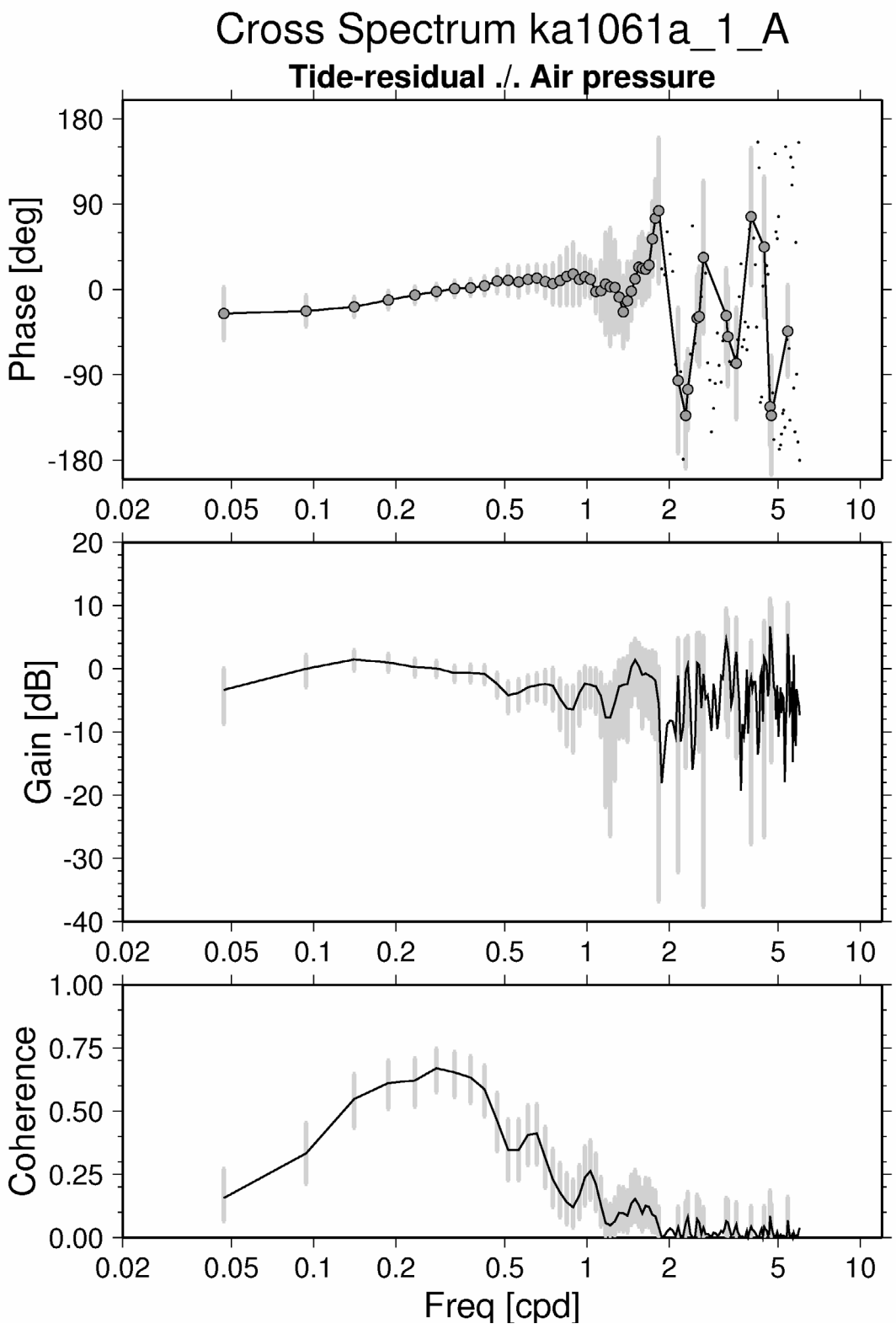

Figure 2-12. *Cross-spectrum analysis of borehole pressure in KA1061A_1_A in relation to surface air pressure. This section was observed with an absolute pressure sensor in 1993-5. Spectra for phase, gain and coherence are shown. The gain spectrum can be conceived as a spectrum of the barometric efficiency expressed in dB. The confidence limits (95%) are indicated by grey bars. No bars are shown where coherence is insignificant (where gain cannot be discerned from zero and phase could be any angle).*

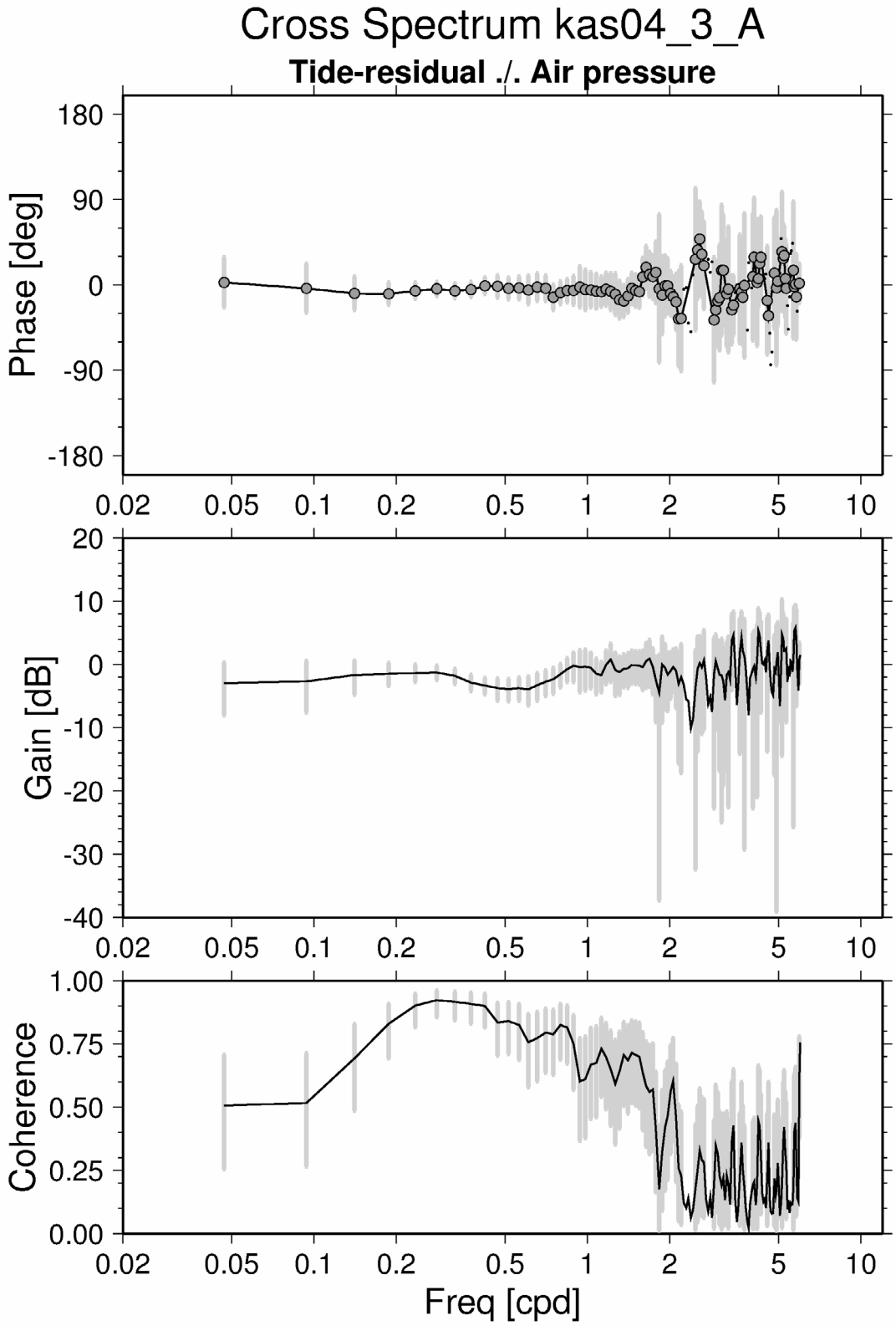

Figure 2-13. *Cross-spectrum of KAS04_3_A, This section was observed in 1991-2 with a relative pressure meter.*

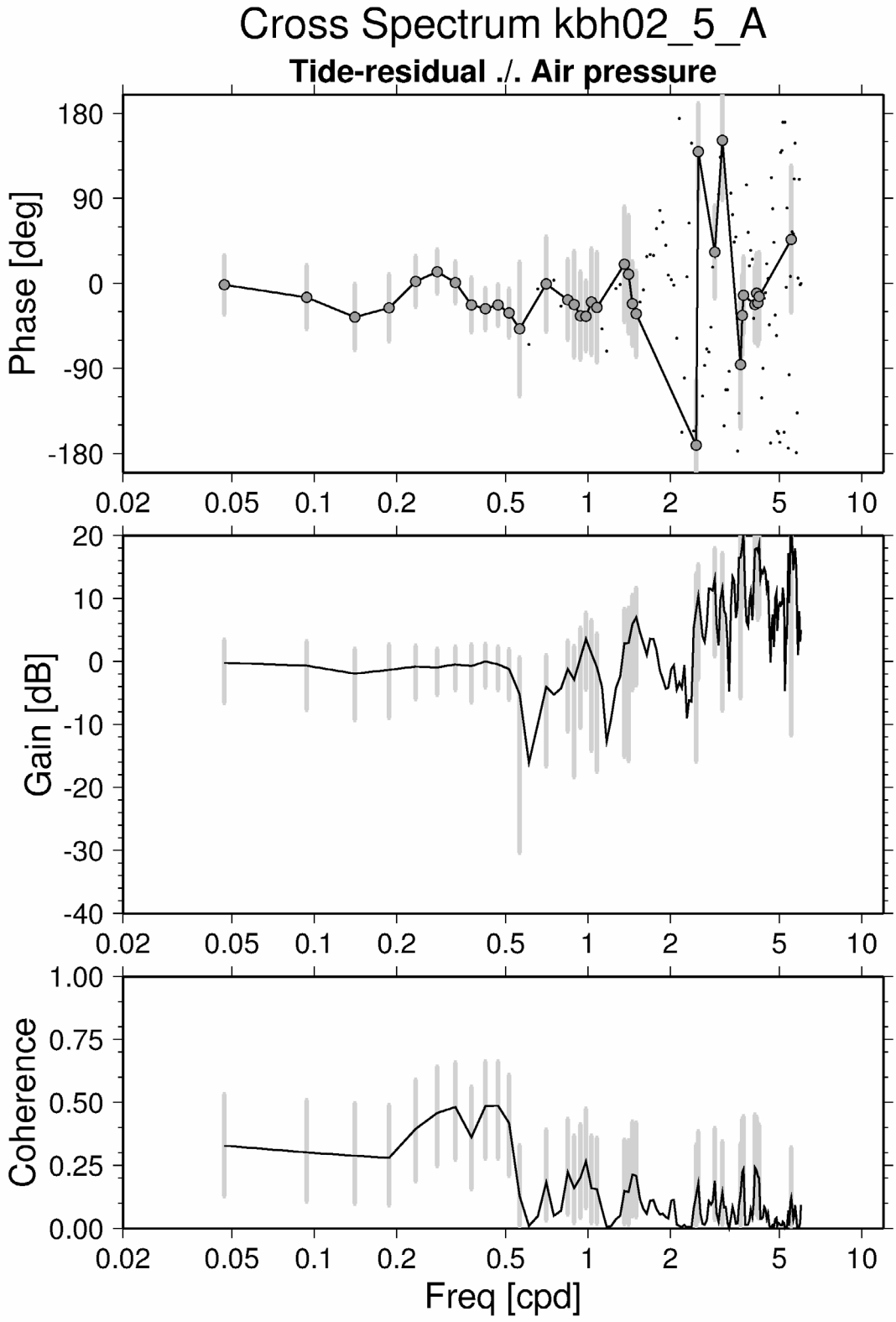

Figure 2-14. *Cross-spectrum for KBH02_5_A. This section was observed in 1996 –7 with an absolute sensor and converted to relative pressure a posteriori.*

2.2.2 Results barometric response and discussion

First we need to keep in mind that the way the borehole records are processed results in a relation between external pressure and absolute pressure in the borehole section. In most cases we find that the frequency response is flat; deviations are largely due to uncertainties in the estimates and confined to those spectral bands where air pressure power density is small. Highest coherence is usually found between 1 cyc/d and 0.1 cyc/d.

There are only a few cases where borehole pressure are low frequencies is significantly lagging behind the surface pressure. This behaviour hints at leaky confinement. The suspected borehole sections are KAS03_1_B, KAS03_1_C, KA1061a_1_A, KA1131b_1_A, and KBH02_4_A. The latter shows only marginal evidence for a lagged behaviour; a rather stable gain below 0.5 cyc/d is seen, so that the leak is certainly less strong than in the case of KAS03_1_B, where the gain increase extends up to 1 cyc/d. The leakage in KAS03_1_C is even more severe as the high-pass character extends throughout the whole frequency band. Finally, in both KA1061a_1_A and KA1131b_1_A the pressure relaxation affects only frequencies below 0.5 cyc/d, suggesting a quite intact tidal band.

The nature of the leak in data segment KAS03_1_B and more so in segment C is difficult to understand as it is accompanied by a high tidal efficiency. The mind-bogging feature is the high-pass characteristic accompanied by the typically increasing phase lag as frequency decreases. This means that the feature obeys causality. In comparison, KAS03_1_A has no significant phase lag but still a very low barometric and a high tidal efficiency. The change in behaviour occurs over time (the three records start in 1991, 1996, and 1999, respectively), see Fig. 2-18 for evidence. In B the pressure relaxation occurs below the tide frequencies. In C the relaxation extends to high frequencies, hence one should expect that the is affected. Figure 2-10, however, shows practically the same tidal efficiency in all three data segments. B and C have been recorded with an absolute sensor and the surface pressure has been restored. Since absolute pressure is the key parameter here, this step had to be undone. One could suspect a mistake in this process, but this would be likely to affect other records as well, which can be ruled out. Also it would be more likely that processing mistakes would show up as a signal in phase with the surface pressure. In B the cancellation (-10 dB) at low frequencies is a too critical condition to be reached by mistake. The series is not particularly noisy (SNR is 31 dB at M2 frequency). Yet, the coherence with surface pressure is rather low across the whole frequency band. The coherence is very low in C across the whole frequency band, so that one must conclude that the record segment is unaffected by surface pressure, not even through an elastic loading effect. The results pertaining to A and B are contradicted. A severe dating problem could explain this behaviour.

The following sections have anomalous air pressure response: KAS16_2_B and KAS16_4_Z. In either case relative transducers were used. The inferred absolute pressure in KAS16_2_B practically equals the surface air pressure. In the cross-spectrum analysis the section shows perfect coherence with the barometric record. Also, the tidal efficiency is found to be zero. These circumstances hint at packer failure where the leak is upward. In KAS16_4_Z the barometric efficiency is near unity, but coherence is low. Also the tide amplitude is low but not as low as in KAS16_2_B. Thus this section seems to be partially unconfined, and the leak would probably be downward.

Finally there are cases where we have low coherence at low frequencies (in spite of maximum spectral power in the excitation), eventually extending to diurnal periods, but where the least-squares adjustment has determined a high-frequency admittance near 0.5 with medium uncertainty. An example is KI0025F03_9_A. Also the M2 tide response is found at a midrange value. This is a section measured with an absolute sensor, so there is no surface air pressure information restored. There is no obvious reason for bad surface pressure coherence, so the conclusion is that this section has exceptionally noisy measurements.

A general trait, however, is that we find large confidence limits. This implies that including the barometric response in the fracture zone model will add only weak constraints to the modelling. The tidal information is the more critical information. It can be foreseen that we will get narrow bounds for the fracture zone azimuth, and wide bounds or even unstable solutions of the fracture zone dip.

The gain factors that are found (see Table 2-3 and Fig. 2-16) are in many cases compatible with the fracture zone model described in SCH/1, i.e. between 0.7 and 1. However, in about 15 cases (1/3 of the surveyed time series) the efficiency parameters are near or below 0.6. At high dip angles, the response could be as low as 0.7 but rather not lower. Because of the large uncertainties these findings are not critical. With respect to constraining the fracture zone model, the barometric response will have little impact except generally favour steep fracture zone angles.

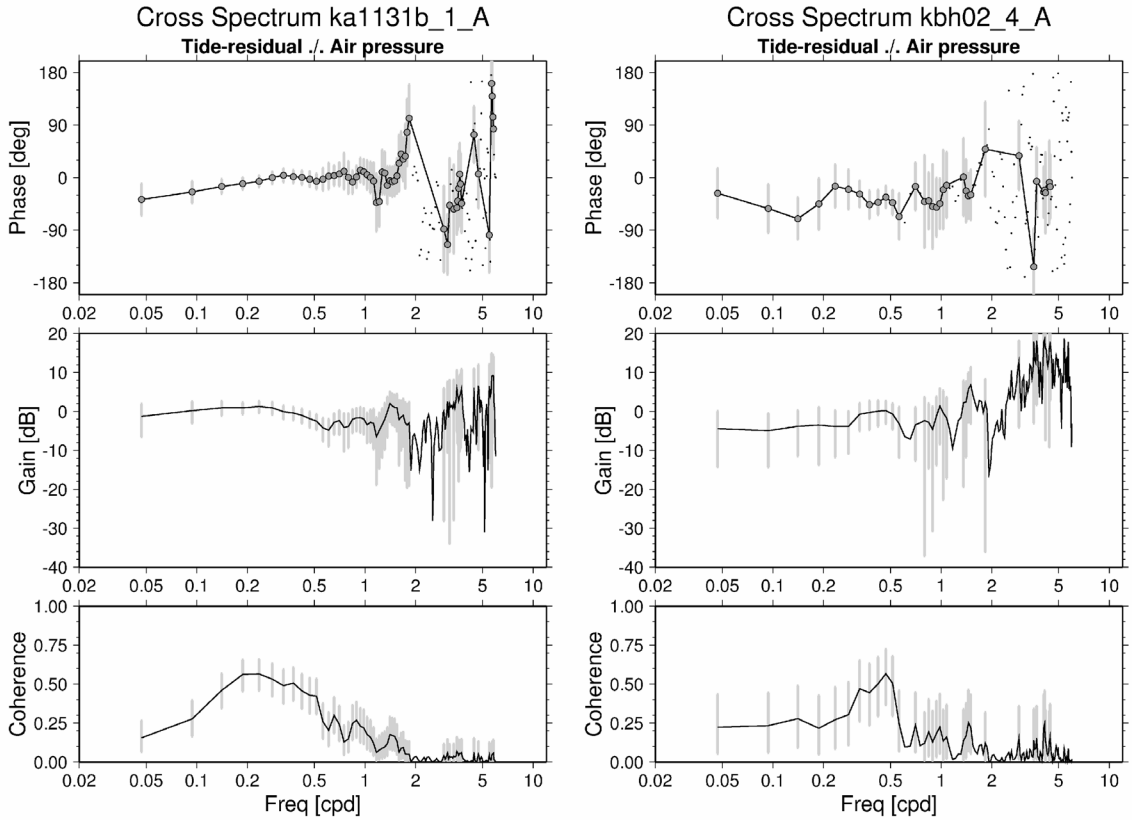

Figure 2-15. *Cross-spectrum of two sections where significant phase lag at low frequency was found.*

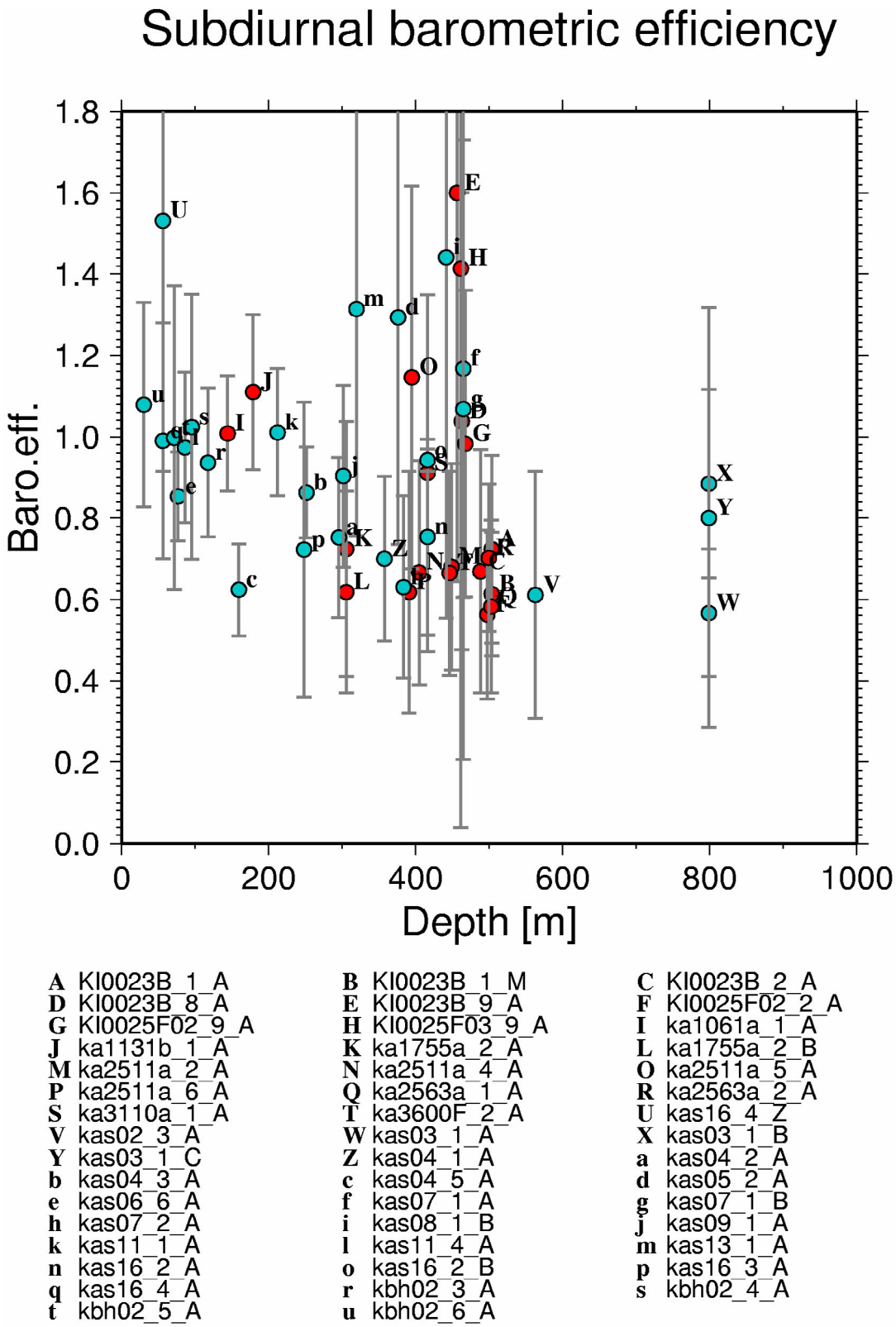

Figure 2-16. *Results from cross-spectrum analysis. Blue symbols represent surface boreholes (with relative pressure measurements), red symbols tunnel boreholes (absolute pressure). The barometric efficiency is taken from Tab. 2-3. It represents the sub-diurnal frequency range, the band where substantial spectral power in surface air pressure exists. In almost all cases the frequency response of the borehole sections is flat with a phase lag insignificantly different from zero. Exceptions are discussed in the text.*

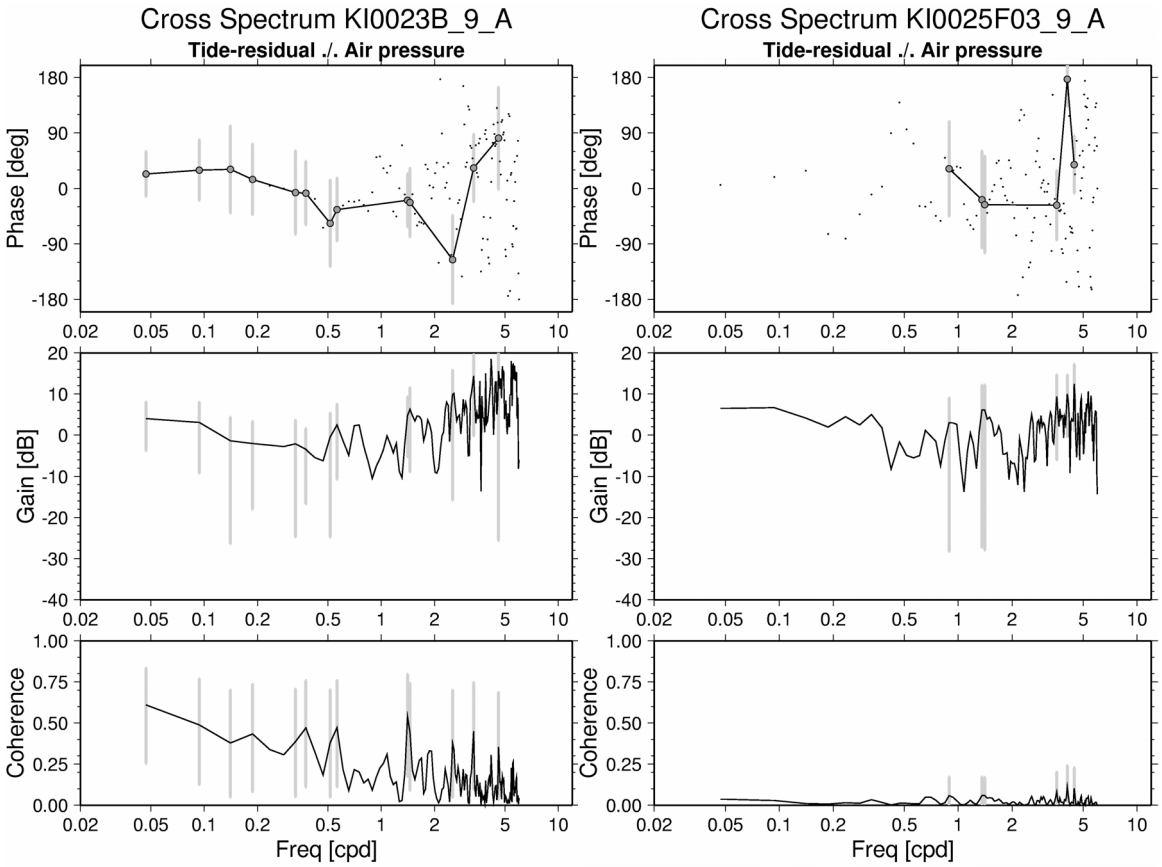

Figure 2-17. *Two examples for virtually high gain at high frequency, however accompanied by insignificant coherence. Both borehole series are sampled at 0.5 kPa resolution, so the anomalous gain can be explained by discreteisation noise. In the case of KI0023B_9A shown to the left, low-frequency gain is above unity too; however, the confidence interval includes* 1.

Several barometric efficiencies are determined at values greater than unity. These anomalies occur always when coherence is small. Similarly, in some gain spectra the gain at high frequency is found to exceed unity. Also here, coherence is always small. The gain value in the latter case is the square root of the ratio of the noise powers. In the absence of other signal this residual noise would typically be the discreteisation noise. In those cases where sections are sampled with 0.5 kPa resolution, and air pressure with 1 hPa, the gain value must be expected to approach 5. This is indeed the case in the two examples KI0023B_9_A and KI0025F03_9_A shown in Fig. 2-17.

However, KI0023B_9_A does show significant coherence at low frequencies, and gain values above unity. The coherence spectrum with falling coherence versus frequency is indicative of the rounding noise becoming more and more severe as the signal power decreases. No air pressure reduction for this section was carried out, since it is measured with absolute transducers. Carefully re-running the analysis re-assured that absolute pressure was acknowledged in the procedure. So the only comment that remains plausible for this case is that the confidence limit does include the value of unity (which is the physical limit). A calibration error would be the only alternative explanation.

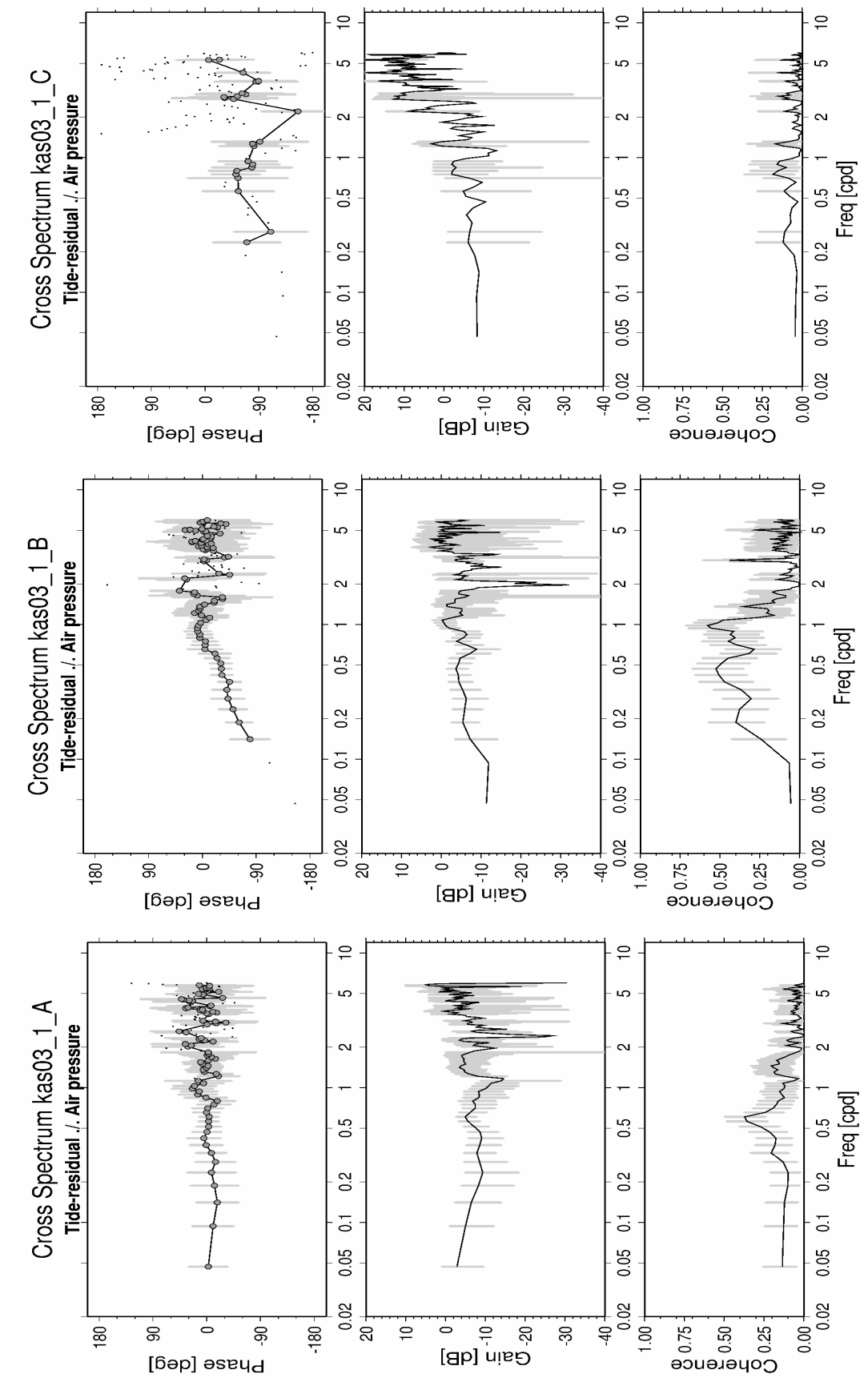

Figure 2-18. *Cross-spectrum for KAS03_1 at three different observation periods, starting in 1991 (A), 1996 (B), and 1999 (C), respectively. Segments B and C have been recorded with absolute pressure sensors.*

2.3 Tidal analysis

So far the discussion has involved the barometric response and the M2 tide. The central part of this report is devoted to the tidal response in both of the fundamental bands, the semidiurnal and the diurnal. As shown in SCH1 phase and amplitude information from these bands allow to uniquely solve for three strain coupling coefficients owing to the particular strain regime that is associated with each band.

The tidal results will first be derived from least-square fit of the tidal model to the borehole data segments one-by-one. The data is prepared in the usual way, i.e. sampled at two-hour interval and differenced in order to have near white-noise conditions. Simultaneously included in the fit are observed time series of air pressure at Ölands Norra Udde and sea level at Oskarshamn harbour. A bias and a rate are also estimated. The borehole data is not changed with respect to absolute or relative sensors; the original character of the observations is kept. The barometric admittance factor coming out of the least-squares fit will be less than zero in the cases when the relative transducers have been employed, so that addition of +1 to the factor will transform the notion of the coefficient from relative to absolute. The latter is in agreement with the standard definition of barometric efficiency.

The tidal model is based on Tamura (1987). The long segments, like KAS03_1_A, can utilise more tide wave groups; primarily the P1 and K1 tides can be discriminated. The associated frequency band setup can be seen in the table in Fig. 2-20[1]. This table is the main result output of the least-squares program. Segments that are shorter than six months do not allow spectral separation of the P1 and K1 tides. In this case these frequency bands were joined together and the response was represented with one admittance coefficient.

The tide analysis can be conceived as the splitting up of the input time series into a tidal part, a predicted nontidal part (due to surface air pressure and local sea level loading), and a residual (that could be further investigated). An example is shown in Fig. 2-19 covering a complete segment (KAS16_3_A, starting 1995-06-23 and ending in 1996-02-08, comprising of 2763 samples of which 6 are deleted or flagged missing. (Constant trends have been reduced in the figure.)

[1] Because of problems with MS-Word to import ASCII-files and showing them sideways the data had to be inserted into this document as a figure.

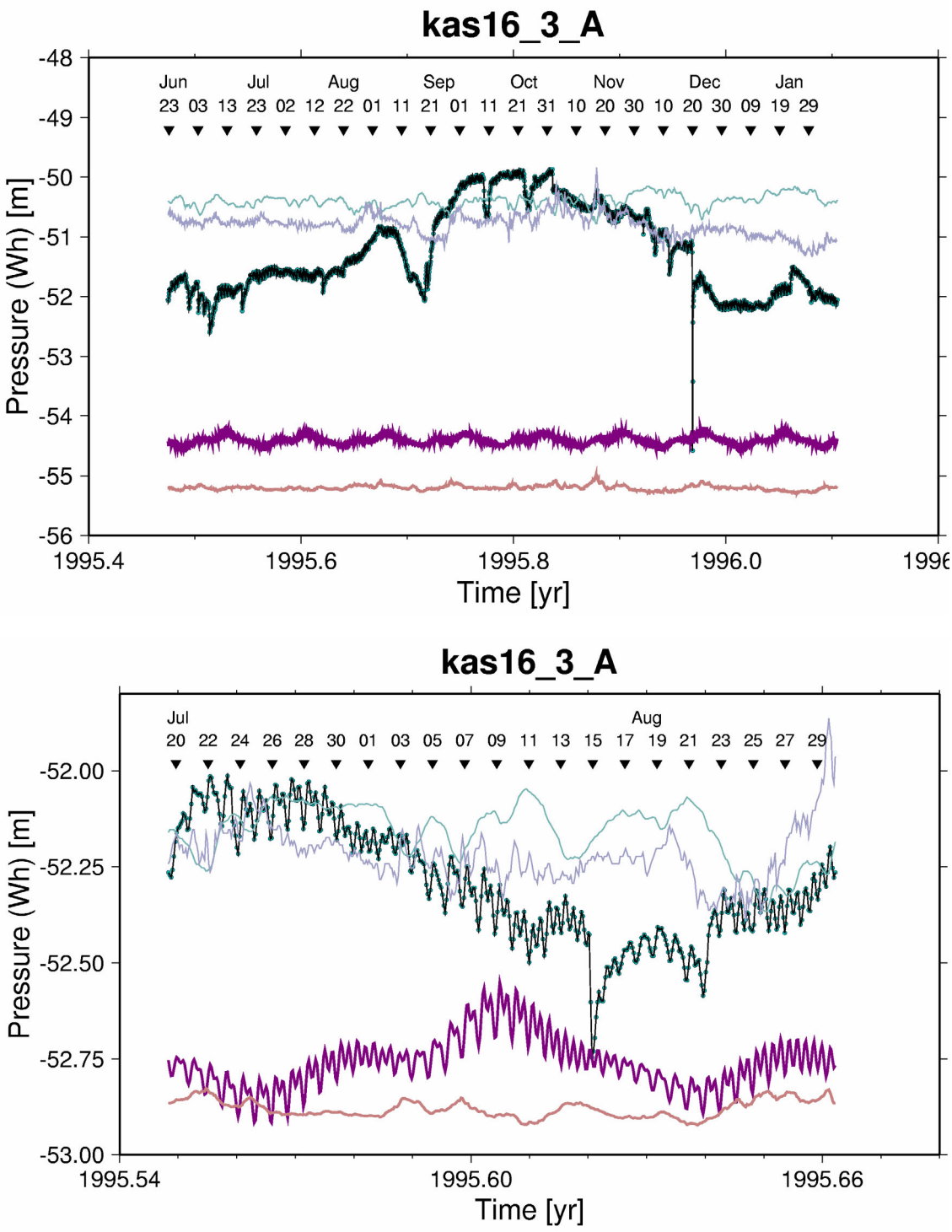

Figure 2-19. *Decomposition of observation segment KAS16_3_A (dark green) into a tidal (purple) and deterministic nontidal (pink) part. The top diagram shows all data, the bottom a 1000 h long excerpt. The deterministic component blends together barometric pressure (light-blue), sea level (light green), and a constant drift rate (suppressed). This series has relatively high tidal efficiency and medium barometric efficiency. Yet, the largest excursions of this time series are unaccounted for, and the long-period tides are probably exaggerated. For improved readability a uniform trend has been removed from all time series, and all curves except the observations have been moved to convenient ordinate positions.*

RESULTS: ADMITTANCE

SITE/FILE: kas03_1_A_wh.ts lon/lat: 16.6700 57.4550

Normalized chi^2 of fit : 1.04D-04, R= 1.02D-02 , X_1 X_2 = 1.00 2.30, Nev=46
The error information below is compatible with a unit normalized chi^2.

	#b	Dominating tide argum.numbers	Frequ. [cyc/d]	Amplit. [m]	Phase [deg]	Co..admittance parameter..Quad +- 68.3% conf	Gain	Cophase
Mm	1	2 0 1 0-1 0 0 0	.0362916	1.239D-02	70.4	-.047545 +-1.186232 .884990 +-1.190284	.886266	93.1
Mf	3	2 0 2 0 0 0 0 0	.0732022	2.346D-02	192.6	-.184614 +-.300125 -.183701 +-.300577	.260439	224.9
Mt	5	2 0 3 0-1 0 0 0	.1094338	4.491D-03	83.0	-.665885 +-.984463 -.413742 +-.975869	.783955	211.9
Sig1	7	2 1-3 2 0 0 0-1	.8618093	2.809D-03	330.9	-.219247 +-.164974 -.169602 +-.165073	.277190	217.7
Q1	9	2 1-2 0 1 0 0-1	.8932441	1.757D-02	286.8	-.336355 +-.044758 -.072156 +-.044799	.344008	192.1
O1	11	2 1-1 0 0 0 0-1	.9295357	9.151D-02	177.2	-.346556 +-.006935 -.074451 +-.006957	.354463	192.1
M1	13	2 1 0 0 1 0 0 1	.9664463	7.138D-03	119.4	-.489292 +-.195324 -.033549 +-.195212	.490441	183.9
P1	15	2 1 1-2 0 0 0-1	.9972621	3.943D-02	23.9	-.391041 +-.013750 -.075806 +-.013777	.398321	191.0
K1	17	2 1 1 0 0 0 0 1	1.0027379	9.450D-02	12.9	-.389007 +-.005847 -.071965 +-.005870	.395607	190.5
J1	19	2 1 2 0-1 0 0 0 1	1.0390296	7.393D-03	260.1	-.461647 +-.104695 -.021849 +-.104603	.462163	177.3
001	21	2 1 3 0 0 0 0 1	1.0759401	4.008D-03	22.4	-.421526 +-.109674 -.123432 +-.109700	.433226	196.3
3N2	23	2 2-3 2 1 0 0 0	1.8282556	5.237D-04	90.3	-.141782 +-.505126 -.245762 +-.504634	.283727	240.0
2N2	25	2 2-2 2 0 0 0 0	1.8645472	2.166D-03	340.7	-.476257 +-.107171 -.150333 +-.107190	.493420	162.5
N2	27	2 2-1 0 1 0 0 0	1.8953820	1.357D-02	296.6	-.518067 +-.035469 -.106820 +-.035413	.528965	168.3
M2	29	2 2 0 0 0 0 0 1	1.9322736	7.087D-02	187.0	-.540078 +-.004268 -.113670 +-.004264	.551910	168.1
L2	31	2 2 1 0-1 0 0 0	1.9685653	2.003D-03	257.5	-.563999 +-.241032 -.202115 +-.241341	.599120	199.7
S2	33	2 2 2-2 0 0 0 0	2.0000000	3.297D-02	33.3	-.535788 +-.008271 -.142902 +-.008267	.554518	165.1
K2	35	2 2 3 0-1 0 0 0	2.0417675	5.010D-04	90.1	-.119369 +-.492663 -.059899 +-.492973	.133555	153.4
3 1	37	3 1 0 0 0 0 0 2	.9661368	1.755D-03	273.5	-.620954 +-.991982 -.705713 +-.991314	.940008	228.7
3 2	39	3 2-1 0 0 0 0 1	1.8956725	9.678D-04	270.7	-.374684 +-.448620 -.505145 +-.449041	.628335	233.4
M3	41	3 3 0 0 0 0 0 2	2.8984104	5.000D-04	280.6	-.278024 +-.385065 -.257944 +-.385110	.379253	222.9
BSBP	43	<d/kas03_1_A_ml.ts>				.076319 +-.003480		
AIRP	44	<d/kas03_1_A_ap.ts>				-.624387 +-.012883		
/	45	Linear [m]/(8699*2.00000D+00[hl])				-6.903172 +-.224678		
/	45	Linear [m]/[year]				-4.516585 +-.147002		
-W	46	const 1.000D+00				.000402 +-.000132		

RESULTS: MAJOR TIDE AMPLITUDES, GREENWICH COPHASES

#pot.	dvlp	frequ.	core-factor SP_STRAT	amplitude [m]	cophase [deg]	+- 68.3% conf
Mm	040	.036292	1.0000 .00	.010980	93.1	+- .014747
Mf	076	.073202	1.0000 .00	.006110	224.9	+- .007051
Mt	114	.109494	1.0000 .00	.003521	211.9	+- .004422
Sig1	203	.861809	1.0037 -.03	.000779	234.4	+- .000464
Q1	225	.893244	1.0024 -.02	.006044	208.8	+- .000787
O1	257	.929536	.9996 -.01	.032435	208.8	+- .000637
M1	293	.966446	.9915 .02	.003501	200.6	+- .001394
P1	310	.997262	.9259 .40	.015707	207.6	+- .000543
K1	324	1.002738	.7339 3.03	.037384	207.2	+- .000555
J1	351	1.039030	1.0270 -.10	.003417	194.0	+- .000774
001	378	1.075940	1.0172 -.07	.001761	213.0	+- .000440
3N2	432	1.828256	1.0000 .00	.000149	273.4	+- .000265
2N2	452	1.864547	1.0000 .00	.001082	195.8	+- .000232
N2	474	1.895982	1.0000 .00	.007177	201.7	+- .000481
M2	501	1.932274	1.0000 .00	.039114	201.5	+- .000302
L2	526	1.968565	1.0000 .00	.001200	233.1	+- .000483
S2	546	2.000000	1.0000 .00	.018285	198.4	+- .000273
K2	577	2.041767	1.0000 .00	.000067	186.7	+- .000247
3 1	290	.965137	1.0000 .00	.001650	245.3	+- .001741
3 2	470	1.895673	1.0000 .00	.000609	266.8	+- .000435
M3	629	2.898410	1.0000 .00	.000190	272.9	+- .000193

Figure 2-20. *Result sheet from the least-squares adjustment, for KAS03_1_A as an example. The upper half of the figure (”ADMITTANCE”) shows the frequency setup for the tidal analysis, the resulting tidal admittances (waves Mm to K2), i.e. the responses of observed water head with respect to tide potential elevation. For nontidal effect the results comprise also admittance of the ancillary time series”BSBP” (Baltic Sea bottom pressure = sum of air pressure and water level elevation pressure),”AIRP” (air pressure),” / ” (a uniform ramp) and ”–W” (a constant bias). The lower half shows the tidal results converted into units of meter waterhead. The columns ”core-factor” show equivalent amplitude and phase change of the tide potential due to the earth’s liquid core as sensed in the borehole assuming the Bower fracture tide model. Confidence level is 68% and is specified always for amplitude; phase confidence is related to amplitude confidence by* $\delta\Phi = 360^{\circ} \cdot \mathrm{asin}\,(\delta A/A)$

Each response coefficient is a complex number representing the amplitude ratio and phase angle between the borehole tide and the astronomical tide. Referring to equations (1.3) and (1.8) in SCH1,

$$Z_j = (\Pi_j / g\rho) : (H_j \exp[i(\chi_j + m(j)\lambda)] / g)$$

is a dimensionless tidal response coefficient (water had divided by potential height). The phase of Z_j expresses whether the pressure tide leads or lags the potential. Since the incidence of high potential coincides with high surface elevation and thus with positive dilation of the crust, pressure is low at this moment. Thus, in the Gaussian plane Z_j will be somewhere near the negative real axis. We will use body tide parameters only, i.e. the effect of ocean loading tides has been subtracted using the best-fitting set of strain coupling parameters.

Appendix A collects the full set of tide analysis results.

2.3.1 Strain coupling coefficients

At the next stage the observations are interpreted in terms of strain coupling coefficients (SSC), see SCH1 equation (1-14). Global strain includes solid earth tide and ocean loading. Typically 11 tidal wave-groups, i.e. 22 independent data values, determine three SSC's (10 wave-groups in the cases when K1 and P1 had to be combined due to short data segments). A pressure relaxation model helps to centre both fundamental bands in the Gaussian plane, so that the SSC's need only to take care about the change of amplitude and phase. The relaxation model is an all-pass model and has two parameters, one for the knee-frequency and one for the lower passband gain. The upper passband gain is fixed at unity. Thus, the system is well over-determined. The model is adjusted using the Marquart-Levenberg method (nonlinear least-squares).

An example is shown in Fig. 2-21 for KAS03_1_A. Shown are the observed Z_j's for the largest tides, three semidiurnal and four diurnal waves. They are plotted as simple coloured crosses surrounded by open squares that illustrate the standard deviation. On the model's side, the coupled strain of the solid earth tide is depicted as a Maltese cross. The ocean loading effect (again in the form of coupled strains) is depicted as small needles with heads in the associated colour; the effect is added to the solid earth tide.

For a nondispersive earth we would have one diurnal and one semidiurnal solid earth coefficient. We see, however, that the solid earth tide displays some dispersion in the diurnal band. This feature originates from the coupling coefficients for the strain due to the liquid core of the earth; at this stage they have not been re-iterated. From each legend entry there is one arrow pointing to the observation and one to the predicted body tide effect.

The misfit between the model and the observations gives the χ^2 of the fit, that will be examined together with the resulting strain coupling coefficients β_1, β_2, β_3. The latter are defined in SCH1 equation (1-14).

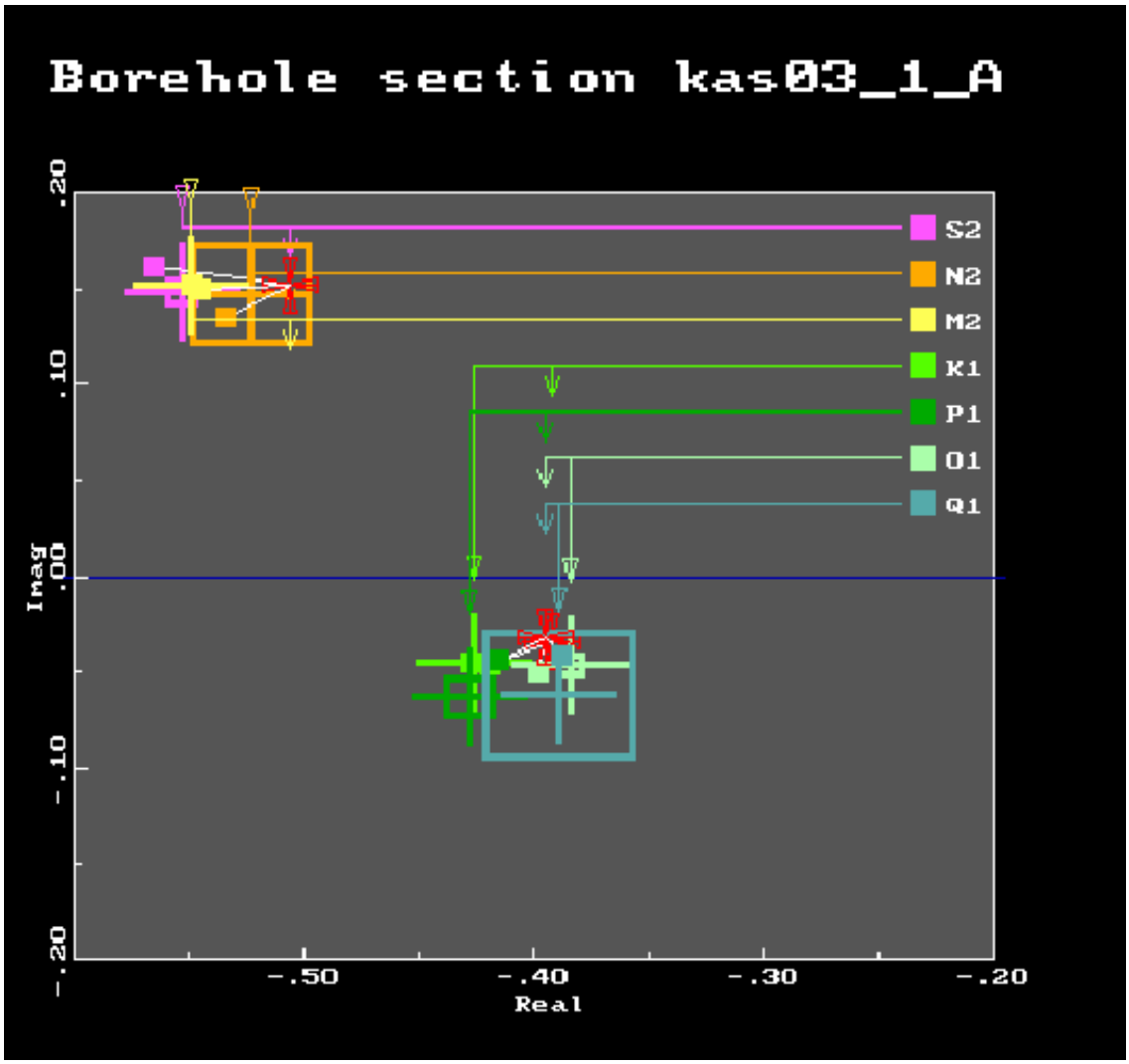

Figure 2-21. *Tide observations and model. Observations shown as central crosses inside open squares that indicate the 95% confidence limit. The model involves the response of the solid earth (Maltese crosses) to which the ocean loading phasors have been added. The Darwin symbols of the partial tides that have been analysed are shown in the legend. Lines and arrows connect the legend entries with both the associated body tide and the observed coefficient. The example is for KAS03_1_A, which has the highest tidal efficiency of all investigated segments. Ocean loading is seen to imply 2 to 5% perturbation in the diurnal and semidiurnal frequency band, respectively, and it does improve the fit. The residual dispersion due to the liquid core of the earth shows up at a perturbation level of less than 1%. The tidal response model at this stage consists of the three strain-pressure-coupling coefficients and a one-pole all-pass filter for borehole pressure delay/dissipation. The dichotomy into a diurnal and semidiurnal response is obviously reproduced with high confidence.*

2.3.2 Relaxation model

In order to account for a possible relaxation of tidal pressure in the borehole, a filter was introduced in SCH1 (equation 1-29). The filter is characterized by modelling a direct 1:1 response to tides at high frequencies, a relaxed response at low frequencies (attenuation factor r), and a transition time t_r where the response is half in between the two extremes. Since a wide frequency response spectrum is needed to resolve the relaxation time and relaxed response simultaneously, there is little hope to arrive at stable and precise solutions when long-period tides are not well resolved. This is a general problem as the fortnightly tide is generally small and hard to resolve. This was not possible in the prestudy, and in the present study no other borehole record did outperform the KAS03 series in this respect.

The relaxation model has mainly one purpose. It helps to align the tide phase. The strain coupling coefficients (three in number) leave one degree of freedom unused even in the case when we would have only one diurnal and one semidiurnal tide observation (four independent observables). The aim is to create overdetermination from additional tides observed in each fundamental band. Thus, this major degree of freedom needs to be exploited, prefarably with a model parameter that has a rather universal meaning. Phase alignment, however, cannot be forced without side effects on the amplitude, since causality must be obeyed. The allpass model accomplishes this, but it needs two parameters. A one-parameter model would make extreme assumptions at the low-frequency end of the response. A two-parameter model where one parameter is kept fixed at a harmless value seems more viable than enforcing a fixed zero or unity response at zero frequency.

Simultaneous solutions of r and t_r were attempted in a few cases. However, even in the case of the record with the highest tidal efficiency, KAS03_1_A, the confidence limits are greater or on the order of the parameters. It appears more sensible on formal grounds (but not on physical grounds) to fix the weakest one, transition time (t_r) at a short-time value (5 hours) and solve for the relaxed response (r).

In Table 2-4 the relaxation model results are shown. Relaxed responses less than unity are most readily explained by dissipation of pressure from the main fracture or borehole into connected structures at other orientation while friction impedes the flow. The other structure could actually include the atmosphere (the true relaxed response would be zero then, but such a conclusion cannot be based on diurnal and semidiurnal observations alone; one would need to study frequencies where the ensuing attenuation is effective). Relaxed responses greater than unity can be explained by fractures that are connected to the borehole via a friction-flow system, and the other fractures have greater tidal efficiency than the volume directly sensed by the borehole.

Table 2-4 suggests that the relaxed response is rather well determined unless the relaxation time is simultaneously solved. Many of the uncertainties are in the five to ten percent range. We note a few extreme results. They can only be discussed after the tide response ratio (M2:O1) is studied, so I defer this discussion to section 2.4.1.

Table 2-4. Relaxation model. In some cases simultaneous solutions have been attempted. Where zero uncertainty is given, the corresponding parameter has been kept fixed. Anomalies are discussed in the text.

Segment	Relaxation time t_r [h]	Uncertainty $\sigma(t_r)$ [h]	Relaxed response (r)	Uncertainty $\sigma(r)$
KI0023B_1_A	3,9	1,0	3,41	0,37
KI0023B_2_A	34	620	0,9	2,4
KI0023B_8_A	5,111	0	0,823	0,045
KI0023B_9_A	5,111	0	0,519	0,053
KI0025F02_2_A	5,111	0	1,052	0,036
KI0025F02_9_A	5,111	0	0,831	0,041
KI0025F03_9_A	5,111	0	0,781	0,063
KA1061A_1_A	5,111	0	0,411	0,034
KA1131B_1_A	5,111	0	0,328	0,035
KA1755A_2_A	5,111	0	0,413	0,031
KA1755A_2_B	5,111	0	0,564	0,036
KA2511A_2_A	5,111	0	0,815	0,034
KA2511A_4_A	5,111	0	0,836	0,037
KA2511A_5_A	5,111	0	0,837	0,033
KA2511A_6_A	5,111	0	0,859	0,034
KA2563A_1_A	5,111	0	0,912	0,033
KA2563A_2_A	5,111	0	0,974	0,028
KA3110A_1_A	5,111	0	0,79	0,11
KA3600F_2_A	5,111	0	0,888	0,045
KAS02_3_A	5,111	0	0,679	0,029
KAS03_1_A	10,9	24	0,76	0,42
KAS03_1_B	4,9	4,1	0,780	0,070
KAS03_1_C	4,4	8,7	0,850	0,085
KAS04_1_A	1,4	109	1,01	0,54
KAS04_2_A	5,111	0	0,656	0,023
KAS04_3_A	3,9	3,3	1,573	0,093
KAS04_5_A	5,111	0	0,552	0,015
KAS05_2_A	5,111	0	1,193	0,084
KAS06_6_A	5,111	0	0,890	0,046
KAS07_1_A	5,111	0	0,691	0,076
KAS07_1_B	5,111	0	0,597	0,057
KAS07_2_A	5,111	0	1,074	0,077
KAS08_1_A	4,3	1,8	2,532	0
KAS08_1_B	5,111	0	0,492	0,065
KAS09_1_A	1,0	5,1	1,042	0
KAS11_1_A	5,111	0	0,335	0,025
KAS11_4_A	5,111	0	0,641	0,088
KAS13_1_A	2,837	2,45	1,93	0,31
KAS16_2_A	5,111	0	1,15	0,027
KAS16_2_B	1,53	1,90	1,38	0
KAS16_3_A	5,111	0	0,457	0,032
KAS16_4_A	16.0	7,9	7,9	1,9
KBH02_3_A	5,111	0	1,68	0,12
KBH02_4_A	5,111	0	0,31	0,14
KBH02_5_A	5,111	0	0,65	0,13
KBH02_6_A	6,1	3,8	1,41	0,11

2.3.3 M2:O1 ratio

In order to gain a comprehensive overview over the situation comprising all borehole segments at once, a convenient route of attack is to compare the ratio of the tide response coefficients between the two lunar waves O1 and M2. These two tides are least effected by local weather and climate and they represent the strongest tidal effects in the diurnal and semidiurnal bands, respectively. Thus, they convey the essential information as to the coupling of the three horizontal strain components into the observed pressure variations. The diurnal wave O1 is almost unaffected by earth core effects. However, the ocean loading effect must be subtracted before the ratio is computed

$$[Z(\mathrm{M2}) - \hat{Z}_{\mathrm{OL}}(\mathrm{M2})] : [Z(\mathrm{O1}) - \hat{Z}_{\mathrm{OL}}(\mathrm{O1})] \tag{2-6}$$

where $\hat{Z}_{OL}$ is the product of SCH1 equations (1-14) and (1-19).

According to the Bower model of tides in a water-filled fracture the ratio

$$\hat{Z}_{\mathrm{SE}}(\mathrm{M2}) : \hat{Z}_{\mathrm{SE}}(\mathrm{O1}) \tag{2-7}$$

(where subscript SE designates the solid earth tide) has a unique relation with the orientation of the fracture (however, the ratio is insensitive to the elastic properties of the rock). The relation was shown in SCH1 as Fig. 1.8. We now need the inverse of this figure, i.e. the inverse of the relations (1.20)-(1.27) of SCH1, in order to show the response ratios side by side for all data segments. Each ratio, if sufficiently certain, will point out a unique dip and strike angle. In order to construct the plot the Bower model is run through the permissible range of dip and strike parameters; the resulting modelled ratio is depicted on behalf of its amplitude and phase.

The trivial model of uniform coupling of dilatational strain and nonadmittance of shear strain would result in a value of unity (within three decimal places; in the fourth decimal place consequences of earth flattening and core would show up). This plot is a control station for eventual further analysis.

2.4 Tidal results and discussion

The strain coupling coefficients β_1, β_2, β_3 and the normalised χ^2 of the solution are tabelled in Table 2-5. For the SCC formulation, equation (1-14) of SCH1 has been employed,

$$\tilde{\Pi}_j = \frac{i\omega + r/t_r}{i\omega + 1/t_r}\left[\beta_1(\tilde{\mathrm{E}}_{ee,j} + \tilde{\mathrm{E}}_{nn,j}) + \beta_2(\tilde{\mathrm{E}}_{ee,j} - \tilde{\mathrm{E}}_{nn,j}) + \beta_3\,\tilde{\mathrm{E}}_{ne,j}\right] \tag{2-8}$$

where the borehole tide pressure is given in units of water head. The observation equation contains the relaxation model (1-29) of SCH1. The parameters of the relaxation model are given in Table 2-4. The relation of water head to tidal strain is dependent primarily on the following earth parameters: Love numbers h_2=0.6030, l_2=0.0841, employing the Wahr (1981) solid earth tide model and the Tamura (1987) tide potential.

From the χ^2 of the SCC determination (Table 2-5) the quality of the records can be characterised. The four estimated parameters reduce the signal efficiently, normalised χ^2/n dropping from typically 25 to near unity. Some cases of good and exceptionally bad fit will be discussed below. In all except 5 cases the normalised χ^2 is below 2 (between 8 and 2 in descending order: KAS04_1_A: 8.2, KI0023B_8_A: 7.0, KAS09_1_A: 3.1, KAS16_4_A: 2.5, KAS04_3_A: 2.2).

The M2:O1 ratios of all examined segments are shown in Figure 2-22 and tabelled in Table 2-6. A nonzero phase change between the semidiurnal and diurnal wave-groups is an indicator for shear strain coupling. Values between -8 and 0 degrees are possible to explain by a first order pressure dissipation model. We see from Figure 2-23 that this is the case only in a few segments. Thus, most segments show significant shear strain coupling. A clear dependence on depth is not seen.

The tide efficiencies and tide SNR's that are found suggest that the 5 cm discreteisation of water head in some of the tunnel boreholes is not a limiting factor for the results.

Inspection of Table 2-6 and Figure 2-22 suggests that results with uncertainties greater than 0.2 are not worth further analysis. The first 16 segments would provide enough certainty so that different dip angles could be discerned. In the rest, the whole range steeper than 45° is bracketed by the error bar.

A few M2:O1 ratios have a large phase part while amplitudes are near unity; thus the nearest fracture zone solution would imply extremely low dip angle faults. Angles below 30 degrees might be termed exteremely low because of the increasing pressure that is required to keep them open and fluid-filled to an apreciable degree. However, most of these cases are determined with large confidence intervals. The three most significant cases pertain to segments KAS16_2_A, KI0023B_1_A and KBH02_3_A.

Interesting cases for further inspection are KAS08_1_B and KI0025F02_2_A; their M2:O1 ratios are far inside the Bower curves while the determination did succeed with low uncertainty.

M2:O1 ratios that fall inside the curve of 90 dip are not possible to explain with the Bower model unless additional complication is introduced. The following attempts are possible from a principal point of view:

1) interacting fracture systems. The concept, if formulated in a model, would lead to more parameters than observables if borehole sections are analysed one at a time. Dedicated studies on fracture systems known to interact could be conceived.

2) pressure relaxation together with a fracture zone orientation of 70° to 90° azimuth. Most extreme, a first order high-pass model would represent the effect of a simple pressure leak. In this situation phase can change by as much as 20° between M2 and O1 and amplitude ratios, constrained by causality, by 1.6.This does not bring the bulk of the heap closer to the Bower curves. However, it could bring a couple of points inside the 90 dip curve closer to a unit response. A leaky confinement would show up in the barometric response. Whence the number of candidates is quickly diminished to KBH02_4_A and KBH02_5_A.

Generally the heap at 140° hints at a regional effect. It appears as if regional anisotropy introduces a regional structure. The preferred azimuth as found in Munier (1993) in his clusters 2 and 4. Munier (1993) concludes hydraulically active fractures at N-S, E-W, and ENE azimuths as well as on the steep fractures at SSE azimuth. In this framework we could conclude that the effective fractures are those with SSE azimuth, and that the other fractures modify the dominating effect to varying degree.

The only way to sort out this complex situation is to perform strain observations in the tunnels and in dry holes in undisturbed rock units.

High resolution and low noise conditions are vital for the tidal analysis. Only in a few cases the results look promising, mostly in the deepest sections. The effect of varying air pressure in the tidal frequency band is limited in amplitude. The reason for the very low barometric efficiency in the deep sections is still unclear. Thus, it appears pessimistic to expect improved parameter resolution from air pressure analysis, unless more refined methods than the cross-spectral analysis of this report can be developed.

2.4.1 Detailed discussion - Anomalous relaxation results

First of all, **KAS16_4_A** has very little tidal efficiency, therefore great uncertainties in the tide coefficients, so an extreme relaxed response (in this case a low value) is no surprise. Another interesting case is **KAS16_3_A**, which also has a low relaxed response, but for its comparatively shallow depth this segment has a very high tidal efficiency (2.7 cm M2 amplitude). The relaxation model implies a phase shift M2:O1 of -8° and amplitude ratio of 1.14. Ignoring the pressure relaxation model, the fracture zone parameter fit is affected (the effect can be read from Fig. 2-21 by shifting mark "o" 11 percent down and 8° right, which brings it right into the middle of the "big heap"). However the least-squares fit of the SCC's is significantly improved with the strong relaxation (the normalised χ^2 decreases from 4.7 to 0.7). **KA1061a_1_A** is an almost exact pendant to KAS16_3_A. The difference is the low tidal efficiency, and that the response ratio would arrive at almost unity if the pressure relaxation is ignored. Also in this case, however, the SCC least-squares fit gains substantially from including the relaxation parameter.

A second group has large low-frequency responses, i.e. greater than unity. These cases have all in common that the relaxation time has been subject to fit. I give here the results with fixed relaxation time (5.1 h).

KAS16_4_A. We can skip this case since the segment has practically no tide signal.

KAS04_3_A, r=1.57. This segment has very low tidal efficiency and a bad fit of SCC's. In simultaneous solution of t_r and r the normalised χ^2 does not improve below 3.

KAS08_1_A, r=2.50. The normalised χ^2 stays at 1.8 so that the simultaneous iteration of t_r and r resulting in a slightly shorter relaxation time (4 h) does not significantly improve the fit. I also give the gain factors from the tidal least-squares analysis:

O1 0.25 ±0.02, M2 0.17 ±0.01. This is very different from segment _B:

O1 0.24 ±0.04, M2 0.32 ±0.02.

Both segments have been termed unreliable before.

KI0023B_1_A, r=3.41. The normalised χ^2 is near unity for this case. Iteration of t_r yields only slightly shorter relaxation times (4.5 h), and the relaxed response never falls below 2.84. This segment shows one of the largest M2:O1 phase differences (M2 122°, O1 170°), and the O1 phase is not lagging. The tidal gain factors are here

O1 0.25 ±0.02, M2 0.38 ±0.01

The leading O1 phase requires a pressure relaxation model with a lowpass character. This has an unfortunate side effect. The model restores the fracture response such that the instantaneous tidal efficiencies drop by a factor of two. This is seen in the large difference between the tide admittance in the tidal least-squares fit (values above), and the SCC solution

O1 0.06, M2 0.12.

If a flat relaxation model is forced upon the solution, the χ^2 of the fit stays at very poor values (χ^2/n=12.5), so that a large relaxation towards low frequencies is required. Taken at face value, the M2:O1 ratio would point to a low dip angle fracture. However, the combination of two extreme situations may also be taken as a warning sign. As an alternative, a time lag of one hours due to a clock offset could in principle explain the behaviour. However, the other segments of this borehole do not show such large phase lags, and it seems unlikely that a clock offset would affect one section and not the others. A clock offset cannot be reconciled with the barometric phase spectrum either. In addition, there are indications from the barometric gain spectrum that there is an increase in gain towards long-periods. Thus, the conclusion is rather that this borehole section has an anomalous long-period response, perhaps due to delayed communication with another volume, fracture or borehole, and that the simple SCC model does not apply. Maybe the lower packer of section 1 was leaky.

Table 2-5. Strain coupling coefficients from the tidal analysis

Segment	β_1	$\sigma(\beta_1)$	β_2	$\sigma(\beta_2)$	β_3	$\sigma(\beta_3)$	χ^2/n
			[m/μ]				
KI0023B_1_A	-1,007	0,193	-0,4	0,078	-1,205	0,377	1,48
KI0023B_1_M							
KI0023B_2_A	-2,498	0,081	-0,285	0,046	-0,506	0,060	1,03
KI0023B_8_A	-2,392	0,065	-0,399	0,049	-0,335	0,089	7,03
KI0023B_9_A	-2,662	0,093	-0,495	0,082	-1,037	0,147	0,68
KI0025F02_2_A	-2,342	0,047	-0,350	0,035	-0,456	0,065	1,86
KI0025F02_9_A	-2,494	0,062	-0,338	0,048	-1,115	0,085	1,07
KI0025F03_9_A	-2,487	0,097	-0,448	0,075	-0,825	0,135	1,51
KA1061A_1_A	-1,694	0,039	0,031	0,031	-0,381	0,048	1,33
KA1131B_1_A	-1,834	0,045	0,036	0,036	-0,407	0,054	1,40
KA1755A_2_A	-2,462	0,052	-0,292	0,041	-1,004	0,067	1,45
KA1755A_2_B	-2,767	0,065	-0,404	0,051	-1,032	0,088	0,34
KA2511A_2_A	-2,530	0,053	-0,255	0,041	-0,994	0,070	0,78
KA2511A_4_A	-2,597	0,057	-0,333	0,045	-1,232	0,078	0,25
KA2511A_5_A	-2,591	0,052	-0,255	0,040	-1,203	0,069	0,34
KA2511A_6_A	-2,535	0,052	-0,283	0,041	-1,194	0,070	0,31
KA2563A_1_A	-2,566	0,049	-0,335	0,037	-0,516	0,067	0,35
KA2563A_2_A	-2,520	0,040	-0,308	0,030	-0,555	0,054	0,33
KA3110A_1_A	-1,570	0,106	-0,082	0,081	-0,834	0,129	0,57
KA3600F_2_A	-2,540	0,069	-0,308	0,054	-1,060	0,094	0,35
KAS02_3_A	-3,455	0,064	-0,199	0,053	-1,470	0,087	1,73
KAS03_1_A	-3,707	0,029	-0,567	0,023	-1,964	0,040	0,84
KAS03_1_B	-3,641	0,220	-0,712	0,068	-1,931	0,248	1,36
KAS03_1_C	-3,850	0,437	-0,618	0,124	-1,697	0,489	0,49
KAS04_1_A	-1,602	1,054	-0,165	0,193	-0,805	0,917	8,21
KAS04_2_A	-2,650	0,039	-0,187	0,032	-1,375	0,053	1,65
KAS04_3_A	-0,978	0,198	-0,003	0,037	-0,450	0,211	2,20
KAS04_5_A	-2,737	0,028	-0,091	0,023	-1,294	0,037	1,49
KAS05_2_A	-2,434	0,111	-0,075	0,085	-1,127	0,147	1,73
KAS06_6_A	-0,948	0,026	0,004	0,020	-0,342	0,033	0,68
KAS07_1_A	-3,149	0,157	0,274	0,141	-1,348	0,233	1,04
KAS07_1_B	-2,672	0,099	0,104	0,087	-1,199	0,144	1,32
KAS07_2_A	-1,041	0,051	0,045	0,044	-0,855	0,071	0,97
KAS08_1_A	-0,999	0,155	0,064	0,041	-0,692	0,205	1,66
KAS08_1_B	-2,635	0,113	0,027	0,093	-1,353	0,144	1,15
KAS08_1_C							
KAS09_1_A	-1,560	0,084	-0,113	0,078	-0,421	0,115	3,11
KAS11_1_A	-1,622	0,028	-0,026	0,023	-0,353	0,036	0,48
KAS11_4_A	-1,450	0,084	0,063	0,065	-0,398	0,100	0,36
KAS13_1_A	-0,944	0,277	-0,435	0,173	-1,289	0,639	1,82
KAS16_2_A	-2,264	0,033	-0,158	0,026	-2,057	0,043	1,67
KAS16_2_B	0,004	0,001	-0,002	0,001	-0,003	0,002	1,14
KAS16_3_A	-2,660	0,058	-0,432	0,046	-1,485	0,077	0,52
KAS16_4_A	-0,294	0,064	0,183	0,049	-0,134	0,036	2,48
KAS16_4_Z							
KBH02_3_A	-0,899	0,049	0,044	0,038	-0,873	0,063	0,33
KBH02_4_A	-1,381	0,136	-0,042	0,108	-0,754	0,160	0,65
KBH02_5_A	-1,161	0,127	-0,268	0,099	-0,335	0,161	1,10
KBH02_6_A	-0,873	0,079	0,075	0,054	-0,888	0,095	0,81

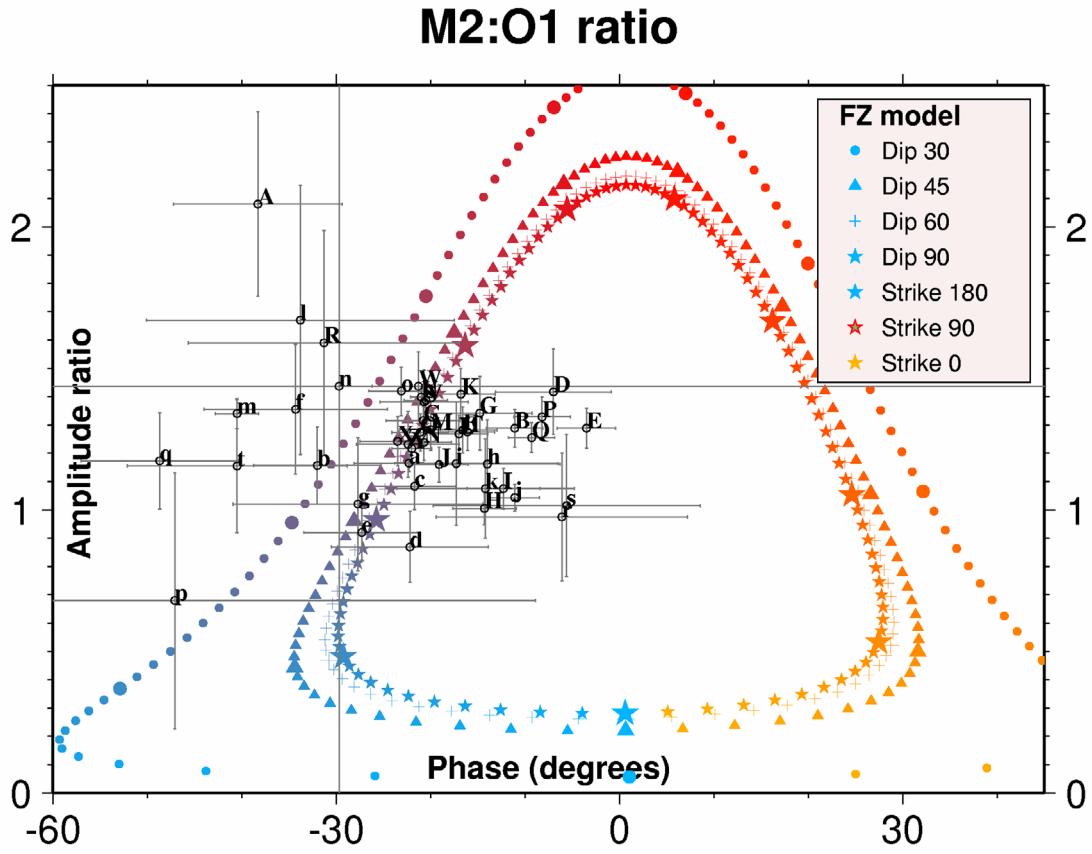

A	KI0023B_1_A	**B**	KI0023B_2_A	**C**	KI0023B_8_A
D	KI0023B_9_A	**E**	KI0025F02_2_A	**F**	KI0025F02_9_A
G	KI0025F03_9_A	**H**	ka1061a_1_A	**I**	ka1131b_1_A
J	ka1755a_2_A	**K**	ka1755a_2_B	**L**	ka2511a_2_A
M	ka2511a_4_A	**N**	ka2511a_5_A	**O**	ka2511a_6_A
P	ka2563a_1_A	**Q**	ka2563a_2_A	**R**	ka3110a_1_A
S	ka3600F_2_A	**T**	kas02_3_A	**U**	kas03_1_A
V	kas03_1_B	**W**	kas03_1_C	**X**	kas04_1_A
Y	kas04_2_A	**Z**	kas04_3_A	**a**	kas04_5_A
b	kas05_2_A	**c**	kas06_6_A	**d**	kas07_1_A
e	kas07_1_B	**f**	kas07_2_A	**g**	kas08_1_A
h	kas08_1_B	**i**	kas09_1_A	**j**	kas11_1_A
k	kas11_4_A	**l**	kas13_1_A	**m**	kas16_2_A
n	kas16_2_B	**o**	kas16_3_A	**p**	kas16_4_A
q	kbh02_3_A	**r**	kbh02_4_A	**s**	kbh02_5_A
t	kbh02_6_A				

Figure 2-22. *Complex plane for the tidal response ratio M2:O1. Given a perfectly isotropic and confined ground water response the expected value would be unity (except for a small deviation due to global effects like mantle rheology and earth flattening). Observations are shown denoted by letters and accompanied by 95% confidence intervals. Introduction of a fracture according to the Bower model causes systematically different values. They depend on fracture orientation in the first place and are slightly varied by fracture size. The colour symbols in the figure show the expected M2:O1 ratios for a sequence of fractures with azimuth coded by colour and three different dips denoted by symbol shape. At a 20° interval of azimuth the symbols are enhanced. Thus we can read a preferred azimuth for the bulk of the results at 130° and a slight preference for the steepest dip. The resolving power for dip appears frustratingly low. See the text for further discussion.*

Table 2-6. M2:O1 response ratio sorted in the order of increasing uncertainty. The data of this table is plotted in Fig. 2-22. Phase uncertainty is 360 x asin (δA/A) The last column also indicates with an asterisk if the data segment is short (duration less than x hours), in which case the spectral discrimination of the two diurnal tides P1 and K1 was not attempted.

Data segment	Amplitude ratio (M2:O1)	Phase [º] (M2:O1)	Amplitude uncertainty (95% cfd)	symbol in Fig.2-22
KAS03_1_A	1.3978	-21.0	0.0283	**U**
KAS04_5_A	1.1649	-22.3	0.0306	**a**
KAS04_2_A	1.2164	-22.0	0.0450	**Y**
KAS11_1_A	1.0425	-11.1	0.0477	**j**
KA2563A_2_A	1.2553	-9.3	0.0534	**Q**
KAS16_2_A	1.3400	-40.5	0.0534	**m**
KAS03_1_B	1.3862	-20.5	0.0552	**V**
KA1061A_1_A	1.0053	-14.3	0.0587	**H**
KA1755A_2_A	1.1603	-19.1	0.0613	**J**
KA2511A_5_A	1.2381	-20.7	0.0627	**N**
KAS02_3_A	1.2747	-16.1	0.0648	**T**
KA2511A_6_A	1.2731	-21.1	0.0668	**O**
KI0023B_2_A	1.2882	-11.1	0.0671	**B**
KA2511A_2_A	1.2678	-17.0	0.0676	**L**
KA2563A_1_A	1.3290	-8.2	0.0693	**P**
KI0025F02_2_A	1.2878	-3.5	0.0699	**E**
KA1131B_1_A	1.0751	-12.3	0.0719	**I**
KA2511A_4_A	1.2837	-20.0	0.0729	**M**
KI0025F02_9_A	1.2814	-16.6	0.0811	**F**
KAS06_6_A	1.0837	-21.7	0.0824	**c**
KAS16_3_A	1.4194	-23.1	0.0856	**o**
KAS04_1_A	1.2416	-23.5	0.0870	**X**
KA1755A_2_B	1.4089	-16.8	0.0893	**K**
KI0023B_8_A	1.3147	-20.8	0.0908	**C**
KAS07_1_B	0.9208	-27.3	0.0987	**e ***
KA3600F_2_A	1.3817	-20.7	0.1122	**S ***
KAS04_3_A	1.2309	-22.4	0.1167	**Z**
KAS03_1_C	1.4368	-21.3	0.1223	**W**
KAS07_1_A	0.8690	-22.2	0.1257	**d ***
KI0025F03_9_A	1.3421	-14.8	0.1299	**G**
KAS05_2_A	1.1562	-32.0	0.1364	**b ***
KI0023B_9_A	1.4171	-7.0	0.1510	**D ***

KAS08_1_B	1.1617	-14.0	0.1560	**h ***
KBH02_3_A	1.1735	-48.7	0.1702	**q**
KAS11_4_A	1.0757	-14.2	0.1764	**k**
KAS09_1_A	1.1631	-17.3	0.2189	**i**
KBH02_4_A	0.9742	-6.1	0.2258	**r**
KAS07_2_A	1.3554	-34.3	0.2295	**f ***
KBH02_6_A	1.1552	-40.5	0.2349	**t ***
KAS08_1_A	1.0192	-27.7	0.2350	**g**
KBH02_5_A	1.0153	-5.6	0.2506	**s ***
KI0023B_1_A	2.0805	-38.3	0.3258	**A**
KA3110A_1_A	1.5893	-31.3	0.3981	**R**
KAS16_4_A	0.6795	-47.1	0.4528	**p**
KAS13_1_A	1.6708	-33.8	0.4760	**l ***
KAS16_2_B	1.4368	-29.7	3.3977	**n**

2.4.2 Detailed discussion – example segments

KAS04_1_A

We find large residuals due to P1 and N2 tides. The anomalous P1 response might be related to perturbations at the solar diurnal cycle. Table 2-1 indicates a low tidal SNR, There are no clues why particularly this segment should have such a problem. The section is at normal depth, has normal tidal efficiency, so that the only possible reason is an anomalously high noise level. More effort could be spend on a reanalysis.

KBH02_3_A

This case is characterised by low tidal efficiency with moderate noise level. The M2:O1 ratio has a large phase and thus would point towards a low dip angle, if the fracture zone model is accepted. The section, however, is shallow, and the efficiency not anomalously low. The large phase shift might be less certain than in the deeper cases that have more tide signal. However, it is an interesting test case which should be looked at with other methods to try and confirm or reject the low dip angle that could be inferred from this study.

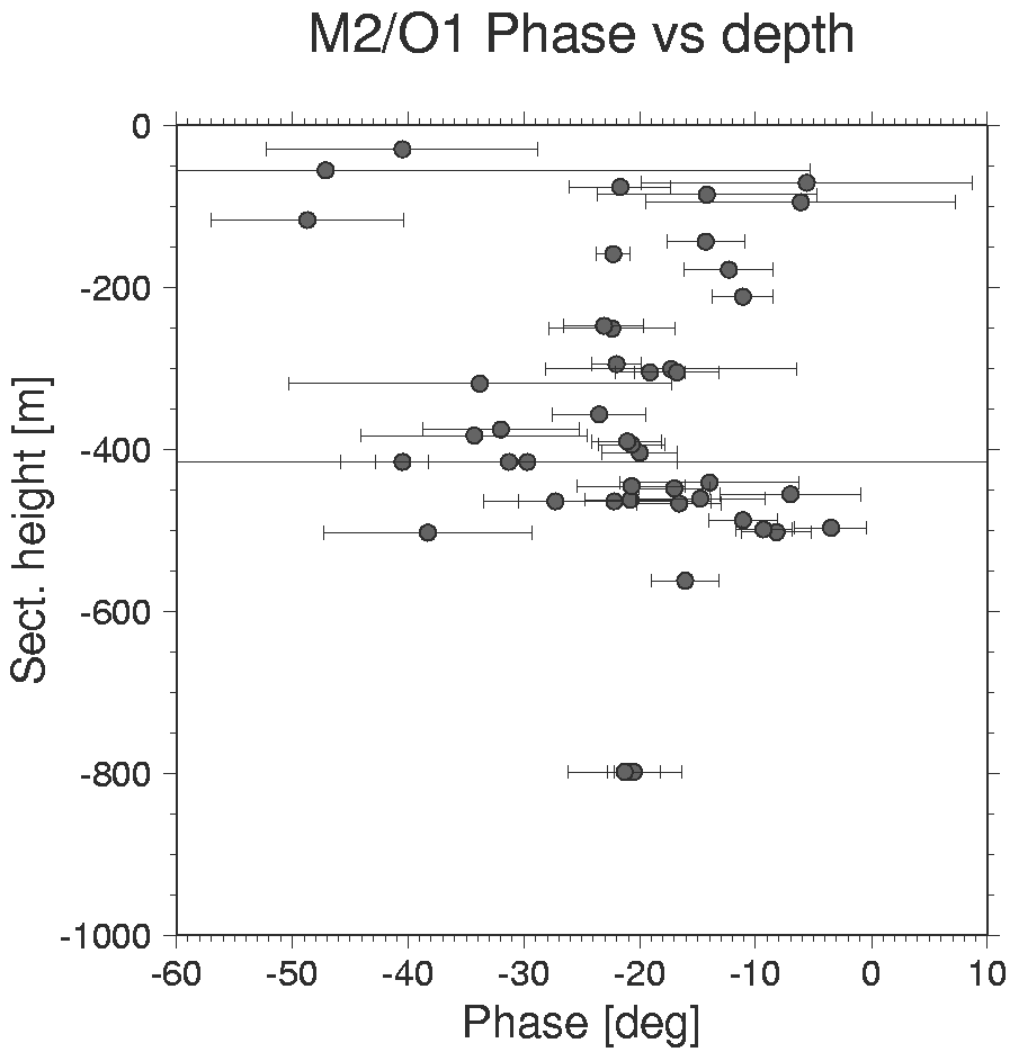

Figure 2-23. *The phase difference between semidiurnal and diurnal response is indicative of shear strain coupling. Values beyond 10 degrees are difficult to reconcile with a pressure dissipation process. In this figure it is demonstrated that there is no obvious relation between shear strain coupling and borehole section depth.*

KI0023B_1_A

General problems appear to exist with the model of this section. We have already noted to anomalously high relaxed response in the dissipation model (see Chapter 2.4.1 above). Applying the relaxation model the O1 response is reduced with respect to the M2 and an exceptionally large amplitude ratio M2:O1 results. Not applying the dissipation model results in a large misfit of the SCC model. Additional depth sections of the same borehole have been recorded and investigated (2, 8, 9). They do not show this behaviour (see Chapter 2.4.3 below).

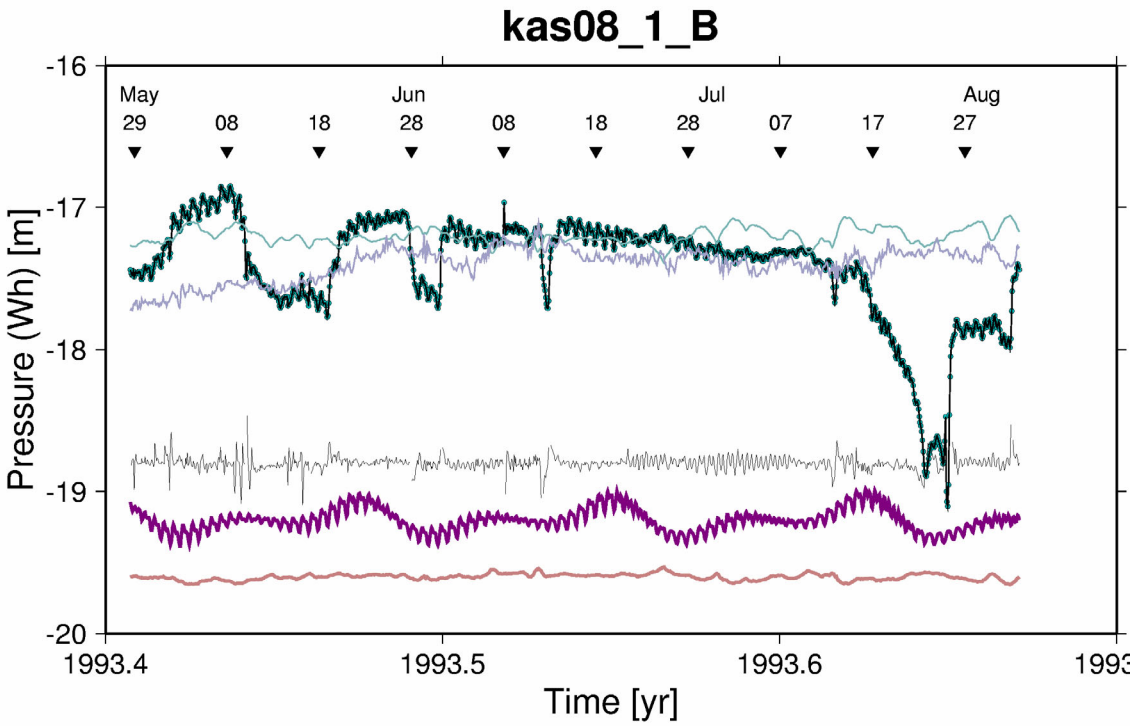

Figure 2-24. *Tidal decomposition for segment KAS08_1_B. The complete segment is shown- Curves as in Figure 2-5 with the addition of the least-squares residual (after difference filtering) shown in black. The residual has been made unitless by division with the RMS and been amplified with a factor 3 to improve readability. During a period between June 20 and July 10, tidal oscillations appear in the residual, pointing towards a change in confinement conditions.*

KAS08_1_A and B

This segment shows a mid-range tide efficiency. The segment B is short, so that P1-K1 discrimination cannot be accomplished. In comparison, KAS08_1_A was much longer, but the tide response is severely attenuated by almost a factor of 2 (see Table 2-2). The time series is an example for transient nonstationarity. A large change in tide efficiency occurs between 1992 and 1993 (between segments A and B). Segment A was discarded since it does not appear to be well coupled to the ambient stress, judging from the low tidal efficiency. Also within segment B the tide response is instable. The time series of segment B involved in the tide analysis are shown in Figure 2-24. A period of residual tide oscillations between June 20 and Jul 10, 1993, is clearly visible. Comparing the time series it appears as if the borehole section was not well-confined during this period, since tidal variations in the input data show reduced amplitude. There are no obvious relations to pumping tests or interruptions of the borehole record. On the other hand, the borehole response remains stable during quite large pressure changes on the order of one meter.

A power spectrum of the least-squares residual (Fig. 2-25) shows that the tidal spectral range below 2 cyc/d is practically white, a consequence of the difference filter. At higher frequencies spectral power falls off with ω^{-2}, i.e. this frequency range was proportional to ω^{-4} prior to the differencing operation. The power spectrum is estimated using a Hanning window of length 128 samples on the autocovariance sequence. Hence, the semidiurnal tidal transient feature is detectable in the power spectrum while the least-squares process cannot adjust to such a time-limited anomaly.

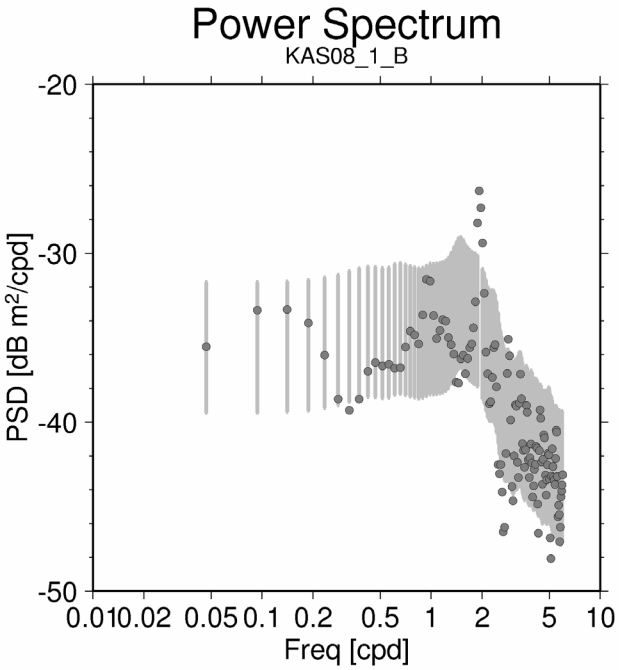

Figure 2-25. *Power spectrum of the least-squares residual (black curve in time series plot, Figure 2-24). The nonstationary feature in the tidal response between June 20 and July 10, 1993, is the cause of the peak at 2 cyc/d. The band of bars indicates the 95% confidence interval for noise. The flat level below 2 cyc/d confirms that the simple difference filter is sufficient to produce uncorrelated noise as required by the least-squares procedure.*

A look at the least-squares residual also convinces that those large, meter-scale transients do not introduce large features into the signal submitted the least-squares stages. The outlier editing process did successfully deselect the affected samples.

A second solution was computed, now deleting the dubious period (KAS08_1_C). The tidal coefficients changed with marginal significance (M2 from 0.0224 to 0.0218 ±0.0015 m in amplitude and by -3° ±4° in phase). The M2/O1-ratio (Fig. 2-22, Tab. 2-6) for this segment was found slightly off the centre of the crowd (due to a slightly smaller phase shift); deleting the period of low tidal response places the result a little closer to the crowd.

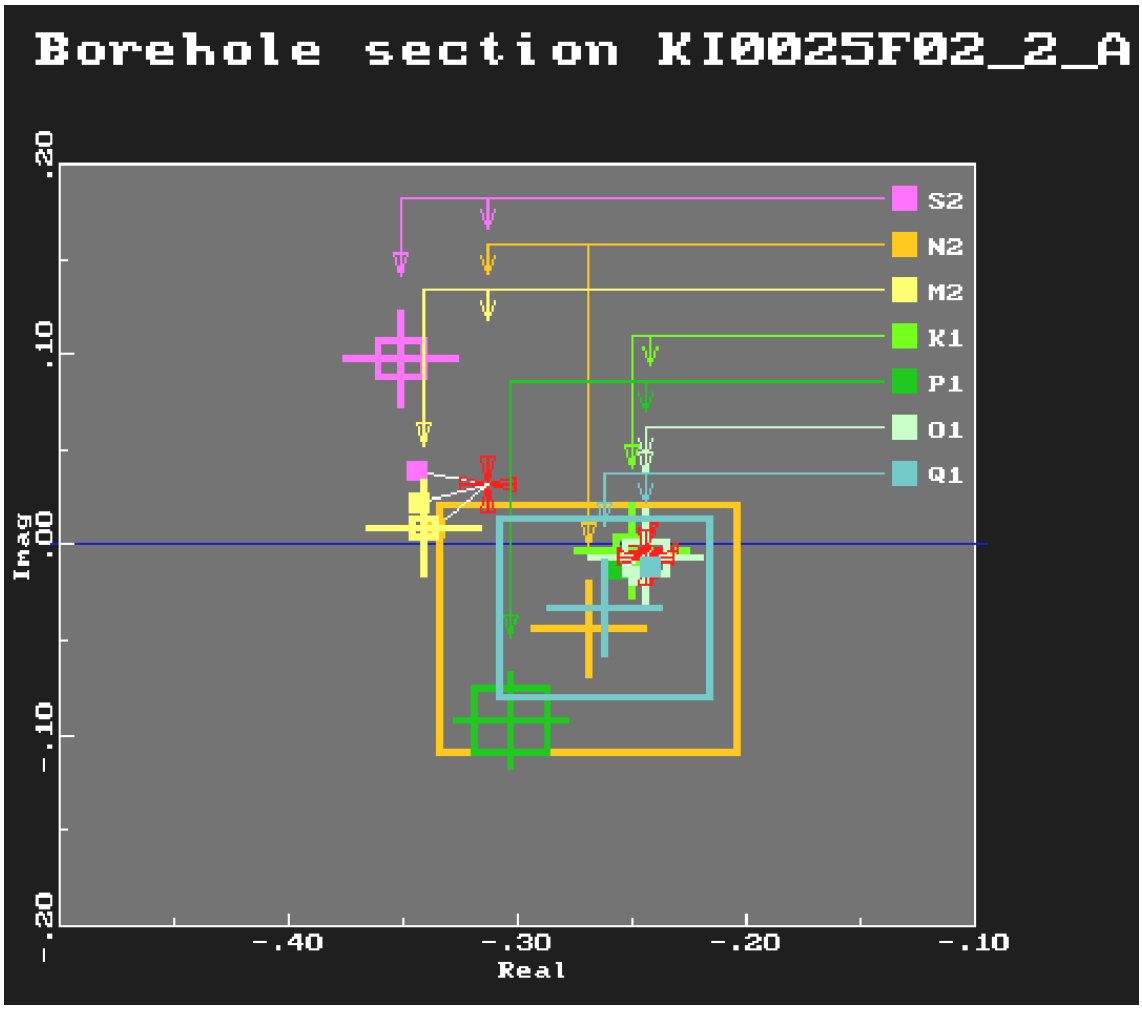

Figure 2-26. *KI0025F02_2_A may be disturbed at solar diurnal and semidiurnal cycles. The results for O1 and M2 alone indicate almost no phase shift. The amplitude ratio could be compatible with the observed low barometric gain at low frequency.*

KI0025F02_2_A

This segment appears to have chiefly a volumetric strain response. In this respect it is a rather unique case. O1 and M2 have almost identical near-zero phase (Figure 2-26). Especially noting the good signal to noise ratio (M2 T-SNR of 33 dB) the low influence of shear stress appears rather well-established. The other wave-groups, however, scatter quite much in this segment, despite the high tidal efficiency in this rather deep (495m) section. The SCC solution explains the amplitude ratio M2:O1 by means of North-north-east-east simple shear and determines the low frequency pressure relaxation at a value rather greater than unity. However, the amplitude ratio M2:O1 = 1.3 could also be explained by underestimated pressure dissipation. The cross-spectrum with barometric pressure shows low gain at low-frequencies and a substantial gain increase between diurnal and semidiurnal band (Figure 2-27). This back-pocket solution would be consistent with assuming large environmental perturbations at one and two cycles per solar day, which is not unusual. The major contradiction is seen in the failure of the SCC and relaxation model fit to cope with the sign of the M2-O1 phase. The relaxation model prefers a relaxed response greater than unity, which contradicts the barometric pressure finding.

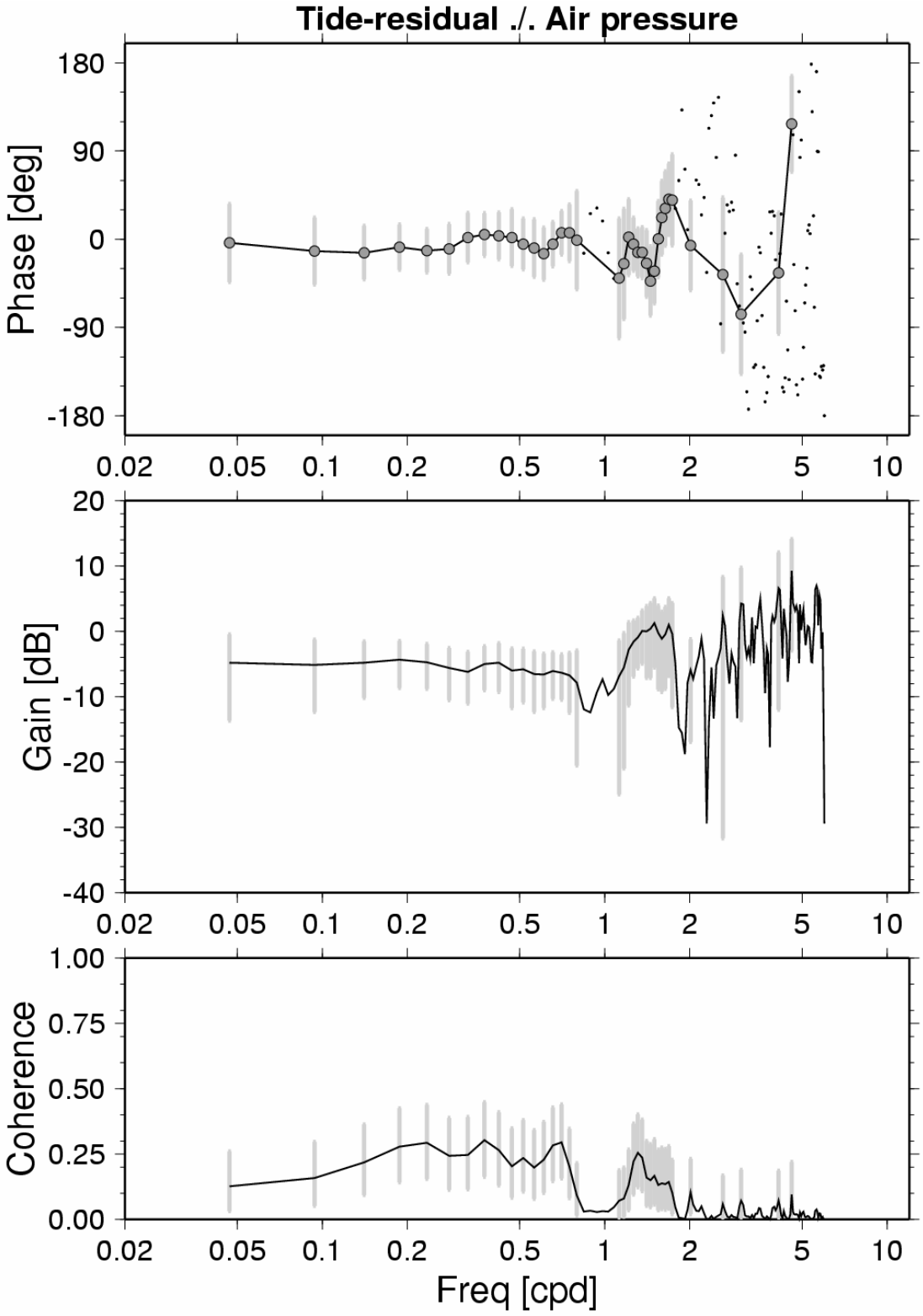

Figure 2-27. *Barometric pressure cross spectrum analysis for KI0025F02_2_A.*

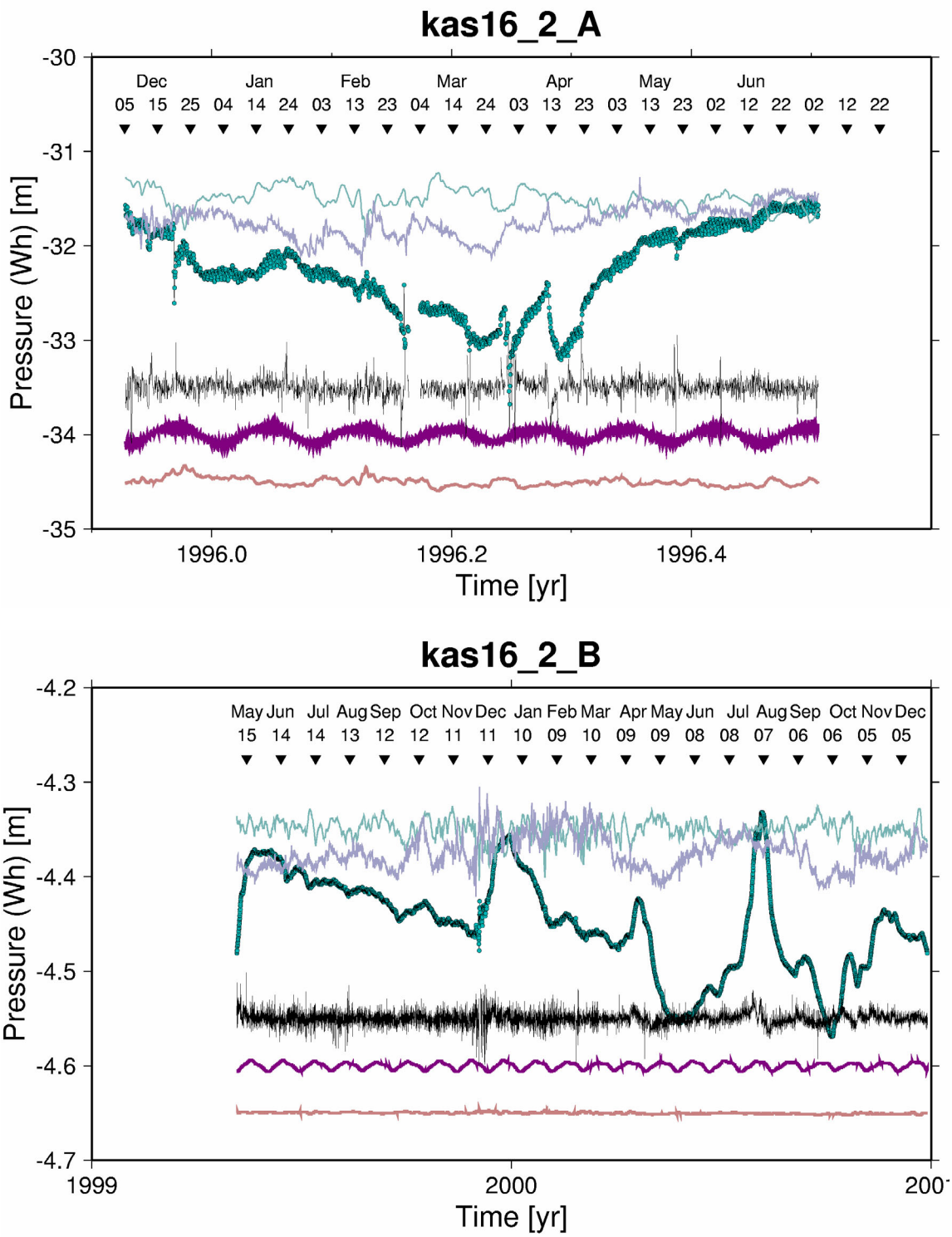

Figure 2-28. *Borehole behaviour in section KAS16_2 changed drastically between 1996 and 1999. Tidal components are clearly visible during 1996 (upper diagram, segment A), total signal variance is one order of magnitude greater (notice ordinate scale). In segment B the tidal response admits almost no daily tides but rather only a monthly component. In the lower diagram surface air pressure and sea level have been scaled by 0.1 and the filtered residual by 0.01. In the upper diagram the filtered residual has been scaled by 0.1.*

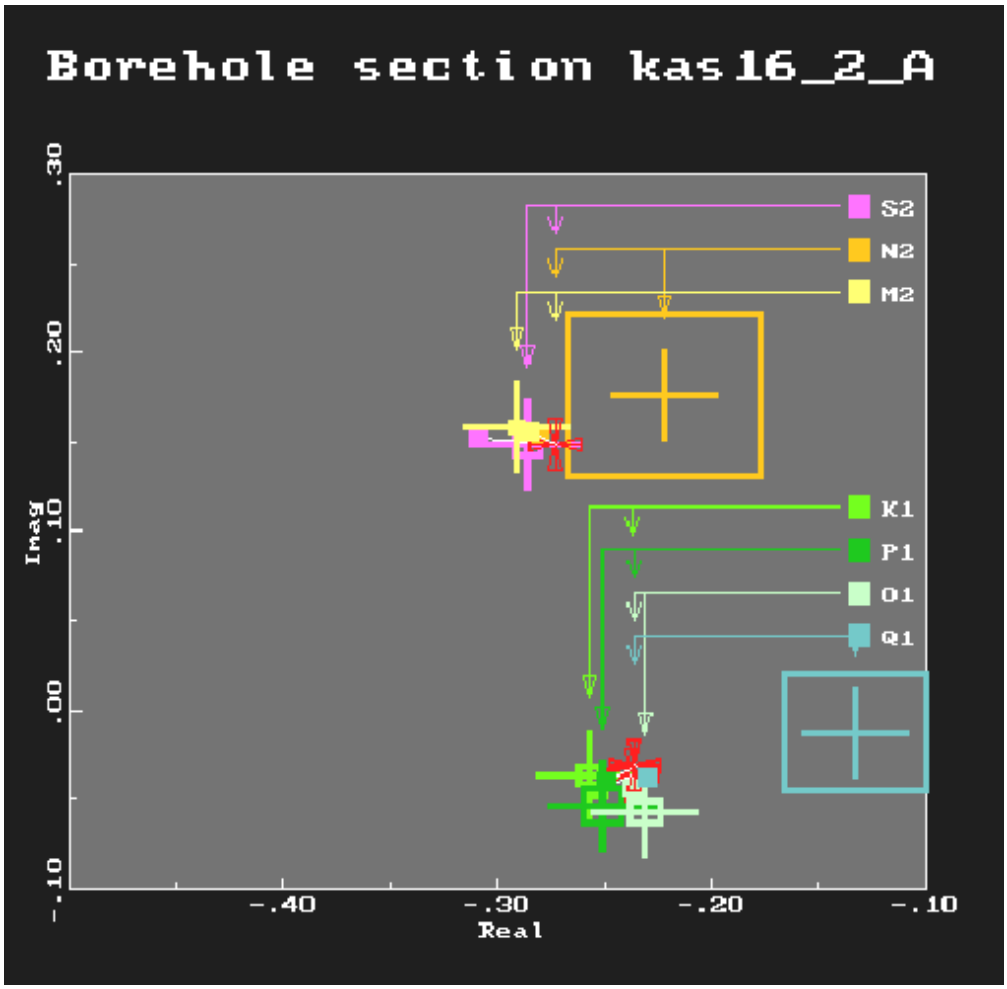

Figure 2-29. *KAS16_2_A tide modelling result. Very good fit is achieved with the greater tidal waves. Only the species that are closer to the noise floor (N2 and Q1) show noticeable disagreement. The normalised χ^2 for this case (from 11 tidal wave-groups) is 1.7. The plot suggests that the large phase shift between diurnal and semidiurnal species is highly significant.*

KAS16_2_A and B

The M2:O1 ratio for KAS16_2_A can be interpreted to point towards low dip (Figure 2-22, symbol m). We obtain rather narrow confidence limits for the ratio. The second segment from this section was found to have almost no tide signal (Figure 2-28). The strain coupling coefficients drop by three orders of magnitude (Table 2-5). The first segment, however, yields one of the largest and simultaneously most well-determined differences of semidiurnal versus diurnal response, M2:O1 = (1.34, -40°). Observe the small uncertainties in the tidal phasor plot (Figure 2-29) and the goodness of SCC-fit (χ^2/n = 1.67).

Examination of time series and tidal admittance suggests that a major failure in the confinement might have occurred between 1996 and 1999. More close inspection shows two points in time when the character changes, Oct. 9, 1997, tidal admittance appears to become lower, but short-period random signal persists. After Feb. 19, 1998 the signal loses almost all high-frequency content. During 1996 the data segment has rather high quality with not only easily determined tides but also a rather balanced surface air pressure response (Figure 2-30).

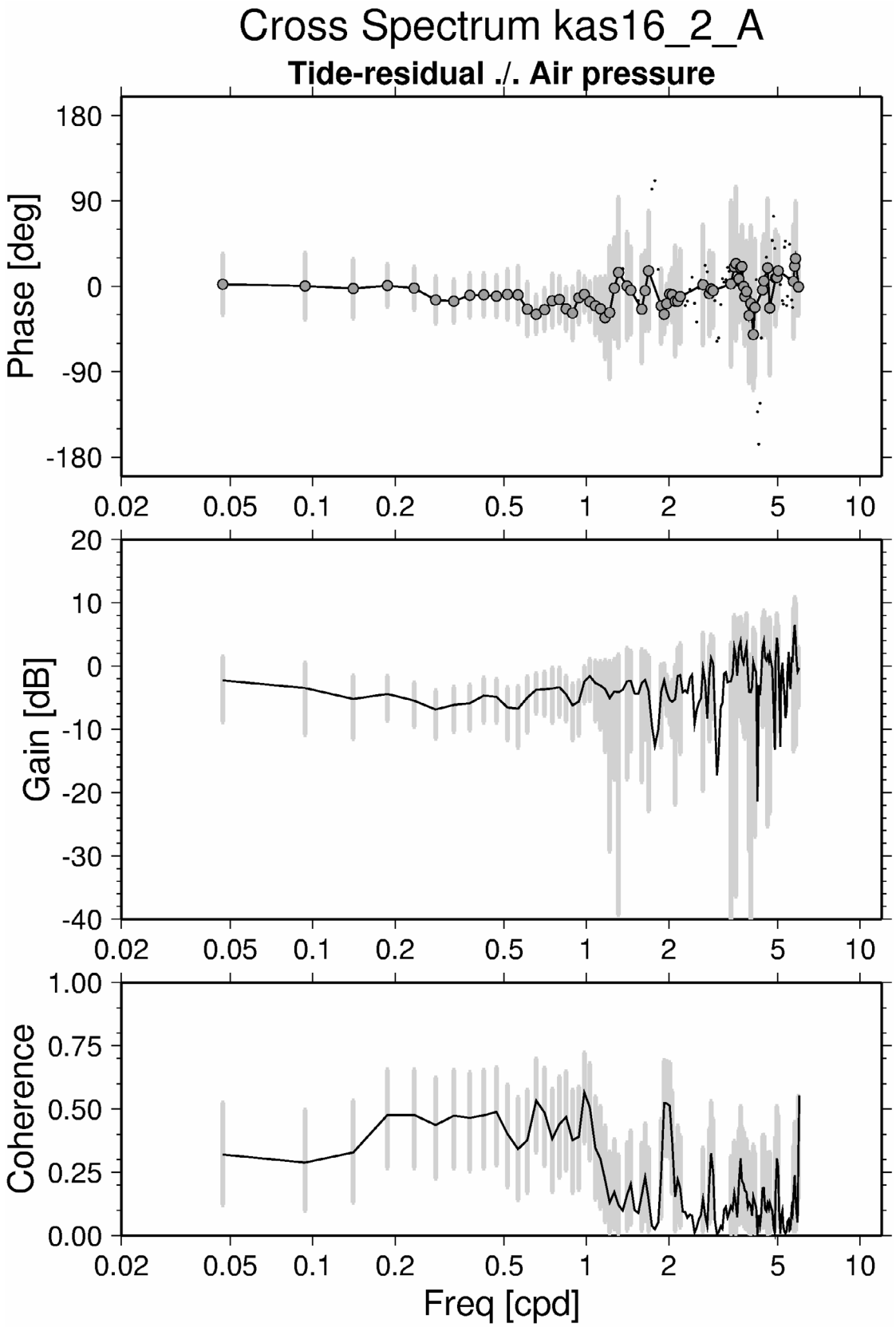

Figure 2-30. *Response spectrum of section KAS16_2 segment A to surface air pressure.*

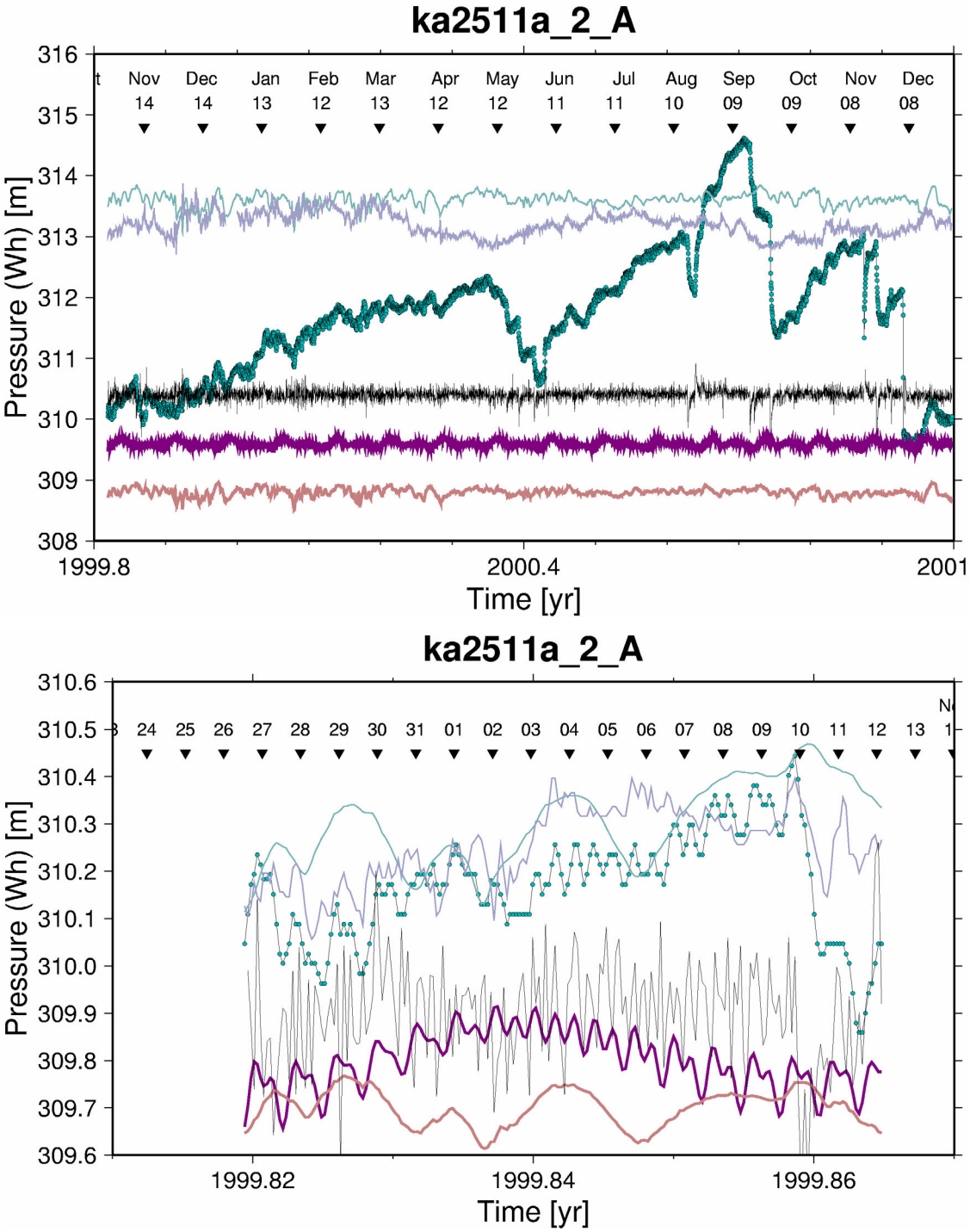

Figure 2-31. *ka2511a_2_a, lower diagram excerpt Oct-Nov 1999.*

KA2511a_2

This is an example for a tunnel hole with low-resolution absolute measurement (Figure 2-31). The semidiurnal waves show some scatter (Figure 2-32), still, the SCC fit succeeds with a small residual error (χ^2/n=0.78). The most serious closure residual appears at the solar semidiurnal tide S2. If it is externally generated (an environmental perturbation at half solar day period), the M2 result would be biased by -3% in the real part. However, such a perturbation goes usually hand-in-hand with a diurnal perturbation, to be expected as a large offset between the wave-groups K1 and O1. Such an offset is not observed in Figure 2-32.

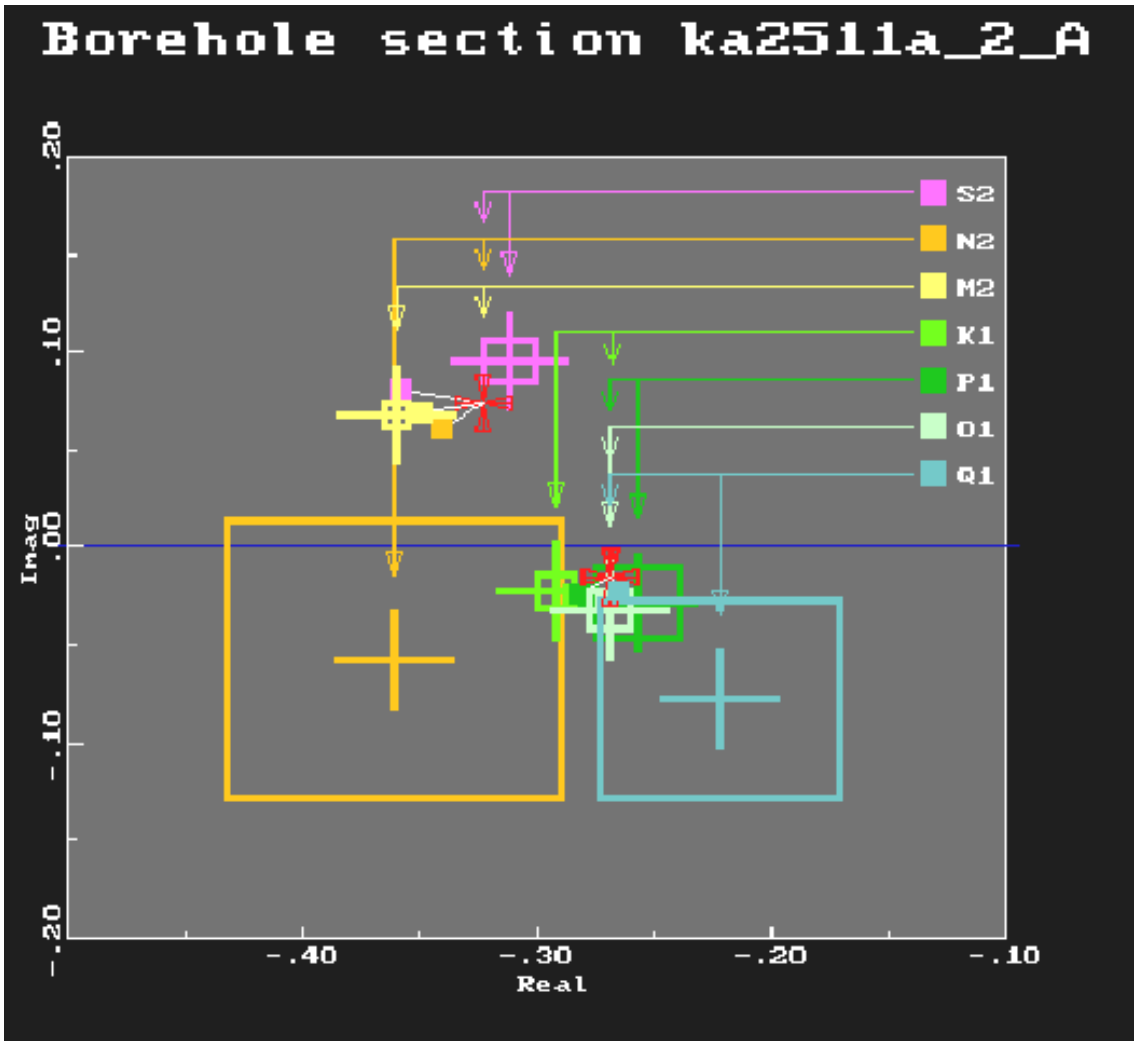

Figure 2-32. *Relatively large S2 residual. Example for a section with small phase difference diurnal vs. semidiurnal.*

The deep surface-drilled sections usually show considerably smaller S2 residuals (see Figure 2-21 for KAS03_1_A as an example).

The large discreteisation noise in this segment is probably the reason for the conservative *a posteriori* noise figure and hence the small χ^2. A more realistic standard deviation would be adjusted downward by 20% or even more, lending increased significance to the S2 residual.

The barometric response of KA1511a_2 is compatible with a flat gain spectrum (Figure 2-33). The coarse descreteisation causes the relatively wide confidence limits and the fading of the coherence beyond 0.5 cyc/d. The gain factor (ranging between 0.6 and 0.7) is somewhat too low to be explained with a fracture model, but the low confidence does not exclude such a model.

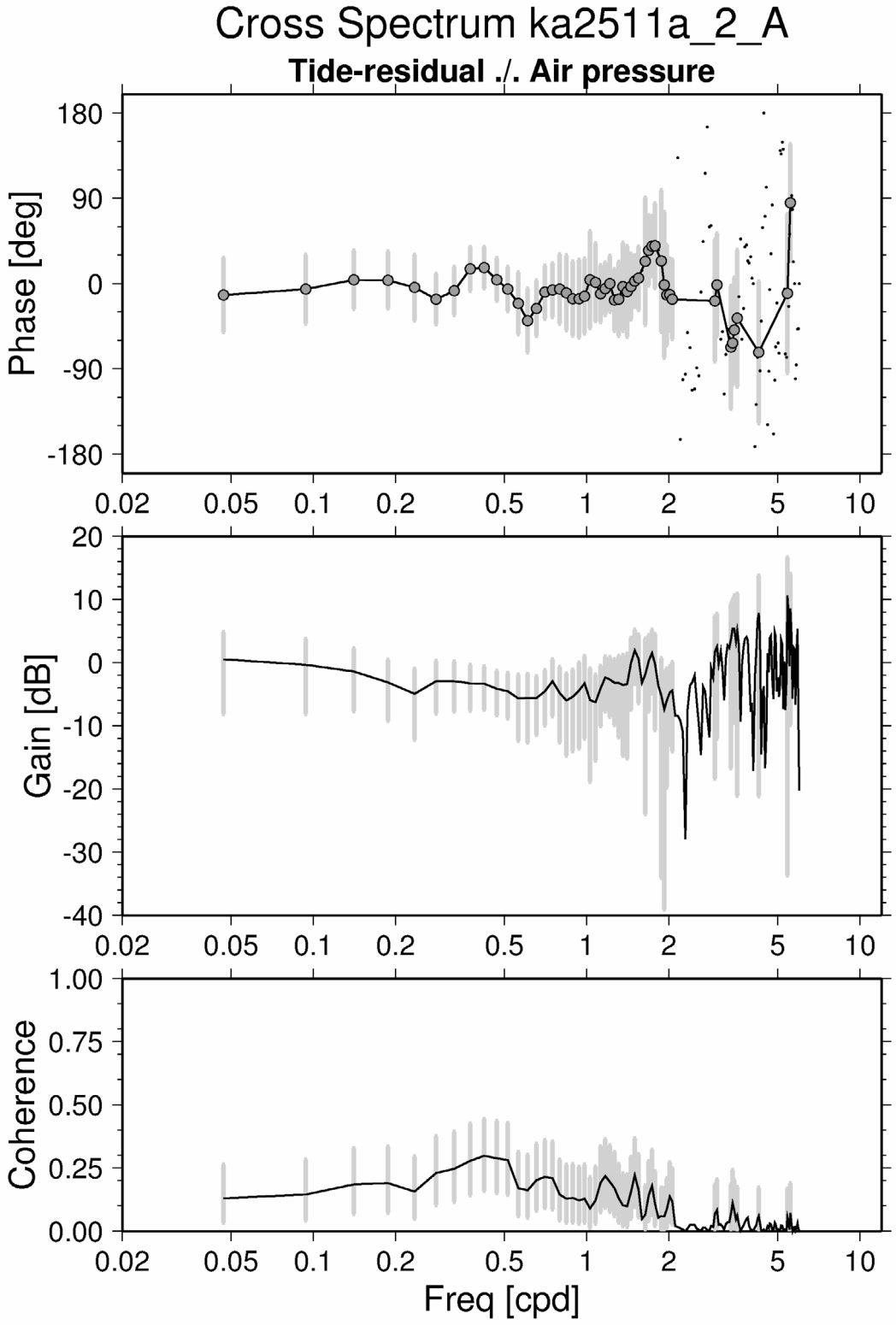

Figure 2-33. *ka2511a_2_a*

2.4.3 Separate sections in the same borehole

In four cases we have obtained reliable tide solutions for more than two sections in the same borehole. The results are worth a careful examination. The respective boreholes are KI0023B, KA2511a, KAS04 and KAS16 (Figure 2-34).

Well within the uncertainty both KA2511a and KAS04 show the same response in all sections. The M2 amplitudes in KA2511a stay almost constant between the sections while they change substantially in the sections of KAS04. There, the amplitudes do not simply increase with depth but increase in the order 3, 1, 5, 2 (no useful data could be retained from section 6). The respective depths are 250, 360, 160, and 300 m, while the depths of the KA2511a sections only range between 390 and 450 m. In KAS04, section 2 has a 2.5 times larger M2 amplitude than section 1. Still, the M2:O1 ratios almost coincide. Even more important appears to be the fact that both boreholes reproduce the same M2:O1 ratio within the error limit. And this ratio is near the centre of the heap of all M2:O1 results.

In comparison, the spreads in KI0023B and KAS16 are substantial and significant. The depth range of the KI0023B sections is only between 450 and 500 m. In KAS16 the segments are located at very different depths, 46, 215, and 415 m.

In KI0023B the lowest section (1) seems to be leaky; it appears to have the largest M2:O1 ration of the whole investigation, including a large phase offset and phase change. The next lowest section (2) has almost unity ratio M2:O1 with very little phase change. The third section from the bottom (3) has a response ratio falling on the steepest fracture zone model curve at a typical 130 degree azimuth. Finally the uppermost section (9, depth 450 m) has again a M2:O1 response ratio close to unity, impossible to reconcile with the fracture zone model. The data quality is generally good. Thus this set of sections can be treated as representative of the whole investigation. There are significant changes in the tidal response, they occur over short distances. However, there may be occasional problems with the recording (section 1). The general feature observed is a mixture of a single fracture zone response with a pure (shear-free) volumetric response, and the origin of the mixing is not accessible in this study.

As a result for the ensemble one could suggest that the centre of the heap represents locally undisturbed conditions. Tidal strain must then have been modified on a regional scale, e.g. due to oriented structures that affect the elastic properties of the crust. The nonzero phase difference between diurnal and semidiurnal tides hints at the north-east strain component being involved. The situation could be resolved by finding regional admittance factors individually for the north and east components of horizontal displacement before applying the operations in SCH1 equation (1-4). Alternatively, the Hooke equations (equation (1-25) in SCH1) must be modified to reflect some kind of anisotropy.

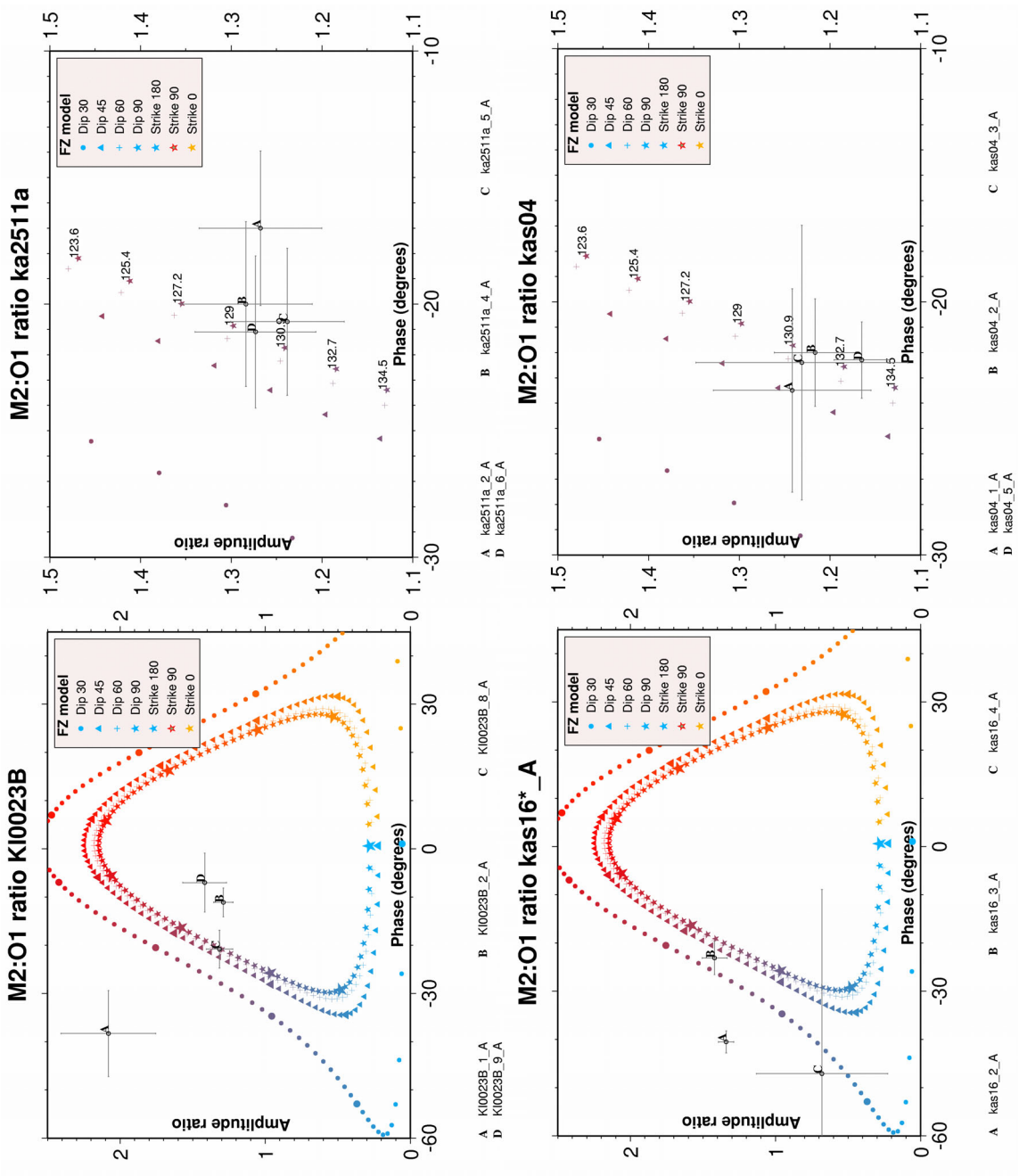

Figure 2-34. *Four boreholes with narrow spread (right column) and wide spread (left column), respectively, of M2:O1 ratios between different depth sections. Section legend below each frame. In order to facilitate the zoomed-in view of the narrow spread, the azimuth angles have been printed out.*

3 Conclusions

From the analysis of water pressure time series from 50 borehole sections we can conclude that in most of these tidal variations are present. The number of tide worthy record segments was 47, and they were taken from 41 different borehole sections.

Tide analysis succeeded in most cases with a normalised χ^2 of the fit near unity. This implies that the tide model seems to be accurate. The parameterisation includes first coefficients for a normal response, i.e. the coupling of volumetric strain computed for a uniform rock basement to borehole pressure. In addition two coefficients describe the coupling of ambient shear strain. Shear strain coupling appears to be highly significant for all except 6 to 8 sections. It may be indicative of oriented structures that respond to shear strain with a volume change, such as a fracture zone. The effect of shear strain coupling is exhibited by a non-unity ratio of the semidiurnal to diurnal response (so-called M2:O1 ratio). This is a complex-valued ratio; nonzero phase points towards North-east shear coupling, for which fractures of orientation at other azimuths than zero and 90 degrees are required. The three strain coupling coefficients still leave one degree of freedom unexplored. For this purpose a dissipation mechanism with one (two) free parameters is introduced to characterise the wide-band frequency spectrum response. It is constrained by causality.

The typical finding for the dissipation model is that a transition frequency parameter is uncritical, and the long-term response differs from the short-term response being typically lower by 25% to 30%. A few exceptions exist, some of them most probably related to a leaky confinement.

Shear strain coupling appears significant in almost all cases. A model by Bower (1983) was employed to try to explain the particular M2:O1 ratios found in the different record segments. The general observation is that the model's fracture azimuths are all between 120 and 140 degrees from north. There is a heap of results pointing towards high dip angles. However, the dip angle uncertainties are large, in more than half of the cases the uncertainty intervals encompass the interesting range between 30° and 90°.

From the investigation of M2:O1 ratios we may draw the conclusion that depth range does not appear to play an important role for the spread of the ratios. One may hypothesise that the majority of cases are centred on a ratio that is dictated by nonuniform tidal strain in the whole region, and that fractures or other section-specific features may contribute to offset the M2:O1 ratio further.

The heaping of the fracture zone model at mostly one azimuth suggests that the property formulated by the model is not a feature that pertains to specific borehole sections. The original plan of the project to infer single fracture orientations from borehole tides does not appear to be viable.

The Bower model does not appear able to resolve the situation in a satisfactory way. If the borehole response is to be resolved further, the ambient tidal strain in the rock mass needs to be measured, e.g. using strain gauges. At the Piñon Flat Observatory laser strain meters have been in operation for more than 20 years (http://www.igpp.ucsd.edu/aboutigpp/history/timeline2.html). Also, borehole strain meters are being used; instruments and projects have been presented in e.g. Onoue et al. (2001), Takemoto et al. (2003) or Hart et al. (1996).

On the theoretical side, development to extend the simple fracture zone model is required. Maybe the whole concept must be abandoned altogether. Maybe the modelling situation is just slightly more complicated in that the oriented fracture needs to be inserted into a directionally perturbed stress or strain regime. Anyway the remaining problem appears nontrivial.

The truly limiting circumstance to further studies appears to be the uncertain impact of surface air pressure on the pressure in the borehole sections. Ideally, the response would add an important third dimension to the problem, helping to resolve the dip angle of a fracture zone—or in more general phrasing—monitor the admittance of vertical strain into borehole pressure.

Can the tidal results be reached faster, i.e. using shorter time series? It seems that resolution of P1 and K1 is important as a control of environmental perturbations and for overdetermination of the tidal estimation process. However, a very short lunar-only version could be based on O1 and M2 parameters alone. If transient perturbations can be suppressed, one month duration (in order to separate lunar and solar effects) and on the order of 5000 samples (like 5 minutes sampling interval) would provide the necessary basis for a 20 dB signal-to-noise ratio as a minimum. However, 30 dB would be preferable. Since tide amplitudesrarely exceed a few centimetres, sub-millimeter sensor resolution is required for the greater SNR figure.

Finally an attempt of a short interpretation of the findings: The tidal solution could very well be determined by regional nonisotropic strain conditions in the bedrock as a consequence of prevailing, oriented fractures, joints and other structural features that reduce rigidity in a certain direction. The response of each borehole section would become almost identical because they would respond all to the same bedrock strain, assuming that eventual fractures have only small volumes and therefore are hydraulically inefficient to change borehole pressure. This is likely to be the case since the tidal situation differs from e.g. hydraulic testing in that no overpressure of any substational extent is enforced. The small pressure changes due to the tidal forcing – on the order of a few hPa – leave the fluid volumes mostly unchanged; fractures remain near a steady state; fluid transport can be neglected. In such a situation, the whole bedrock complex will cause almost the same tides in each borehole, the only difference arising due to the confinement stresses – the closer the section is located with respect to the surface, the lower is the effective elastic modulus and thus the tidal stress and thus the water pressure in the confined section. Eventual fractures may add only small perturbations to this condition, which we may characterise as regionally dominated. This finding is underpinned not at least by one borehole in particular (KI0023B), which has narrow depth sections that show different mixtures of the isotropic and the regional shear-coupled response.

Acknowledgements

I enjoyed the discussions with Stig Jönsson and Göran Nyberg of Geosigma, Uppsala. Plotting software has been provided under the GNU public license by Wessel and Smith (1998).

References

Bower D R, 1983: Bedrock fracture parameters from the interpretation of well tides, *J. Geophys. Res.,* vol. 88**,** 5025-5035.

Hart R H G, Gladwin M T, Gwither R L, Agnew D C, Wyatt F K, 1996: Tidal calibration of borehole strain meters: Removing the effect of small-scale inhomogeneity. *J. Geophys. Res.,* vol. 101**,** 25,553-25,771.

Munier R, 1993: Four-dimensional analysis of fracture arrays at the Äspö hard rock laboratory, SE Sweden, *Enginering Geology,* vol. 33, pp. 159-175.

Onoue K, Mukai A, Takemoto S, 2001: Tidal strains observed with extensometers in Donzurubo Observatory, Nara, Japan, *14th International Symposium on Earth Tides,* eds. Ooe, M., Crossley, D., Francis, O., Heki, K., Hanada, H., Jentzsch, G., Schuh, H., Shum, C.K. Tamura, Y., Journal of the Geodetic Society of Japan, vol.47, no.1, pp.141-147.

Scherneck H-G, 2001: Tides in fluid-filled fractures of the crystalline bedrock 1 – Theory, pre-study, and literature survey, Svensk Kärnbränslehantering AB.

Scherneck H-G, 2001b: Solid Earth model with liquid core and ocean loading in application to ground water tides in deep wells, *14th International Symposium on Earth Tides,* eds. Ooe, M., Crossley, D., Francis, O., Heki, K., Hanada, H., Jentzsch, G., Schuh, H., Shum, C.K. Tamura, Y., Journal of the Geodetic Society of Japan, vol.47, no.1, pp.204-212.

Takemoto S, Yamamoto T, Mukai A, Otsuka S, Fujimori K, 2003: Crustal Strain Observation for Nine Years with a Laser Strainmeter in Kobe, Japan, *Journal of Geodynamics,* Vol. 35/4-5, pp. 483 - 498.

Tamura Y, 1987: A harmonic development of the tide-generating potential. *Bull. d'Inform. Marées Terr.,* vol. 99, Observatoire Royal de Belgique, 6813-6855.

Wahr, J.M., 1981: Body tides on an elliptical, rotating, elastic and oceanless earth, *Geophys. J. R. astro. Soc.,* vol. 64, pp. 677-704

Wessel P, Smith W H F, 1998: New, improved version of the Generic Mapping Tools Released, *EOS Trans. AGU*, vol. 79, p. 579.